Photoacoustic Effect from Droplets to Imaging

By

Xingchi Yan

A dissertation submitted in partial fulfillment of the
requirements for the Degree of Doctor of Philosophy
in the subject of Chemical Physics at Brown University

Providence, Rhode Island
October 2022

This dissertation by Xingchi Yan is accepted in its present form by the Department of Chemistry as satisfying the dissertation requirement for the degree of Doctor of Philosophy.

Date ______________ ____
Gerald J. Diebold, Director

Recommended to the Graduate Council

Date ______________ ____
Lai-Sheng Wang, Reader
Brown University

Date ______________ ____
Christoph G. Rose-Petruck, Reader
Brown University

Approved by the Graduate Council

Date ______________ ____
Thomas A. Lewis
Dean of the Graduate School

Curriculum Vitae

Xingchi Yan attended Zhejiang University where he received Bachelor of Natural Sciences in 2017. He then started graduate school at Brown University in integrative studies with focus on chemical physics, applied mathematics and computer science. He received Master of Science in the field of Mathematical & Computational Science from Brown University.

Xingchi's research interests focus on the application of mathematics and computation to understand and design biochemical and biophysical measurements including all kinds of microscopy, spectroscopy and tomography. He's also interested in the probabilistic analysis of disorder, randomness and out-of-equilibrium phenomena in the biological systems.

Xingchi has been teaching assistant for several undergraduate and graduate courses at Brown including CHEM 0330 Equilibrium, Rate, and Structure, CHEM 1160 Physical Chemistry Laboratory and CHEM 2010 Advanced Thermodynamics.

Acknowledgements

First and foremost, I would like to express my deepest acknowledgements to my advisor, Prof. Gerald J. Diebold, for his constant support, guidance and inspiration throughout my graduate study. Being an excellent researcher and a dedicated teacher, he is always available to provide help in any aspects, from experiments where we try to capture the smallest signal to the theoretical problems that seem impossible to find an analytical solution. Prof. Diebold's passion for science and continuous encouragements have helped me overcome numerous challenges and obstacles in my graduate study, I could never ask for a better mentor. I will leave Brown with many warm memories in the Diebold lab doing exciting experiments together with memorable lab members Yaqi, Wenyu and Hong.

I'd like to thank my committee members Prof. Lai-Sheng Wang and Prof. Christoph Rose-Petruck profusely for all the participation, advice and encouragements in my PhD milestones. I am indebted to them for their scientific insights and time commitment. I am especially grateful to Prof. Brenda Rubenstein, who has been our physical chemistry advisor since my first year at Brown and has always been there to offer help over the years. Brown's collaborative, interdisciplinary and innovative culture, revealed in the Open Curriculum, provides extraordinary flexibility and resources for interaction and collaboration among and beyond the community. Many amazing professors in distinct disciplines across the campus contributed their expertise, knowledge and passion for science over the years through their dedication to teaching and mentoring, which greatly inspire me, including Prof. Robert Pelcovits, Prof. Thomas Powers, Prof. Kemp Plumb, Prof. Andrey Gromov in the Department of Physics, Prof. Peter Weber, Prof. Richard Stratt in the Department of Chemistry, Prof. Paul Dupuis, Prof. Kavita Ramanan, Prof. John Mallet-Paret, Prof. Oanh Nguyen, Prof. Jerome Darbon, Prof. Mark Ainsworth, Prof. Hui Wang in the Division of Applied Mathematics, Prof. Eli Upfal, Prof. Sorin Istrail, Prof. Michael Littman, Prof. Ritambhara Singh in the Department of Computer Science and Prof. Constantine Gatsonis in the Department of Biostatistics. I'd like to extend my appreciation to all the department faculty and stuff members, the machine shop stuff members Ken, Randy and Al, Graduate School, Center for Computation and Visualization as well as directors of graduate studies, Prof. Li-qiong Wang, Prof. Vicki Colvin, Prof. Sarah Delaney and Prof. Shouheng Sun.

Part of what make my Brown experience unique are the fantastic people that I've met in the campus. I am grateful for all my friends and classmates with whom we discuss science and share joys. And special thanks also goes to all the undergraduates that I have TAed, their curiosity in science, passion for learning and kindness in helping each other have motived me to become a better teacher and researcher.

The thesis is dedicated to my parents and grandparents whom have always been there for me in every stage of my life.

Contents

⋆ Parts of this dissertation appeared in peer-reviewed journals. In particular, Part of Chapter 2 is from Ref. [1], part of Chapter 3 is from Ref. [2]. Parts of this dissertation contain unpublished manuscripts.

List of Tables

List of Figures

Chapter 1

Introduction

> “ If one is working from the point of view of getting beauty into one’s equations, and if one has really a sound insight, one is on a sure line of progress. ”
>
> Paul A.M. Dirac

A prominent feature of the photoacoustic effect [3, 4] inside fluids is that the temporal domain and spatial domain features of the acoustic waves generated by absorption of short pulse optical radiation contains information of the irradiated body owing to different absorption coefficients. This innovative idea was first pointed out by a list of experimental works where optically thin fluid and solids surrounded by different liquids were irradiated by nanosecond laser pulses to generate distinct photoacoustic waves [5–8]. The saliant feature of the photoacoustic effect would lead to enormous applications in both spectroscopy and imaging. Chapter 1 will introduce the basic of the photoacoustic effect, summarize the forward simulation and inverse problems solving involved with the photoacoustic effect. Applications of this effect in trace gas detection and photoacoustic imaging will be discussed.

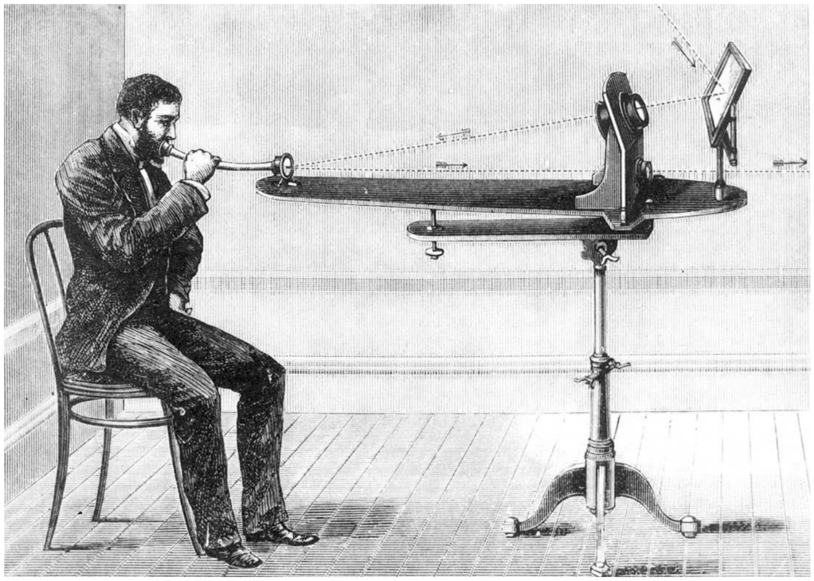

Figure 1.1: The transmitter of Bell's microphone, sunlight is reflected from a voice-modulated mirror, Courtesy of Bell Laboratories.

1.1 Overview of the photoacoustic effect

The photoacoustic effect, also frequently called optoacoustic effect, was discovered by Alexander G. Bell in 1880. The effect refers to the generation of acoustic waves by absorption of optical radiation. As in Fig. 1.1 shows, Alexander G. Bell discovered the photoacoustic effect by using the modulated solar radiation which was transmitted and intercepted by a photoacoustic cell thus producing sound corresponding to the voice modulation [9, 10]. However this effect was not highly valued until the invention of laser which leads to graduate accumulation of works on photoacoustic spectroscopy [11–13]. There are numerous applications of photoacoustic effects, the most important being trace gas detection and optoacoustic tomography, which could combine the advantages of strong contrast by optical absorption with deep acoustic penetration depth and offer unique diagnostic opportunities relative to traditional imaging modalities.

Modeling the generation and propagation of photoacoustic waves inside fluids would involve the laws of fluid dynamics where the energy conservation equation is modified with an energy source term from optical heating [3,4]. The heat conduction as well as viscous dissipation can often be ignored, thus the set of fluid mechanics equations can be transformed into the photoacoustic wave equation [6],

$$\left(\nabla^2 - \frac{1}{c^2}\frac{\partial^2}{\partial t^2}\right) p = -\frac{\beta}{C_P}\frac{\partial H}{\partial t}. \tag{1.1}$$

From Eq. 1.1, we can see that any changes in the light intensity of radiation source with respect to time, i.e. $\frac{\partial H}{\partial t}$, would give rise to a non-zero term that acts as a source and lead to the acoustic wave generation. The physics for production of photoacoustic waves in solids [14] is different from that inside fluids and we will focus on the photoacoustic effect inside fluids in this thesis. As it is well-known, more than 60 percent of the human body is water hence the study of the photoacoustic effect inside fluids would be essential for the purpose of bioimaging.

1.2 Photoacoustic wave forward simulation

To study the photoacoustic effects inside fluids, one would hope to determine the frequency and time domain solution of the wave equation for arbitrary objects inside any fluid medium with various optical heating functions. This can be seen as wave forward problem where the sources, the initial and boundary conditions as well as the medium together determine the features of generation and propagation of the photoacoustic waves.

The photoacoustic wave forward problem can be approached by solving Eq. 1.1 under certain geometry, initial and boundary conditions. However the acoustic absorption is not considered in Eq. 1.1. Although the acoustic absorption might be neglected in most cases for simplicity, it may not be neglected in highly acoustically attenuating materials. The acoustic attenuation $\alpha(r, f)$ can often be modeled as a power law relationship with frequency f as Eq. 1.2 shows [15],

$$\alpha(r, f) = \alpha_0(r) f^y, \tag{1.2}$$

where r represents the space dependence of acoustic attenuation and the power y is typically between 0.9 to 2.0 in tissues [5, 15].

A series of works have come up in modeling the acoustic absorption in lossy media by incorporating the lossy derivative operator [15–19]. Here the case that the acoustic wave propagation modeled by the following coupled differential equations using the fractional Laplacian [20] is presented. Denote $p(r, t)$ as the photoacoustic pressure at position r and time t and $u(r, t)$ as the acoustic particle velocity, the following coupled differential equations can be used to model the photoacoustic effect [20],

$$\frac{\partial u(r,t)}{\partial t} + \frac{1}{\rho_0(r)} \nabla p(r,t) = 0, \tag{1.3}$$

$$\frac{1}{\rho_0(r)} \frac{\partial \rho(r,t)}{\partial t} + \nabla u(r,t) = 0, \tag{1.4}$$

$$p(r,t) = c_0(r)^2 \left(1 - \mu(r) \frac{\partial}{\partial t} (-\nabla^2)^{y/2-1} - \eta(r)(-\nabla^2)^{y/2-1/2} \right) \rho(r,t), \tag{1.5}$$

with initial conditions

$$p(r, 0) = \Gamma(r) A(r), \;\; u(r, 0) = 0, \tag{1.6}$$

where $\mu(r)$ is the acoustic absorption coefficient and $\eta(r)$ is the acoustic dispersion coefficient which are defined as $\mu(r) = -2\alpha_0 c_0(r)^{y-1}$ and $\eta(r) = 2\alpha_0 c_0(r)^y \tan(\frac{\pi y}{2})$. If we neglect the acoustic absorption and dispersion, then Eq. 1.5 becomes $p(r, t) =$

$c_0(r)^2\rho(r,t)$ which is the adiabatic state equation [20].

1.2.1 Analytical solutions

As mentioned, for optical thin bodies with simple geometries, one would be able to get analytical solutions to the wave equation Eq. 1.1 where the spatial and temporal dynamics of the generated acoustic waves depend on the properties of the sources. In Chapter 1, we will focus on several analytical solutions to the photoacoustic wave equation in the cases of spherical droplets, fluid layers and moving optical sources in a one-dimensional resonator.

The analytical solutions are essential as they can provide appreciable physical insights to the problems of interest. For example, the frequency dependence of the pressure waves or perhaps power-law dependence of some parameters can be easily obtained from analytical solutions. The analytical solutions would also serve as a necessary check for other numerical methods. For example, Ref. [21] studied the k-space wave propagation in heterogeneous media and compared their model with the analytical solution proposed by Diebold and Sun for the cylindrical source with a Gaussian heating function [8] and found excellent match.

However the analytical solutions would only be feasible in certain cases under ideal conditions while in many practical scenarios concerning with the imaging of arbitrary objects, it would be impossible to obtain analytical solutions that can describe the whole physical picture. Hence numerical methods would be necessary to obtain or approximate the computational solutions to the coupled differential equations.

1.2.2 Finite Difference Methods

There have been a series of works on solving the coupled wave propagation equations using the finite difference methods, for example, the simulation of wave propagation in the abdominal wall in 2D in Ref. [22].

Here a simple three-dimensional finite-difference time-domain (FDTD) scheme to solve the coupled differential equations similar with Ref. [22] is presented.

Define $S = (\frac{p}{\rho c^2}, \rho u_x, \rho u_y, \rho u_z)$, $F = (u_x, p, 0, 0)$, $G = (u_y, 0, p, 0)$ and $H = (u_z, 0, 0, p)$. The coupled equations can be written as,

$$\frac{\partial S(x,y,z,t)}{\partial t} + \frac{\partial F(S(x,y,z,t))}{\partial x} + \frac{\partial G(S(x,y,z,t))}{\partial y} + \frac{\partial H(S(x,y,z,t))}{\partial z} = 0. \quad (1.7)$$

A second-order space and second-order time accurate algorithm can be written as,

$$S^* = S^n + \Delta t \Theta(S^n), \quad (1.8)$$

$$S^{n+1} = \frac{1}{2}S^n + \frac{1}{2}\Big(S^* + \Delta t \Theta(S^*)\Big), \quad (1.9)$$

where Δt is the time step and the space discretization can be written as

$$\Theta(S^n) = -\frac{\partial F(S^n)}{\partial x} - \frac{\partial G(S^n)}{\partial y} - \frac{\partial H(S^n)}{\partial z}, \quad (1.10)$$

with $\frac{\partial F(S^n)}{\partial x}$, $\frac{\partial G(S^n)}{\partial y}$ and $\frac{\partial H(S^n)}{\partial z}$ approximated by,

$$\frac{\partial F(S^n)}{\partial x} \approx \frac{F(S^n(x_{i+1}, y_j, z_k)) - 2F(S^n(x_i, y_j, z_k)) + F(S^n(x_{i-1}, y_j, z_k))}{\Delta x^2}, \quad (1.11)$$

$$\frac{\partial G(S^n)}{\partial y} \approx \frac{G(S^n(x_i, y_{j+1}, z_k)) - 2G(S^n(x_i, y_j, z_k)) + G(S^n(x_i, y_{j-1}, z_k)}{\Delta y^2}, \quad (1.12)$$

$$\frac{\partial H(S^n)}{\partial z} \approx \frac{H(S^n(x_i, y_j, z_{k+1})) - 2H(S^n(x_i, y_j, z_k)) + H(S^n(x_i, y_j, z_{k-1}))}{\Delta z^2}. \quad (1.13)$$

A two step MacCormack algorithm [23] which has fourth-order space accuracy and second-order time accuracy was used in Ref. [22]. Other more sophisticated time discretization schemes such as strong stability preserving high-order time discretization methods described in Ref. [24] may be considered as well. The finite difference methods are straightforward to implement, however, it has a huge computational cost for three dimensional, highly complicated media especially in application scenarios over a large frequency range. A large number of grids points would be required to recover the subtle time and frequency features of the high frequency acoustic wave components [21].

1.2.3 Finite Element Methods

Finite element methods (FEM) involve a list of basis functions to represent the solutions for the partial different equations [25–27]. One can often incorporate the median heterogeneities in the FEM to approximate the solutions where a list of chosen basis functions are used. These basis functions are often only supported on very small intervals hence calculating the coefficients of the basis functions at different intervals would reduce to the problems of solving sparse matrix systems for which many efficient algorithms have been proposed [28]. There are several works in photoacoustics using FEM, for example, Ref. [29] uses the finite element method to reconstruct the optical and acoustic properties from the frequency domain Helmholtz type photoacoustic wave equation.

1.2.4 Spectral Methods

The fast Fourier transform would greatly benefit the spectral methods, making it much faster than the traditional finite difference method in a wide range of applications [30]. The k-space method for solving acoustic wave propagation was proposed in Ref. [31] where the authors used the absorbing boundary condition in the simulation. The coupled differential equations become [31],

$$\frac{\partial u(r,t)}{\partial t} + \frac{1}{\rho(r)} \nabla p(r,t) + \alpha u(r,t) = 0, \tag{1.14}$$

$$\frac{\partial p(r,t)}{\partial t} + \rho(r) c(r)^2 \nabla \cdot u(r,t) - \Gamma H + (\alpha_x + \alpha_y + \alpha_z) p(r,t) = 0, \tag{1.15}$$

where ΓH is the photoacoustic source term, $\alpha = (\alpha_x, \alpha_y, \alpha_z)$ is the term associated with the absorbing boundary condition. The absorption coefficient α is defined to be nonzero in a layer near the edges of the computational domain orthogonal to the boundary and zero elsewhere [31]. This type of absorbing boundary condition is also called the perfect matched layer [32] which is frequently used in the simulations of fluid mechanics and electromagnetic phenomena to avoid introducing truncation artifacts in computation [33].

It is worth noting that instead of using the conventional k-space substitution rule for the Laplacian operator $\nabla^2 \to -k^2$, Ref. [21] uses the substitution rule $\nabla^2 \to -k^2 sinc^2(c_0 k \Delta t/2)$. The reasoning is stated in the Ref. [21] and the core idea lies in the routine of most theoretical photoacoustic problems. One would often start from the photoacoustic wave equation, assume the source to be stationary, Fourier transform the result into k-space, solving the equation using Green's function and then inverse Fourier tranform back to obtain the real space pressure field [21]. Without too much math presented, the discretization for any time step was found to be [21],

$$\hat{p}(t+\Delta t) - 2\hat{p}(t) + \hat{p}(t-\Delta t) = -4\sin^2(c_0 k\Delta t/2)\hat{p}(t), \tag{1.16}$$

where the simple finite difference scheme often approximates the right-hand term by first-order Taylor approximation as $-c_0^2k^2\hat{p}(t)$. The discretization rule in Eq. 1.16 is the reason why Ref. [21] used different Laplacian substitution rules. Hence the operator $\frac{\partial}{\partial x} \rightarrow ik_x sinc(c_0 k\Delta t/2)$ and $\frac{\partial}{\partial x} = F\Big(ik_x sinc(c_0 k\Delta t/2)\Big)$ [21].

The coupled differential equations can thus be rewritten as in Ref. [34],

$$\frac{\partial u_x}{\partial t} = -\nabla p/\rho - \alpha_x u_x, \tag{1.17}$$

$$\frac{\partial u_y}{\partial t} = -\nabla p/\rho - \alpha_y u_y, \tag{1.18}$$

$$\frac{\partial u_z}{\partial t} = -\nabla p/\rho - \alpha_z u_z, \tag{1.19}$$

$$\frac{\partial p_x}{\partial t} = -\rho c^2\frac{\partial u_x}{\partial x} + \Gamma H/3 - \alpha_x p_x, \tag{1.20}$$

$$\frac{\partial p_y}{\partial t} = -\rho c^2\frac{\partial u_y}{\partial y} + \Gamma H/3 - \alpha_y p_y, \tag{1.21}$$

$$\frac{\partial p_z}{\partial t} = -\rho c^2\frac{\partial u_z}{\partial z} + \Gamma H/3 - \alpha_z p_z. \tag{1.22}$$

One of the most commonly used toolbox for the photoacoustic forward simulation that starts from Eq. 1.17 to Eq. 1.22 developed by Bradley E. Treeby and Ben T. Cox is called k-wave [34]. Figure 1.2 shows the computational steps for solving the coupled equations using staggered grids. The first step is to calculate $\frac{\partial p}{\partial x}$, $\frac{\partial p}{\partial y}$ and $\frac{\partial p}{\partial z}$ from the initial pressure field p. Then the velocity components u_x, u_y and u_z are updated. Next, the partial derivative of the velocity with respect to the coordinate, $\frac{\partial u_x}{\partial x}$, $\frac{\partial u_y}{\partial y}$, $\frac{\partial u_z}{\partial z}$are calculated. Next, the acoustic densities ρ_x, ρ_y and ρ_z are updated [34]. The

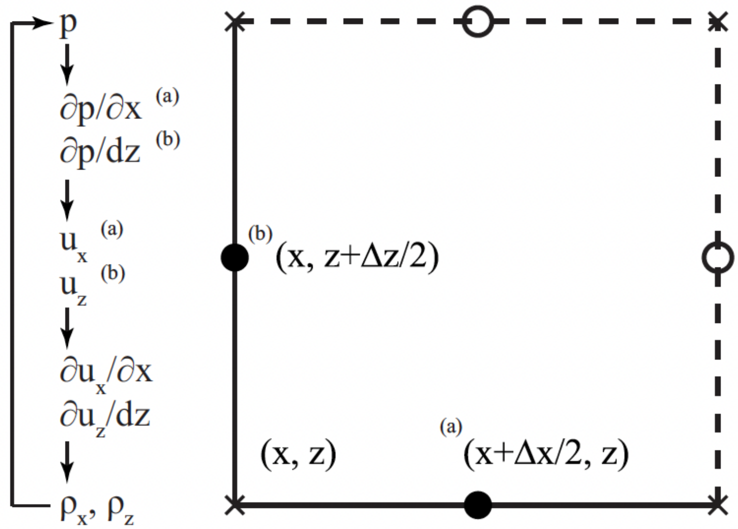

Figure 1.2: The computational steps in solving the coupled first order acoustic equations for heterogeneous media using a staggered spatial grid in k-wave. The figure is taken from Ref. [34].

k-space method for the forward simulations will be used in Chapter 4.

1.3 Inverse Problems in photoacoustic imaging

Section 1.2 describes the photoacoustic forward simulation while a series of practical challenges would involve inverse problems. As shown in Fig. 1.3, there are two main inverse problems in photoacoustic imaging, one is acoustic inversion which aims to reconstruct the initial acoustic pressure distribution from measured acoustic time series, the other is optical inversion which aims to reconstruct the optical absorption coefficients from the initial acoustic pressure distribution. The acoustic inversion is related to the photoacoustic wave propagation and the process involves inverting wave propagation in complex medium hence it is typically harder than the optical inversion. The thesis, especially in Chapter 4 for inverse problems in optoacoustic tomography, will focus on the acoustic inversion.

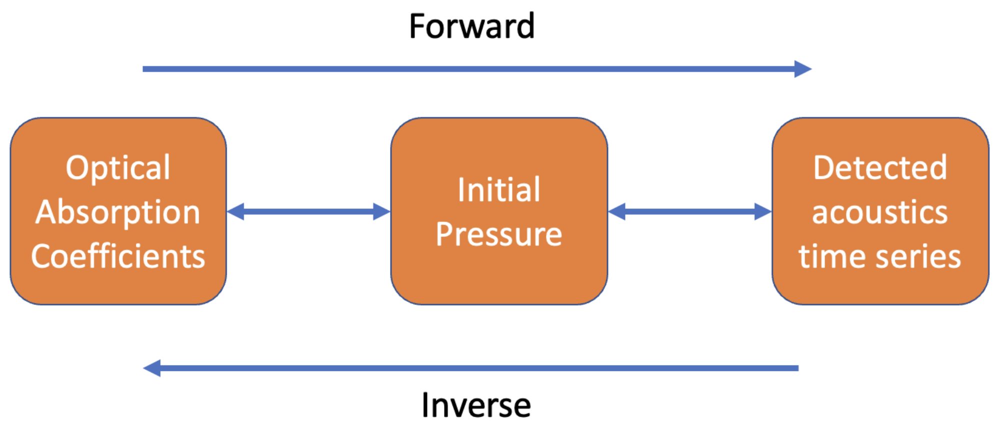

Figure 1.3: Scheme of forward and inverse problems in photoacoustic imaging. The forward process consist of the mapping of the optical absorption coefficients to the initial pressure and the mapping of the initial pressure to the detected acoustic time series signals. The acoustic inversion aims to reconstruct the initial pressure from the measured acoustic time series signals and the optical inversion aims to reconstruct the optical absorption coefficients of the objects from the initial generated photoacoustic pressure.

1.3.1 Spherical Radon transform

Spherical radon transform has been widely used in solving inverse problems in optoacoustic tomography. The physical picture of the forward and inverse processes in optoacoustic tomography can be encoded in the forward operator A that maps the initial pressure to the measured acoustic time series g at the detector positions as well as its generalized inverse. The forward operator A can be characterized by integrating p_0 along a set of spherical balls of radius $t = \frac{|r-r_d|}{c}$ where r_d is the detector position and c is the speed of sound [35,36]. The inverse process might be solved by backprojection algorithms which map the measured acoustic time series signal g that is a function of detector arrangements and time into the initial pressure p_0 by reversing the forward process [35,36].

The problem of recovering a function from its spherical mean has been studied extensively in mathematical literature which leads to numerous applications in thermoacoustic [37] and photoacoustic tomography [35]. These works would date back to the Norton's paper [38] on recovering the reflecting object from its line integrals over the circular geometry case [39–41]. If we assume the simplest case that the acoustic medium is homogeneous and there is no acoustic absorption, the spherical mean radon transform [39–41] can be used to obtain accurate initial pressure distribution reconstruction. The famous universal backprojection algorithms can give exact reconstruction for planar, cylindrical and spherical measurement geometries under certain assumptions [35].

In two dimensions, the filtered backprojection formula is given by Ref. [40,42],

$$p_0(r) = -\frac{1}{\pi R}\int_{\partial S}\int_{|r-z|}^{\infty}\frac{(\partial_t tAp_0)(t,r)}{\sqrt{t^2-|r-z|^2}}dtdS(z), \tag{1.23}$$

where $S = \left\{r \middle| \|r\| < R\right\}$ and R is the radius of detector circle. Here A is the forward operator that is defined as, for $(r,t) \in \partial S \times [0,T]$,

$$(Ap_0)(r,t) = p(r,t). \tag{1.24}$$

The inversion formula in Eq. 1.23 looks quite complicated; it can be seen as the integration along the curve which is the interaction of a cylinder with radius R and a cone that is centered at r. For three dimensions, the filtered backprojection formula has been given in Ref. [35,41]. For 2D integrating line detectors [43,44] which measure line integral of the acoustic wave field, the inversion formula has been given in Ref. [45].

The above inversion formulas are explicit and they are mathematically rigorous under the ideal assumptions. However, these inversion formulas can only be applied for certain geometries and challenges would arise in more complicated geometries such as limited-view case for which some artifacts may occur in the reconstruction. Besides, the assumptions of homogeneous acoustic properties and no absorption are sometimes impractical, especially in the case of large acoustic heterogeneity such as imaging the human brain where the differences of the acoustic properties of bones and tissues should be accounted for. The acoustic absorption in the tissues would also have an impact on the measured frequency spectrum, however, these models may not be able to incorporate acoustic absorption. Despite these limitations, the challenge of reconstructing a function from its spherical means has been a great topic for the exploration of mathematicians.

1.3.2 Time Reversal

One may encounter the idea of time reversal from quantum mechanics which represents some symmetry in the physics language. Translational symmetry would correspond to momentum conservation, rotation symmetry would correspond to angular momentum conservation, and time translational symmetry would correspond to energy conservation [46]. The principle of time reversal is similar to backpropagate the wave equation using the measured time series data at the detectors as the boundary condition where the initial pressure can be recovered at time $t = 0$ [47]. It is similar to backprojection-type algorithms discussed in Section 1.3.1 however the methods of time reversal would be easy to generalize to heterogeneous media and any detection setups as long as the forward wave propagation can be well-characterized [47]. The implementation depends on the inversion of the numerical computation of the forward wave propagation models by repropagating the wave received at the detectors with a reversed time array [47]. There have been several works on developing time reversal approaches [48, 49] that can deal with the variations of sound speeds in photoacoustic imaging. The absorbing acoustic media can also be accounted for using the time reversal method proposed in Ref. [47]. The method of time reversal has connections with and advantages over the methods based on spherical Radon transform. It is computationally efficient for any detection geometry in 3D heterogeneous acoustic media [50].

1.3.3 Variational reconstruction

Although time reversal methods have been very successful and already widely used in inverse problems in optoacoustic tomography, in many practical cases, the reconstruction qualities suffer due to the incomplete spatial resolution as well as the finite bandwidth of the transducers. When the measured data are incomplete, the framework of variational image reconstruction would provide unique advantages over the time reversal type reconstructions. The variational approach solves the following optimization problem,

$$\hat{p}_0 = \arg\min_{p_0} \left\{ \frac{1}{2} \|Ap_0 - g\|_2^2 + \lambda R(p_0) \right\}, \tag{1.25}$$

where g is the measurement time series data and A is the forward operator that maps the initial pressure distribution p_0 to the measurements and $R(p_0)$ is some regularization on the initial pressure p_0.

The solution to the optimization in Eq. 1.25 typically involves the gradient descents which would require the knowledge of the forward operator A and the adjoint of A that is often denoted as A^*. In most cases in optoacoustic tomography, as the forward matrix A is real for all entries, A^* is same as A^T.

In one dimension or two dimensions, it is possible to calculate the matrix A explicitly and perform matrix operations without too much computational cost. However, in three dimensions, it would be impractical to save the matrix A as the dimension of A is $(N_xN_yN_t, N_xN_yN_z)$, take $N_x = N_y = N_z = 64$ and $N_t = 128$ for simplicity, it would cost around 2^{39} bytes which is around 550 GB to store one matrix. Moreover, although there have been some works on constructing sparse matrix representations to approximate A [51,52], it would be computational infeasible to construct explicitly the matrix A in three dimensions by superposition principle due to the high computational cost related with each forward simulation. It would be impossible and computationally inefficient to store and operate on matrix A directly for three dimensional high-resolution applications as well. Luckily, in most cases, one would not need an explicit knowledge of A but rather the action of A for which k-wave can be used to simulate. What about the adjoint operator A^*?

There has been study of the adjoint operator A^* [53] by deriving the operator using the property of Green's function for the wave propagator. The subtle comparison of the adjoint operator and the time reversal operator can be found in Ref. [53]. The paper [53] found that the action for the adjoint operator can be calculated by the forward model using carefully defined sources which can be quite useful in iterative model-based reconstruction as most iterative algorithms would involve the calculation of action for the adjoint operator.

Figure 1.4 shows the state of art reconstruction methods for different medical and biophysical imaging modalities. We can see that up to year 2000, most methods are linear including filtered backprojection, l_2 regularization as well as linear filters. However, since year 2010, most methods change to the nonlinear methods where the total variation type of regularization or wavelet sparsity are incorporated [54]. As photoacoustic tomography is a very new imaging modality compared with other

Method	Up to 2000	Since 2010
Full CT	Filtered backprojection	Filtered backprojection
Undersampled CT	Filtered backprojection	TV-type / wavelet sparsity
PET / SPECT	Filtered backprojection / EM	EM-TV / dynamic sparsity
Photacoustics	–	TV-type / wavelet sparsity
EEG / MEG	LORETA	Spatial sparsity / Bayesian
ECG-BSPM	L2 Tikhonov	L1 of normal derivative
Microscopy	None, linear filter	TV-type / shearlet sparsity
PET-CT / MR	–	TV-type anatomical priors

Figure 1.4: State of the art methods for inverse problems in medical and biophysical imaging. Table taken from Ref. [54].

more well-established imaging modalities, it often borrows the reconstruction ideas from the other modalities. An overview of the advancement in the broad areas of imaging sciences and applied mathematics would be very beneficial for the algorithm development in the field of photoacoustic imaging.

1.4 Application I: Trace gas detection

One of the most widely used application for the photoacoustic effect would be trace gas detection. The basic principle is that the temperature increase due to the absorption of optical radiation increases the pressure to be detected. In experiments one often uses an amplitude-modulated infrared laser to match the absorption line of some particular molecules. The typical experiments, which are shown in Fig. 1.5, are often conducted in an acoustic cell (resonators) to enhance the acoustic wave produced. The modulation frequency can be tuned from a few Hz to a few kHz depending on the specific setups.

The sensitivity of trace gas detection would depend on many factors, for example the resonator, and the sensitivity of the acoustic transducer (often a microphone). In

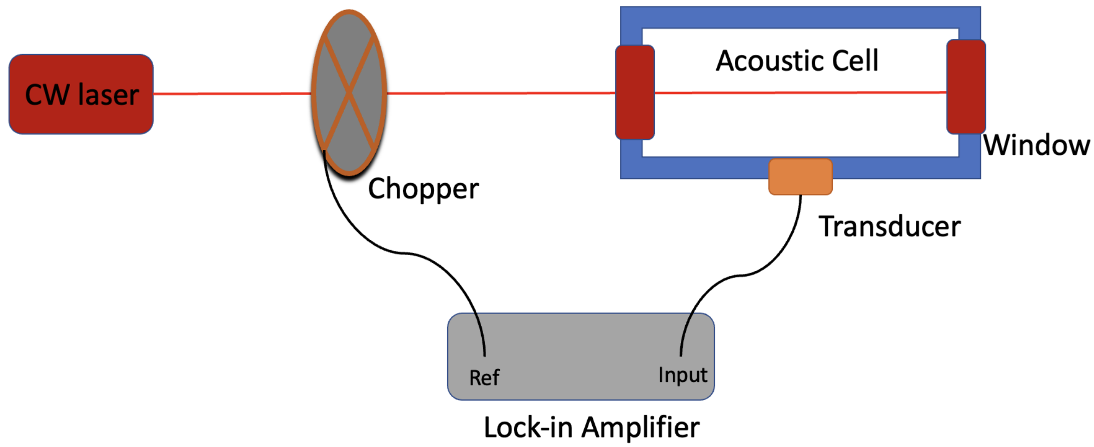

Figure 1.5: A typical experimental setup for photoacoustic trace gas detection. Laser intensity is modulated by the chopper. The acoustic cell consists of two windows which have low absorption. The detected acoustic wave signal by the transducer is fed to a lock-in amplifier to amplify the signal.

one high frequency experiments a piezoelectric crystal was used where the Q factor of the transducer was the determining factor for high sensitivity. The Q factor of a typical $LiNbO_3$ is around 1384 while crystal BiB_3O_6 can have a Q factor of 10800 which, with a design of a moving optical grating, could reach a detection limit in the parts-per-quadrillion range [55].

Section 2.4 discusses about the possibility of a moving continuous optical beam in one dimensional resonator to reach sensitive detection even with traditional transducers.

1.5 Application II: Photoacoustic computed tomography, microscopy and endoscopy

Another central application of the photoacoustic effect would be bioimaging such as detecting tumor cells [56] and *in vivo* imaging of hemoglobin oxygen saturation [57]. In photoacoustic imaging, short pulse laser is often used so that the time for heat conduction is much longer than that for acoustic wave propagation. The laser interacts with the biological molecules such as the hemoglobin, water and lipids and these molecules have different absorption coefficients which give rise to the contrast mechanism. The pressure wave would be generated due to the absorbed heat and propagate in the medium obeying the laws of the wave physics. The detected acoustic waves, often by solid transducers, can be used to reconstruct the initial pressure distribution thus the optical absorption coefficients. There are all kinds of photoacoustic imaging modalities including photoacoustic computed tomography which is often called optoacoustic tomography, photoacoustic microscopy and photoacoustic endoscopy [58, 59].

1.5.1 Photoacoustic computed tomography

The basic principle of photoacoustic computed tomography (PACT) is to use multiple acoustic detectors located at different positions to detect the acoustic wave generated by wide field optical illumination [50, 58–60].

One possible setup uses ring-shaped ultrasonic transducer array (UTA) to detect the acoustic waves generated by the interaction of the object with a laser beam passing by diffuser [61] . Another possible shape of the ultrasnoic transducer array is the hemispheric shaped UTA [62] where the laser beam passes through a diffuser, interacts with the object to produce photoacoustic effects and the detectors are positioned as a hemispheric array. A Fabry-Perot interferometer has also been used where the laser beam is scanned across the surface of the interferometer [63]. Some groups use a linear ultrasonic transducer array [64] where the excitation light is directed into the sample at certain angles and the acoustic wave is emitted and detected by a linear array of transductors.

1.5.2 Photoacoustic microscopy

The photoacoustic microscopy, different from PACT, mostly relies on the scanning of a focused laser beam and ultasonic transducer for generation and detection of the acoustic waves [50, 58–60]. In one configuration, the ultasonic focusing lens and the high numerical aperture optical focus lens are on the opposite side of the imaging objects to achieve sub-wavelength resolution [65]. Other possible systems might use the optical-acoustic combiner that reflects sound but not the transmitted light to observe label-free oxygen metabolic rate [66]. Photoacoustic microscopy would not require the same reconstruction as in photoacoustic computed tomography.

1.5.3 Photoacoustic endoscopy

The photoacoustic endoscopy has been used [67] in combination with ultrasound endoscopy to image the internal organs *in vivo*. Traditional ultrasound endoscopy would suffer from low contrast as its contrast comes from mechanical wave perturbation. The high molecular contrast provided by optical absorption makes functional imaging possible.

Besides the above applications, photoacoustic imaging has been combined with other imaging modalities, for example, a combination of photoacoustic, MRI, Raman imaging for noninvasive brain tumor delineation which leads to a more accurate molecular imaging strategy [68]. It would be impossible to list all the recent advances in photoacoustic imaging in Section 1.5 . The review articles [58, 59] has a very detailed comparison of all these photoacoustic tomography techniques. Owing to the unique advantages related with the physical mechanisms of photoacoustic effect, the area of photoacoustic imaging in biomedicine is growing rapidly in recent years.

Chapter 2

Generation of photoacoustic effect

> “Plato is my friend — Aristotle is my friend — truth is a greater friend.
> If I have seen further it is only by standing on the shoulders of giants. ”
>
> – Sir Isaac Newton

A thorough understanding for generation of photoacoustic effect is essential for applications such as photoacoustic spectroscopy and imaging. The photoacoustic effect can be generated in both solids and fluids. The generation of photoacoustic waves with solids has been well studied in Ref. [14]. This thesis will focus on the generation of photoacoustic effects inside fluids.

A salient feature of the photoacoustic effect [3, 4] in fluids is that the temporal and spatial characteristics of the ultrasonic waves generated by absorption of short pulse optical radiation contains information on the spatial absorption profile of the irradiated body. This principle was first demonstrated experimentally in a series of papers where optically thin fluid and solid bodies with simple geometries immersed in various solvents were irradiated by nanosecond laser pulses. Subsequently this feature of the photoacoustic effect has been used as the basis for medical imaging [50, 69–77] where arrays of transducers are used to record the spatial and temporal patterns of emitted acoustic waves with sophisticated mathematical methods employed to invert acoustic data into images whose contrast is governed by optical absorption.

2.1 Overview

The generation of photoacoustic effect is coupled multi-physics process. In the case of optically thin bodies with simple geometries irradiated by short light pulses, solutions to the wave equation for pressure [5–8] for solid and liquid layers [78, 79], spheres [80–83], cylinders [78,84], and ellipsoids [85,86] yield photoacoustic waveforms with temporal features dependent on the geometry, dimensions, sound speed, and density of the irradiated body. With a knowledge of the density and sound speed of the surrounding fluid, together with a fitting of an experimental waveform to theory, the last three of these acoustic properties of the absorbing body can be determined, thus making the photoacoustic effect an analytical technique. The experimental studies of ultrasonic waves emitted by laser irradiated bodies with symmetry in one, two, and three dimensions have shown excellent agreement with theory. However, there appears to be no investigation, either theoretical or experimental, into the character of the waves produced within the irradiated body although theoretical expressions for determining the waveforms generated internally have been found.

2.2 Photoacoustics effect generated by spherical droplets

Photoacoustic excitation of a fluid sphere generates an outgoing ultrasonic wave whose time profile permits determination of the density, sound speed, and diameter of the sphere. Experiments with pulsed laser beams have confirmed the major predictions of existing theory. With regard to acoustic waves generated within spheres, although mathematical expressions for their properties are known, virtually no exploration of the waveforms in theory or experiment has taken place. Here, two cases for photoacoustic excitation of a droplet are discussed: first, absorption of radiation in a region of fluid external to the droplet, and, second, absorption of radiation by the droplet itself. Large amplitude transients, compressions in the former and rarefactions in the latter, are generated as the waves approach the center of the sphere. The high amplitudes of the waves suggest shock wave formation.

Here, the question of the time dependence of photoacoustic waves found within droplets is addressed. In the Sections 2.2.2 and 2.2.3, two problems are presented, the first being determination of the time and space dependence of photoacoustic waves launched from absorption by a spherical region external to the droplet, and second, when the photoacoustic effect is generated by absorption within the droplet itself. Section 2.2.1 gives a solution for a fluid sphere surrounded by an optically thin, absorbing layer of a second fluid. The creation of a rapid pressure increase by absorption of a short laser pulse causes compressive waves to enter the droplet resulting in large pressure transients as waves propagate to the center of the droplet. In Section 2.2.2 the character of photoacoustic waves generated by absorption of radiation within the sphere itself are investigated. In this case, a series of compressive waves are found along with large rarefactions. In both problems frequency domain expressions are derived, which for the case of equal densities can be Fourier transformed to yield analytical time domain expressions for the sound waves. Section 2.2.3 notes the possibilities of shock wave generation in spheres even for low laser fluences arising from ultrasonic waves propagating to the origin with ever increasing amplitudes.

2.2.1 Photoacoustic effect generated by spherical droplets inside a surrounding absorber

In order that the time integral of the pressure should be zero for acoustic waves in two and three dimensions, as noted in Ref. [87], the surrounding layer is given a boundary with a third, non-absorbing fluid that extends from the absorbing spherical region to infinity. It is clear that if the surrounding layer possessed a rigid outer boundary, there would be an overall pressure increase in the sphere and its surroundings long after absorption of the optical radiation so the pressure integral would not vanish. Therefore, a third fluid is taken to surround the absorbing layer. From the point of view of any experiment where the ultrasound within the sphere is of interest, the acoustical character of the third region is not considered in this thesis. Given the complexity of solving the conservation equation for the photoacoustic effect at two interfaces, the density and sound speed of the infinite layer are taken to be identical to that of the absorbing layer. The part of the problem of interest is thus preserved without the need for carrying out excessive algebraic manipulations.

As shown in Fig. 2.1, a sphere with density ρ_s, sound speed c_s, and radius a is surrounded by an optically thin absorbing layer with an optical absorption coefficient $\bar{\alpha}$, density ρ_f, sound speed c_f, and radius b. The outermost region, which extends from b to infinity is taken to have the same density and sound speed as the absorbing layer. The wave equation for pressure [6] in an inviscid fluid is given by

$$\left(\nabla^2 - \frac{1}{c^2}\frac{\partial^2}{\partial t^2}\right) p = -\frac{\beta}{C_P}\frac{\partial H}{\partial t}, \tag{2.1}$$

where t is the time, c is the sound speed, p is the pressure, β is thermal expansion

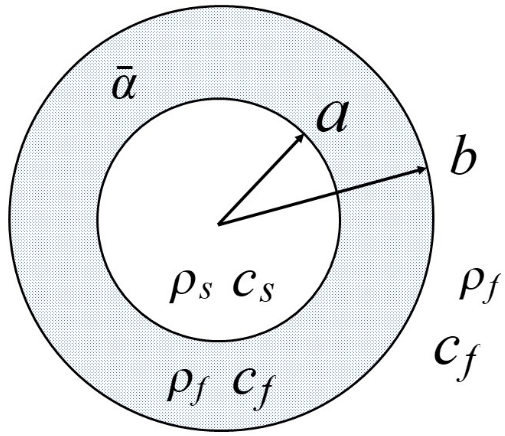

Figure 2.1: Schematic of an optically transparent fluid sphere of radius a with a density ρ_s and sound speed c_s. The droplet is surrounded by an optically absorbing spherical region of radius b having an optical absorption coefficient $\bar{\alpha}$, density ρ_f and sound speed c_f. The larger diameter sphere is, in turn, surrounded by a transparent region that extends from b to infinity with the same acoustic properties as the absorbing region.

coefficient, C_P is the specific heat capacity, and H is the heating function with dimensions of energy per unit time and volume. Note that the effect of surface tension, which would have the effect of addition of a constant pressure differential [88], is not considered. The sphere is irradiated by an optical beam of intensity I_0 modulated at a frequency ω. If the heating function and the pressure for the region between a and b is taken to be $H = \bar{\alpha} I_0 \exp(-i\omega t)$ and $p = \tilde{p} \exp(-i\omega t)$, respectively, the wave equation becomes a Helmholtz equation of the form

$$(\nabla^2 + k^2)\tilde{p} = i\frac{\bar{\alpha}\beta I_0 \omega}{C_P^{(f)}}, \tag{2.2}$$

where $k = \omega/c$. For the absorbing region, the space derivatives in Eq. (2.2) can be set to zero to give a solution to the inhomogeneous Helmholtz equation for $\tilde{p}$. When the exponential factor is then included, the frequency domain pressure corresponding to $\tilde{p}$ becomes

$$\tilde{P}^F = \frac{i\tilde{P}_f}{q\hat{c}} e^{-iq\hat{t}} \quad \text{where} \quad \tilde{P}_f = \frac{\bar{\alpha}\beta I_0 c_f a}{C_P^{(f)}}, \tag{2.3}$$

where $C_P^{(f)}$ is the specific heat capacity of the the fluid in the absorbing region, and a dimensionless frequency q and time $\hat{t}$ have been defined as

$$q = \frac{\omega a}{c} \quad \text{and} \quad \hat{t} = \frac{c_s}{a} t. \tag{2.4}$$

Thus, for the frequency domain pressures in the sphere $\bar{p}_s$, the absorbing layer $\bar{p}_f$, and external region $\bar{p}_e$, the solutions to the wave equation [89] are

$$\bar{p}_s = \tilde{P}^F \hat{P}_s j_0(k_s r), \tag{2.5}$$

$$\bar{p}_f = \tilde{P}^F [1 + \hat{P}_f^{(1)} h_0^{(1)}(k_f r) + \hat{P}_f^{(2)} h_0^{(2)}(k_f r)], \tag{2.6}$$

$$\bar{p}_e = \tilde{P}^F \hat{P}_e h_0^{(1)}(k_f r), \tag{2.7}$$

where the four quantities $\hat{P}$ are constants multiplying the solutions to the homogeneous wave equation, j_0 is a spherical Bessel function, $h_0^{(1)}$ and $h_0^{(2)}$ are zero order spherical Hankel functions, and where the following dimensionless parameters have been defined for the problem as

$$\hat{c} = \frac{c_s}{c_f} \quad \text{and} \quad \hat{\rho} = \frac{\rho_s}{\rho_f}. \tag{2.8}$$

Quantities in the sphere have been given subscripts s, those in the absorbing layer f, and those in the external region, e.

The constants multiplying the homogeneous solutions in Eqs. (2.5, 2.6, 2.7) are found by employing the conservation equations for the continuity of pressure and acceleration at interfaces [88], the latter reducing to the $\nabla p/\rho$. For the interfaces at a and b, these equations are

$$\hat{P}_s j_0(k_s a) = 1 + \hat{P}_f^{(1)} h_0^{(1)}(k_f a) + \hat{P}_f^{(2)} h_0^{(2)}(k_f a), \tag{2.9}$$

$$\hat{P}_s j_0'(k_s a) = \hat{\rho}\hat{c}[\hat{P}_f^{(1)} h_0^{(1)\prime}(k_f a) + \hat{P}_f^{(2)} h_0^{(2)\prime}(k_f a)], \tag{2.10}$$

$$\hat{P}_e h_0^{(1)}(k_f b) = 1 + \hat{P}_f^{(1)} h_0^{(1)}(k_f b) + \hat{P}_f^{(2)} h_0^{(2)}(k_f b), \tag{2.11}$$

$$\hat{P}_e h_0^{(1)\prime}(k_f b) = \hat{P}_f^{(1)} h_0^{(1)\prime}(k_f b) + \hat{P}_f^{(2)} h_0^{(2)\prime}(k_f b). \tag{2.12}$$

Without the assumption of identical sound speeds and densities for the absorbing and infinite regions extremely complicated expressions for the photoacoustic pressures resulted; consequently, the assumption that these quantities be identical was chosen.

The solution of Eqs. (2.9, 2.10, 2.11, 2.12) for the four $\hat{P}$ parameters gives lengthy expressions, the only one of interest here being that for $\hat{P}_s$, which is found [1] to be

$$\hat{P}_s = \frac{N}{D}, \tag{2.13}$$

$$\begin{aligned} N = {} & \hat{\rho}\hat{c}[h_0^{(1)\prime}(k_f a) h_0^{(1)\prime}(k_f b) h_0^{(2)}(k_f a) - h_0^{(1)\prime}(k_f a) h_0^{(1)\prime}(k_f b) h_0^{(2)}(k_f b) \\ & - h_0^{(1)\prime}(k_f a) h_0^{(1)\prime}(k_f b) h_0^{(2)\prime}(k_f a) + h_0^{(1)\prime}(k_f b) h_0^{(1)\prime}(k_f a) h_0^{(2)\prime}(k_f b)] \end{aligned}$$

and

$$D = [h_0^{(1)\prime}(k_f b) h_0^{(2)}(k_f b) - h_0^{(1)}(k_f b) h_0^{(2)\prime}(k_f b)] \times [h_0^{(1)}(k_f a) j_0'(k_s a) - h_0^{(1)\prime}(k_f a)\, j_0(k_s a)\hat{\rho}\hat{c}].$$

[1] Extensive algebraic manipulation is required to solve the four equations; therefore Mathematica was used to find the solution.

It is convenient to express $\hat{P}_s$ in terms of the dimensionless parameters

$$k_f a = q\hat{c} \quad k_f b = q\hat{c}\hat{b} \quad \hat{b} = b/a \quad \hat{r} = r/a. \tag{2.14}$$

After substitution for explicit forms of the spherical Bessel functions, $j_0(x) = \sin(x)/x$, $h_0^{(1)}(x) = \exp(ix)/(ix)$, $h_0^{(2)}(x) = \exp(-ix)/(-ix)$, and their derivatives into Eq. (2.13) and simplification of the result, the frequency domain photoacoustic pressure within the sphere is found to be

$$\bar{p}_s = 2\tilde{P}_f(\frac{\hat{\rho}}{\hat{c}})\frac{\sin(q\hat{r})}{q\hat{r}}\left[\frac{(1-i\hat{c}q)e^{iq} - (1-i\hat{c}qb)e^{iq(\hat{c}b-\hat{c}+1)}}{[(1-\hat{\rho}) + iq(1+\hat{\rho}\hat{c})][1+Re^{2iq}]}\right]e^{-iq\hat{t}}, \tag{2.15}$$

where R is an amplitude reflection coefficient for a spherical wave at a spherical interface given by

$$R = \frac{-(1-\hat{\rho}) + iq(1-\hat{\rho}\hat{c})}{(1-\hat{\rho}) + iq(1+\hat{\rho}\hat{c})}. \tag{2.16}$$

Note that the factor containing R in the denominator of Eq. (2.15) can be expanded in an infinite series, which in the time domain results in time delays in the pulse sequence within the sphere.

If $\hat{\rho}$ is set to unity, it is possible to obtain the inverse Fourier transform of Eq. (2.15) in analytic form [2]. In taking the Fourier transform of the frequency domain pressure it is to be noted that the integration over ω means that $\tilde{P}_f$ becomes $\bar{\alpha}\beta E_0 c_f^2\hat{c}/C_P^{(f)}$ so that the time domain photoacoustic pressure response to a delta function heating pulse becomes

$$p_s = -P_f\frac{1}{2\hat{r}(1+\hat{c})}\sum_{n=0}^{\infty}(-R')^n\sum_{i=1}^{4}F_i(2n), \tag{2.17}$$

where P_f, with dimensions of pressure, R', the equal density reflection coefficient, and

[2] Extensive algebraic manipulation is requred to solve the four equations; therefore Mathematica was used to find the solution.

the functions F are given by

$$
\begin{aligned}
P_f &= \frac{\bar{\alpha}\beta E_0 c_f^2}{C_P^{(f)}}, \qquad R' = \frac{1-\hat{c}}{1+\hat{c}}, && (2.18)\\
F_1(n) &= (1+n-\hat{c}-\hat{r}-\hat{t})sgn(\hat{r}+\hat{t}-1-n), && (2.19)\\
F_2(n) &= (1+n-\hat{c}+\hat{r}-\hat{t})sgn(\hat{r}-\hat{t}+1+n), && (2.20)\\
F_3(n) &= (-1-n+\hat{c}-\hat{r}+\hat{t})sgn(1+\hat{c}(\hat{b}-1)+n+\hat{r}-\hat{t}), && (2.21)\\
F_4(n) &= (-1-n+\hat{c}+\hat{r}+\hat{t})sgn(-1-\hat{c}(\hat{b}-1)-n+\hat{r}+\hat{t}), && (2.22)
\end{aligned}
$$

where $\mathrm{sgn}(x)$ is the sign function defined as -1, 0, or 1 depending whether x is negative, zero, or positive.

The results of the calculation for three positions within the droplet are shown in Fig. 2.2. It can be seen that where $\hat{r}$ is small, the pressure takes on large values, which, given the $\hat{r}^{-1}$ dependence of the pressure amplitude in the prefactor of Eq. 2.17 indicates that the pressure transients are essentially unbounded. Fig. 2.2 is plotted for a sufficiently large value of $\hat{b}$ that the effects of waves emanating at the interface between the absorbing layer and the external region do not arrive on the time scale plotted. For longer times or smaller values of $\hat{b}$ additional waves appear that have substantial rarefactions. When $\hat{c}$ is given values less than one, e.g. 0.2, for small values of $\hat{r}$ a series of square wave compressions with large spikes of high amplitude compressions and rarefactions appear. When $\hat{r}$ is near unity a series of triangular waves are found. For the case $\hat{c} = 1$ and $\hat{b} = 5$, $\hat{r} = 0.001$, Eq. 2.17 yields a compressive square wave starting at $\hat{t} = 1$ and ending at $\hat{t} = 5$, preceded by a compressive spike at $\hat{t} = 1$ and followed by a rarefaction spike at $\hat{t} = 5$. For larger values of $\hat{b}$, the square wave extends farther out in time to whatever value of $\hat{b}$ that is used.

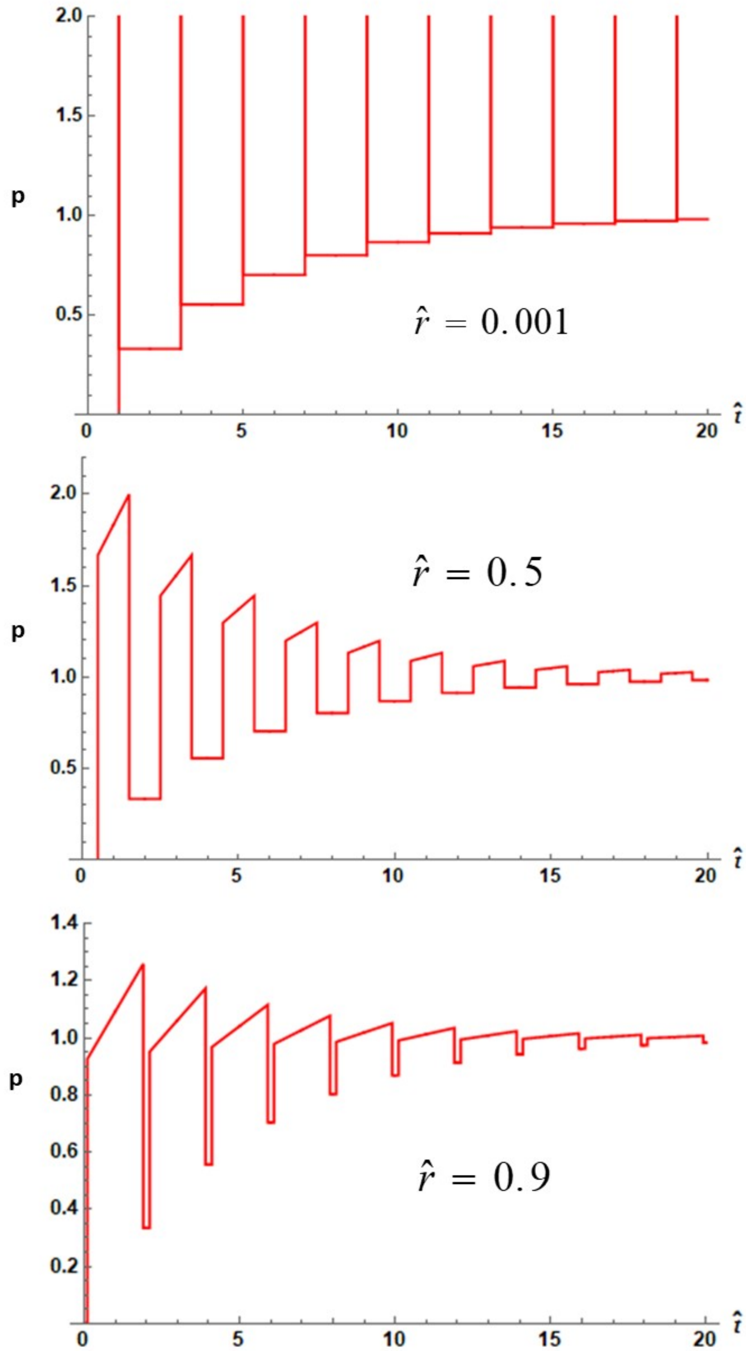

Figure 2.2: Dimensionless photoacoustic pressure versus dimensionless time from Eq. 2.17 with 40 terms in the summation for $\hat{c} = 5$ with P_f set to one. The top plot is truncated since the peak pressure reaches a value of approximately 800.

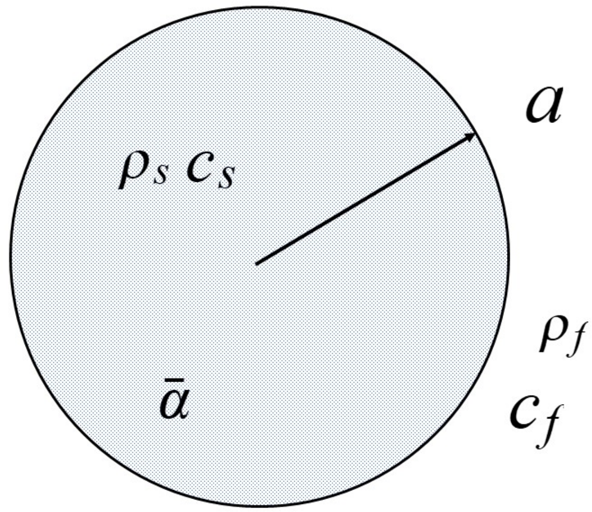

Figure 2.3: Schematic of an optically thin fluid sphere of radius a with an optical absorption coefficient $\bar{\alpha}$, density ρ_s and sound speed c_s surrounded by an infinite medium with density ρ_f and sound speed c_f.

2.2.2 Photoacoustic effect generated by excited spherical droplets in fluids

Determination of the photoacoustic effect from an optically thin, absorbing sphere (as shown in Fig. 2.3) has been reported in Ref. [81] as noted above. The frequency domain photoacoustic pressure inside the sphere is given by

$$\bar{p}_s = \tilde{P}_s \frac{i}{q}\left[1 + \frac{\hat{\rho}(1 - i\hat{c}q)(\sin q\hat{r}/q\hat{r})}{(1-\hat{\rho})\sin q/q - \cos q + i\hat{\rho}\hat{c}\sin q}\right] e^{-iq\hat{t}}, \tag{2.23}$$

where

$$\tilde{P}_s = \frac{\bar{\alpha}\beta I_0 c_s a}{C_P^{(s)}}, \tag{2.24}$$

and where $C_P^{(s)}$ is the specific heat capacity of the fluid in the sphere. Substitution of exponential functions for the sine and cosine functions in Eq. (2.23) yields

$$\bar{p}_s = \tilde{P}_s\left[\frac{i}{q} + \frac{2\hat{\rho}(1 - i\hat{c}q)(\sin q\hat{r}/q\hat{r})e^{iq}}{[(1-\hat{\rho}) + iq(1+\hat{\rho}\hat{c})][1 + Re^{2iq}]}\right]e^{-iq\hat{t}}, \tag{2.25}$$

which in the limit where $\hat{\rho} = 1$ gives

$$\bar{p}_s = \tilde{P}_s\left[\frac{i}{q} + \frac{2(1 - i\hat{c}q)(\sin q\hat{r}/q\hat{r})e^{iq}}{iq(1+\hat{c})[1 + R'e^{2iq}]}\right]e^{-iq\hat{t}}. \tag{2.26}$$

As above, it is possible to obtain an analytic form solution for the Fourier transform of Eq. (2.26). The photoacoustic pressure within the sphere is found to be

$$p_s = P_s\left\{\frac{sgn(\hat{t})}{2} + \frac{1}{2\hat{r}(1+\hat{c})}\sum_{n=0}(-R')^n[G_1(2n+1) + G_2(2n+1)]\right\}, \tag{2.27}$$

where

$$G_1(n) = (\hat{c} - n - \hat{r} + \hat{t})sgn(\hat{t} - \hat{r} - n), \tag{2.28}$$

$$G_2(n) = (n - \hat{c} - \hat{r} - \hat{t})sgn(\hat{t} + \hat{r} - n), \tag{2.29}$$

and

$$P_s = \frac{\bar{\alpha}\beta E_0 c_s^2}{C_P^{(s)}}. \tag{2.30}$$

The frequency domain pressure in the surrounding fluid can be found from the acoustic conservation equations at the interface, as above, to be

$$\bar{p}_f = \tilde{P}_s\frac{2(\sin q - q\cos q)/q}{\hat{r}[(1-\hat{\rho}) + iq(1+\hat{\rho}\hat{c})][1 + Re^{2iq}]}e^{-iq(\hat{\tau}-1)}, \tag{2.31}$$

where $\hat{\tau} = \hat{t} - \hat{c}(\hat{r} - 1)$ is the retarded time from the perimeter of the sphere. Fourier transformation of Eq. (2.31) into the time domain with $\hat{\rho} = 1$ yields

$$p_f = P_s \frac{1}{2\hat{r}(1+\hat{c})} \sum_{n=0}^{\infty} (-R')^n [H_1(2n+1) + H_2(2n+1)], \tag{2.32}$$

where

$$\begin{aligned} H_1(n) &= (n + \hat{c}(\hat{r}-1) - \hat{t}) sgn(1 + n + c(\hat{r}-1) - \hat{t}), && (2.33) \\ H_2(n) &= (n + \hat{c}(\hat{r}-1) - \hat{t}) sgn(1 - n - c(\hat{r}-1) + \hat{t}). && (2.34) \end{aligned}$$

The photoacoustic pressures calculated from Eq. (2.32) and Eq. (2.27) are found to be identical as $\hat{r}$ approaches one.

Several plots of pressure versus dimensionless time from Eq. (2.27) are given in Fig. 2.4. Unlike the case for the externally irradiated sphere, at small values of $\hat{r}$, the transients are high amplitude rarefactions. As $\hat{r}$ approaches unity, the wave takes on the character of a series of repeated N-shaped waves, which appear in time with the sharp spikes in amplitude diminished or non-existent. The series of repeated N-shaped waves with diminishing amplitude resemble the emitted waves found from Eq. (2.32), as described in Ref. [81].

2.2.3 Discussion for photoacoustically excited droplet

The large amplitude waves reported here follow as a consequence of spherical wave propagation to the center of the droplet, as is explicit in the time domain expressions derived above. Analytic Fourier transforms of the complete frequency domain expressions that include density differences could not be found; however, their numerical Fourier transforms as well as experimental results [80] show that the effect of density differences in the two fluids is to give qualitatively the same waveforms

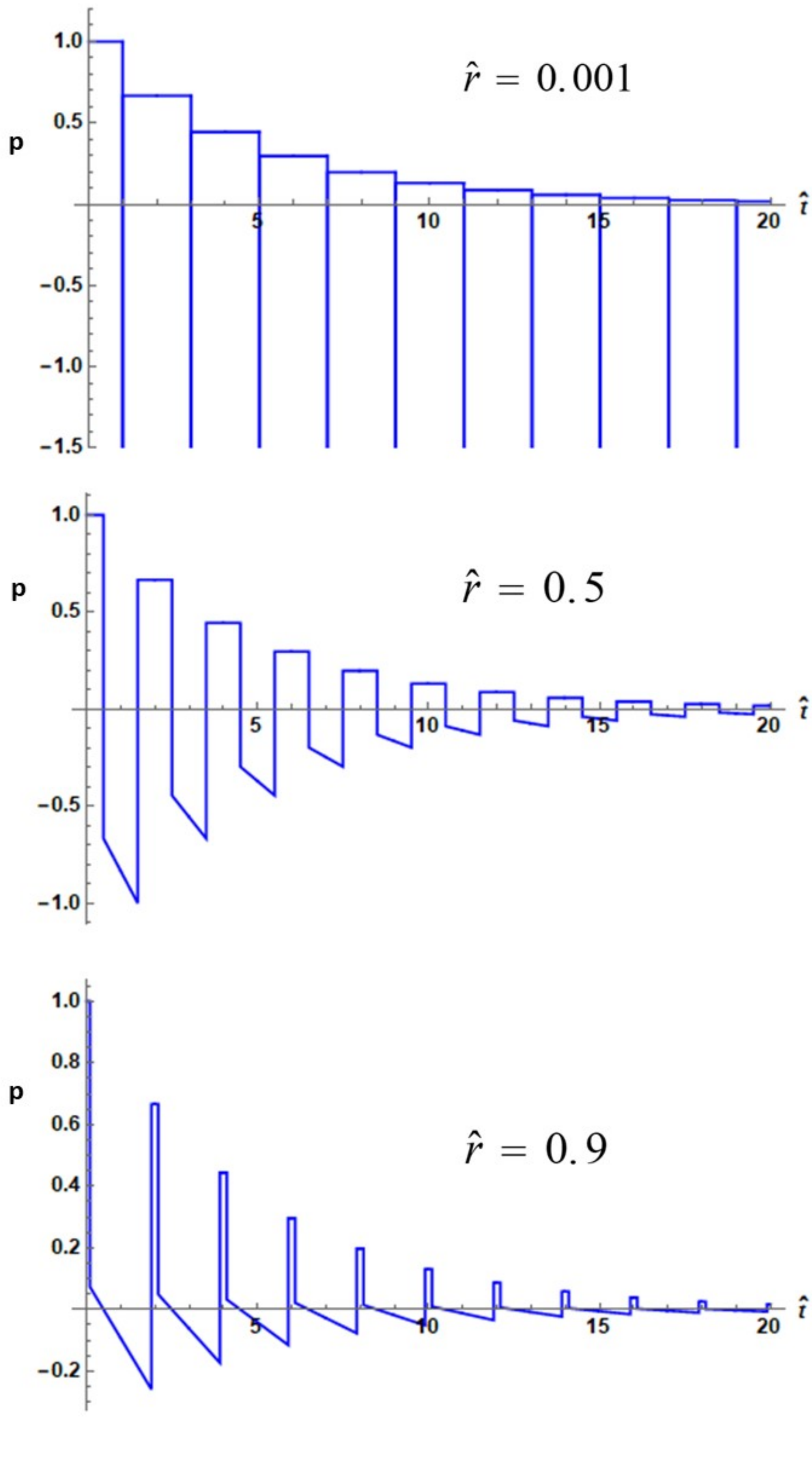

Figure 2.4: Dimensionless photoacoustic pressure with P_s set to unity versus dimensionless time from Eq. 2.27 with 40 terms in the summation with $\hat{c} = 5$. The top plot is truncated as the first peak reaches a value of approximately -800.

calculated from Eq. (2.32), but with curvature on the repeated waveforms, as opposed to strictly triangular features, with the curvature becoming more pronounced for each repetition of the initial wave. The origin of the difference in waveform shape for the two cases where the density ratio is unity or departs from this value is that the reflection coefficient R is frequency dependent whereas R' is not. Thus when the fluids have identical densities, features of the waveforms repeat in time. For unequal densities the frequency dependence of R results in different degrees of filtering of the different components of the frequency spectrum in the wave at each reflection.

According to Ref. [87], for two and three-dimensional waves the time integral of the pressure must be zero, that is,

$$\int p(t)dt = 0. \tag{2.35}$$

In order to insure that this integral be zero, a non-absorbing layer of fluid that extends from b to infinity was considered. Had the absorbing layer been of finite extent the pressure integral would become a constant. It is easily verified by numerical integration that the integrals of the pressure in the time domain expressions given above vanish, although this is not evident in Fig. 2.2, which shows only the initial compressive features. However, if large values of $\hat{t}$ are included in the plot so that the wave emanating from the boundary at b becomes visible, a second wave with significant rarefactions is found. Fig. 2.5 shows an example of this cancellation over the range of $\hat{t} = 0$ to 40. The dimensionless pressure numerically integrated over this range gives a value of 0.3; if the integration range is extended to $\hat{t} = 80$ the integral becomes 2×10^{-6}.

The pressure amplitudes P_f and P_s are prefactors in the expressions for the time domain expressions for both problems treated here and multiply the dimensionless

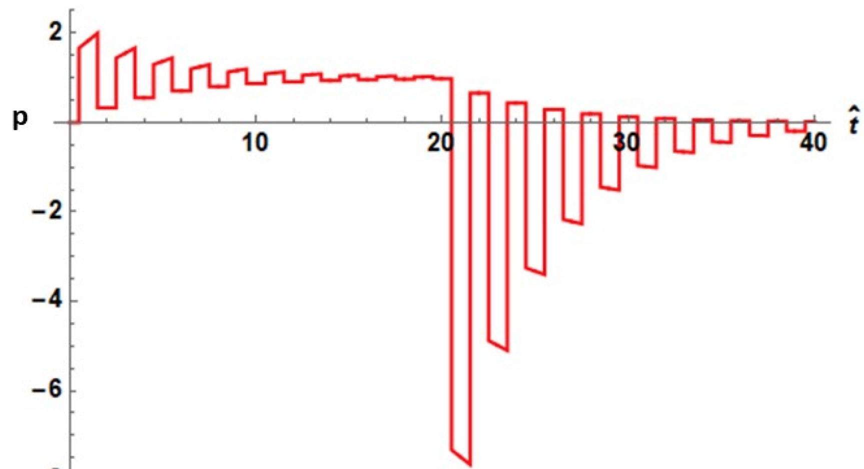

Figure 2.5: Dimensionless pressure versus $\hat{t}$ from Eq. 2.17 evaluated with $\hat{c} = 5$.

amplitudes given in the pressure plots to give the actual photoacoustic pressure. In so far as experimental generation of shock waves within a droplet is concerned, it is easily found that the factors P_f and P_s for hexane with an absorption of 1 mm^{-1} irradiated by laser with a fluence of 1 J/cm^2 results in a pressure of 240 atm. This figure presupposes that the laser pulse width be much smaller than the transit time of sound across the droplet. The 240 atm figure when multiplied by the peak values of the large transient spikes shown in Fig. 2.2 suggest that shock wave production is highly likely. A factor to consider however is that the results given here have been derived for a perfect sphere whose index of refraction matches that of the surrounding fluid. Departure from sphericity will change somewhat the time dependence of the spikes and their amplitudes. Any mismatch in index of refraction or departure from the condition that the absorber be optically thin will result in a non-uniform heat deposition within the droplet, either of which will act to reduce the amplitude of the pressure spikes.

In addition to extension of the study of the acoustics of the laser irradiated droplet to the pressure within droplets, part of the motivation for this investigation has been to point out production of large amplitude compressions and rarefactions within a droplet. The possibility exists for manipulating biological objects such as cells placed at the centers of droplets with the high amplitude acoustic waves that have been shown to exist. In any experimental verification of the above results it should be noted that the size of the droplet strongly influences the frequency spectrum of the emitted photoacoustic wave. The experimental investigations referenced in Section 2.1 showed that ultrasonic waves emitted from objects with dimensions of millimeters generated waves with features on the order of microseconds; more recent experiments with micron sized particles [90] showed the ultrasonic waveforms possessed compressions and rarefactions on the nanosecond time scale. The frequency response of the detection is thus governed not only the duration of the transients as shown in Figs. 2.2 and 2.4, but also by the size of the droplet.

2.2.4 1D and 3D Visualizations of the emitted sphere pressures

Here the emitted sphere pressures in equal densities cases in one and three dimensions are plotted. Figure 2.6 shows the emitted sphere pressure signals in the time domain with parameters in Fig. 2.6 (a) $\hat{c} = 5$, $\hat{r} = 2$ and (b) $\hat{c} = 2$, $\hat{r} = 2$. It's clear that in both cases an N-shape wave feature appears in the plots. The N-shape wave has been a key feature concerning the pressure wave emitted from photoacoustically excited spherical droplets. The pressure integration with time should be zero as predicted according to Ref. [87]. It is straightforward to check that fast Fourier transform of the frequency domain solution matches the time domain solution from the derived analytical formula.

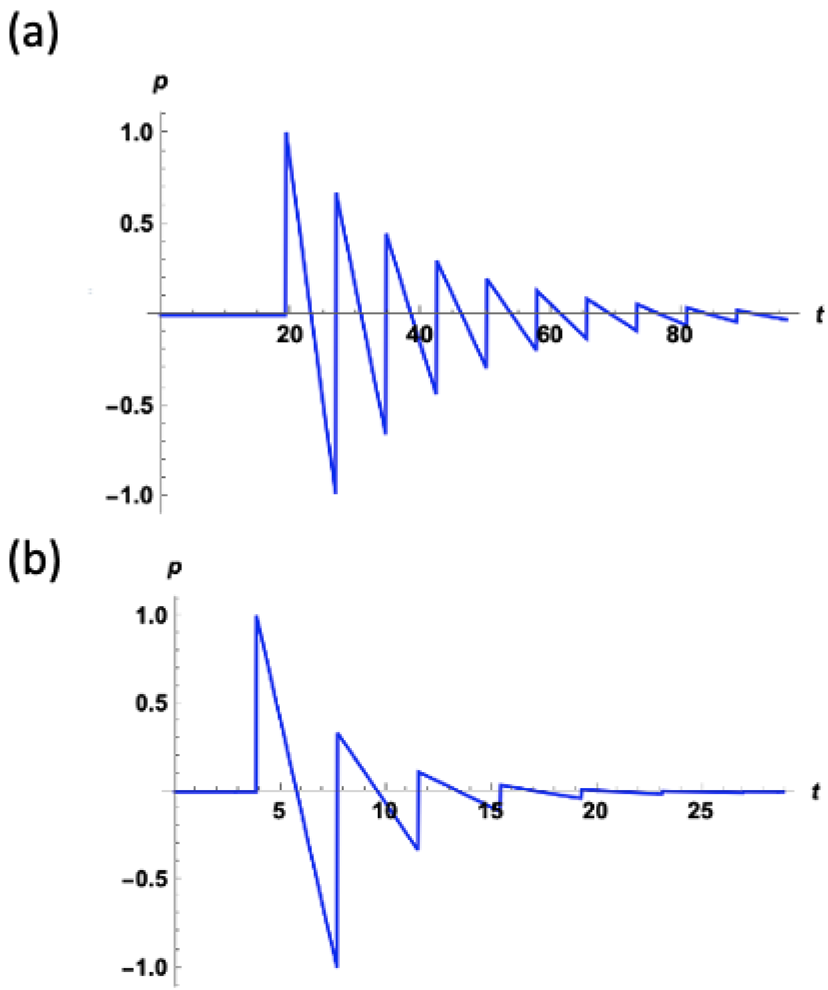

Figure 2.6: N-shape emitted pressure waves in the time domain with (a) $\hat{c} = 5$ and $\hat{r} = 2$, (b) $\hat{c} = 2$ and $\hat{r} = 2$.

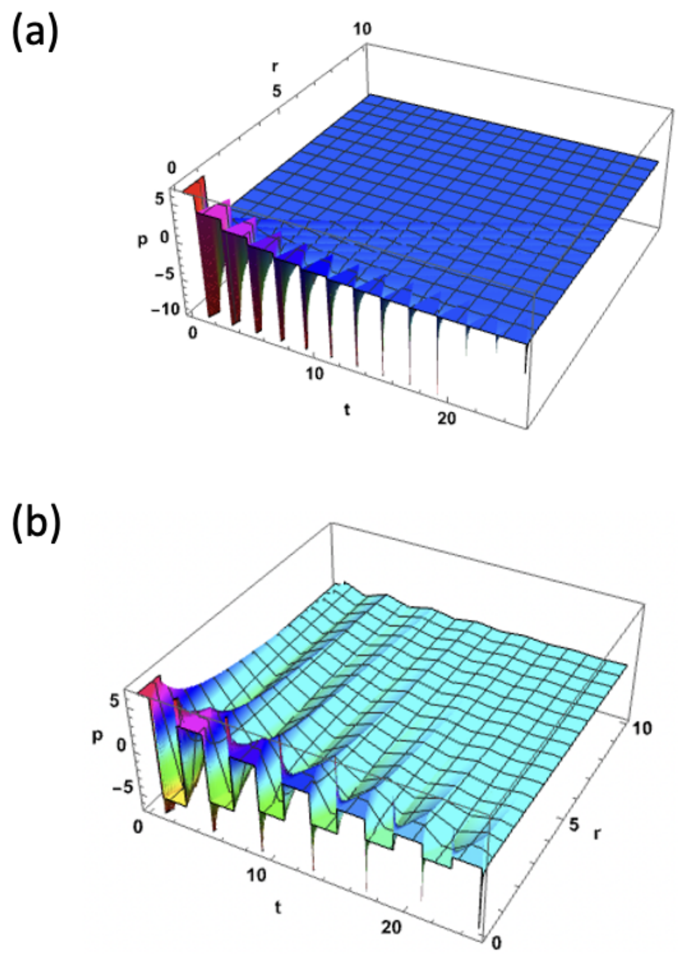

Figure 2.7: 3D Visualization of external radiated pressure with (a) $\hat{c} = 5$, (b) $\hat{c} = 0.1$.

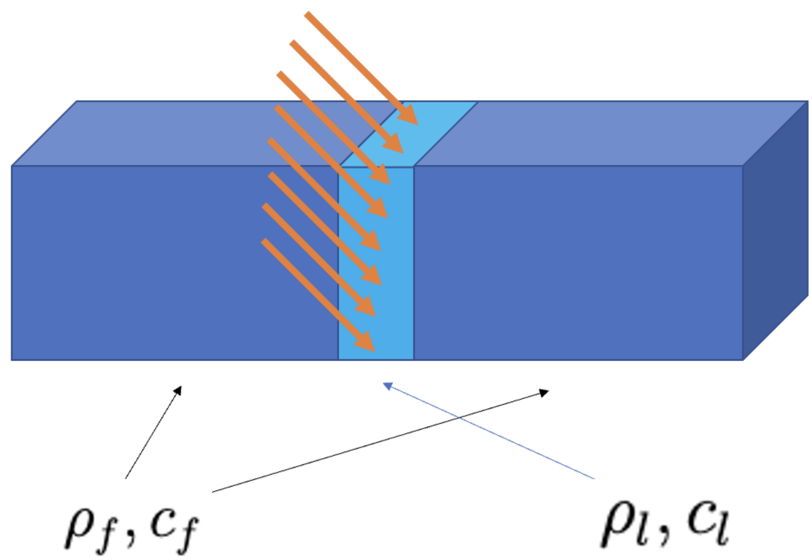

Figure 2.8: Optical thin fluid layer with density ρ_l and sound speed c_l surrounded by transparent fluid layer with density ρ_f and sound speed c_f.

For 3D external pressure, the case of $\hat{c} = 5$ is shown in Fig. 2.7 (a) and $\hat{c} = 0.1$ is shown in Fig. 2.7 (b). When $\hat{c} = 5$, the transient rarefactions at time $t = 1, 3, 5, 9...$ can be observed. Transient compressions and rarefactions at edges where the $1/r$ dependence can be seen in Fig. 2.7 (b) with $\hat{c} = 0.1$.

2.3 Photoacoustic effect generated by fluid layers

In Section 2.2, the production of high amplitude compressions and rarefactions within a droplet has been investigated. A natural question that arises is whether the structures different from the spherical droplets inside fluids, for example, the layered fluid structures would produce high amplitude transients as in the photoacoustically excited droplets.

The photoacoustic effects can also be generated by absorption of laser radiation in optically thin layers [91]. As shown in Fig. 2.8, an optically thin fluid layer is surrounded by another transparent fluid layer. Denote $\hat{\rho} = \frac{\rho_l}{\rho_f}$ and $\hat{c} = \frac{c_l}{c_f}$ where ρ_l and c_l are the density and sound speed in the absorbing fluid layer, ρ_f and c_f are the density and sound speed in the surrounding fluid layer. Assume the layer is heated by a laser beam with intensity modulation at frequency ω, the heating function is described as $H = \alpha I_0 e^{-i\omega t}$ where α is the optical absorption coefficient of the fluid layer. The photoacoustic pressure generated in the middle fluid layer is given by Ref. [91],

$$p_L = \frac{i\lambda}{\hat{q}}\left(1 - \frac{i\hat{\rho}\hat{c}\cos\hat{q}\hat{z}}{\sin\hat{q} + i\hat{\rho}\hat{c}\cos\hat{q}}\right)e^{-i\hat{q}\hat{t}}, \tag{2.36}$$

where λ is an amplitude factor, $\hat{q}$ is the normalized frequency and $\hat{t}$ is the dimensionless time and the other parameters are defined as $\lambda = \frac{\alpha\beta I_0 c_l l}{2C_p}$, $\hat{q} = \frac{\omega l}{2c_l}$, $\hat{t} = \frac{2c_l t}{l}$ and $\hat{z} = \frac{2z}{l}$.

Denote amplitude reflection coefficient as $R = \frac{1-\hat{\rho}\hat{c}}{1+\hat{\rho}\hat{c}}$ and transmission coefficient as $T = \frac{2\hat{\rho}\hat{c}}{1+\hat{\rho}\hat{c}}$ as given in Ref. [92], by simple algebra, the denominator D can be written as

$$D = \sin\hat{q} + i\hat{\rho}\hat{c}\cos\hat{q} = \frac{e^{i\hat{q}} - e^{-i\hat{q}}}{2i} + \frac{i\hat{\rho}\hat{c}}{2}(e^{i\hat{q}} + e^{-i\hat{q}}) = \frac{i}{2}e^{-i\hat{q}}(1+\hat{\rho}\hat{c})(1 - Re^{2i\hat{q}}). \tag{2.37}$$

Hence the photoacoustic pressure in the middle layer p_L in Eq. 2.36 can be written as a function of reflection and transmission coefficients,

$$p_L = \frac{i\lambda}{\hat{q}}e^{-i\hat{q}\hat{t}}\left(1 - \frac{i\hat{\rho}\hat{c}\cos\hat{q}\hat{z}}{\frac{i}{2}e^{-i\hat{q}}(1+\hat{\rho}\hat{c})(1 - Re^{2i\hat{q}})}\right) = \frac{i\lambda}{\hat{q}}e^{-i\hat{q}\hat{t}} - i\lambda T\frac{\cos\hat{q}\hat{z}e^{-i\hat{q}\hat{t}+i\hat{q}}}{\hat{q}(1 - Re^{2i\hat{q}})}. \tag{2.38}$$

Fourier transformation of Eq. 2.38 yields the layer pressure in the time domain,

$$p_L(t) = \lambda\left(\pi\,\mathrm{sgn}(t) - \frac{\pi T}{2}\sum_{n=0}^{\infty} R^n\big(\mathrm{sgn}(t+z-2n-1) + \mathrm{sgn}(t-z-2n-1)\big)\right). \tag{2.39}$$

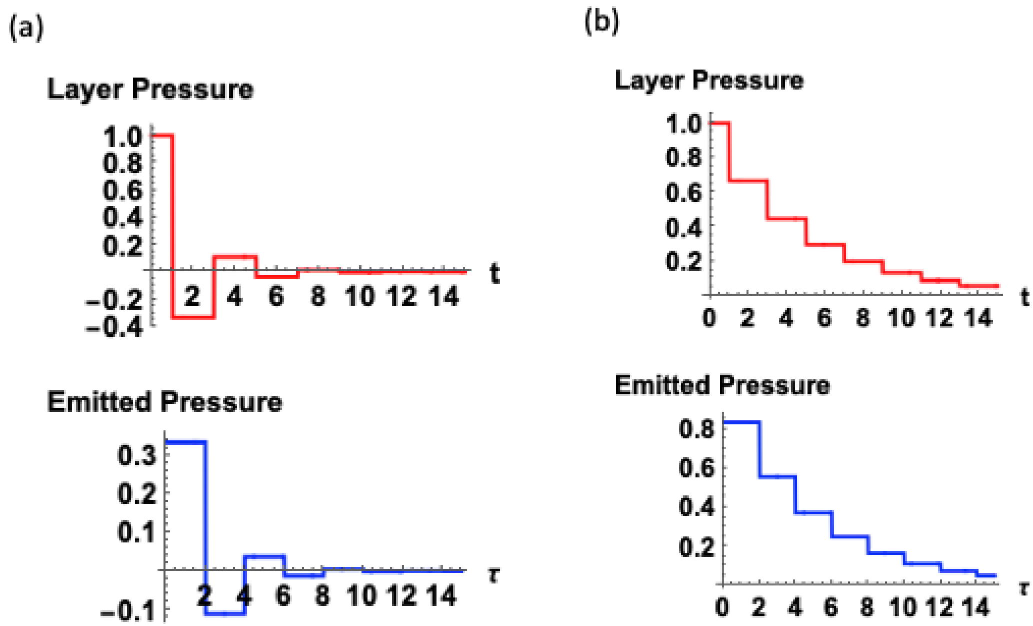

Figure 2.9: Internal layer pressure and the emitted pressure with (a) $\hat{c} = 2$ and $\hat{\rho} = 1$ and (b) $\hat{c} = 0.2$ and $\hat{\rho} = 1$.

Similarly, the emitted layer pressure which is denoted by p_E is given by Ref. [91],

$$p_E(\hat{\tau}) = \frac{2\pi\lambda}{1 + \hat{\rho}\hat{c}} \sum_{n=0}^{\infty} R^n \Theta_{2n,2n+2}(\hat{\tau}), \tag{2.40}$$

where $\Theta_{a,b}$ is the step function that is only nonzero over the finite interval $[a, b]$ and $\hat{\tau}$ is the dimensionless retarded time which is define as $\hat{\tau} = \frac{2c_l}{l}\left(t - \frac{z-l/2}{c_f}\right)$.

Figure 2.9 shows the internal and emitted pressures generated by fluid layers where the plots show the apparent features of step functions. As opposed to the layered spherical droplets cases, there is no evidence of high pressure compression or rarefaction generation. The different time domain responses for various fluid parameters can be used to infer the fluid properties.

2.4 Photoacoustic effect generated by an oscillating optical source in a one-dimensional resonator

Although the photoacoustic effect is most commonly generated by pulsed or amplitude modulated continuous optical sources, it is possible to generate acoustic waves by moving a constant amplitude continuous light beam. If the light beam moves at the speed of sound, an amplification effect takes place which can be used to advantage in trace gas detection. Here, in a related problem, the properties of the photoacoustic effect are investigated for a continuous optical beam that is moved in a one-dimensional resonator. The solution shows the additive effects of sweeping the optical beam the length of the cell and back.

Photoacoustic trace gas detection has a rich history dating from the 1960's. The research on this subject, which has been reviewed numerous times [11–13], has focused on optical excitation schemes and the design of the resonator with the goal of providing the highest possible sensitivity. Recently, the use of a moving infrared optical grating has been employed to generate the photoacoustic effect in the hundreds of kilohertz range in a cavity with a resonant piezoelectric crystal used as the detector [55]. In this device a principle formulated by Gusev and Karabutov [3] where the optical source is made to move at the sound speed results in coherent addition of the instantaneously produced light induced pressure wave with the traveling pressure wave generated at a previous time was used to advantage. The reported detection limit for this device is in the parts per quadrillion range for SF_6, however, the instrument uses expensive technology and requires a crystal detector that is not at this point commercially available. As a result, it was decided to investigate the principles of

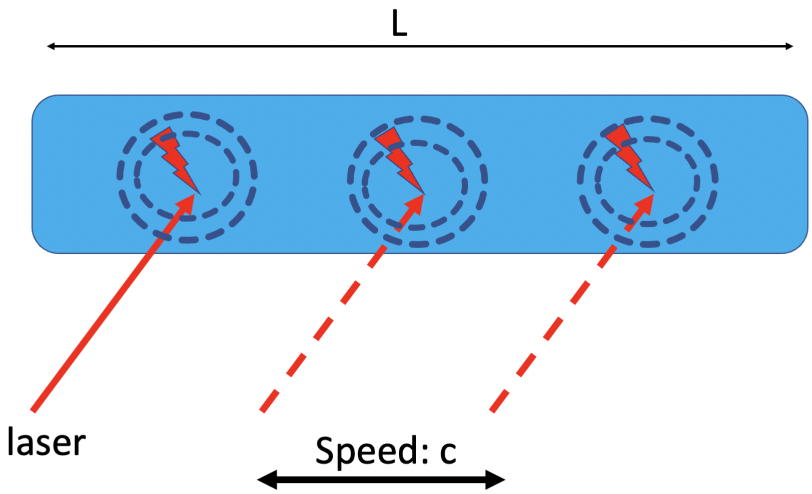

Figure 2.10: Scheme of oscillating sources in a one-dimensional resonator. The laser moves at the speed of sound c back and forth along the axis dimension of resonator

operation of a longitudinal resonant cavity where a laser beam was directed to move back and forth along the axis of the resonator. Such an instrument would employ a microphone operating in the range of kHz instead of the much higher frequency reported in Ref. [55].

2.4.1 Single delta pulse in a 1D resonator

The motion of the laser beam along the longitudinal resonator can modeled as a summation of delta functions at various z_n which is the coordinate of each moving delta sources. In Section 2.4.1, the case for single delta pulse in a one-dimensional resonator is presented.

Consider a single delta pulse in a one-dimensional resonator that extends from 0 to L, the heating function can be written as $H = I\delta(z - z_0) = I\delta(z - ct) = \frac{I}{c}\delta(t - z/c)$ where I is the energy per unit area and time delivered to the gas, z is the coordinate along the symmetry axis of the resonator, and z_0 is the coordinate of the single moving delta function source. The photoacoustic effect in a inviscid fluid is described by

$$\left(\nabla^2 - \frac{1}{c^2}\frac{\partial^2}{\partial t^2}\right) p = -\frac{\beta}{C_P}\frac{\partial H}{\partial t}, \tag{2.41}$$

where p is the pressure, c is the sound speed, β is the thermal expansion coefficient, C_p is the specific heat capacity, t is the time, and H is the heating function, which describes the energy per unit time and volume deposited by the optical source. The one-dimensional photoacoustic wave equation can be written as,

$$\left(\frac{\partial^2}{\partial z^2} - \frac{1}{c^2}\frac{\partial^2}{\partial t^2}\right)p = -\frac{\beta I}{C_p c}\frac{\partial}{\partial t}\delta(t - z/c). \tag{2.42}$$

Fourier transform of Eq. 2.42 and integration by parts gives

$$\left(\frac{\partial^2}{\partial z^2} + \frac{\omega^2}{c^2}\right) = -\frac{\beta I}{C_p c}\int_{-\infty}^{\infty} e^{-i\omega t}\frac{\partial}{\partial t}\delta(t - z/c)dt \tag{2.43}$$

$$= -\frac{i\omega\beta I}{C_p c}\int_{-\infty}^{\infty} e^{-i\omega t}\delta(t - z/c)dt = -\frac{i\omega\beta I}{C_p c}e^{-i\omega z/c}. \tag{2.44}$$

Denote $k_m = \frac{m\pi}{L}$, the Green's function for one-dimensional resonator can be written as,

$$G(z, z') = \frac{2}{L}\sum_m \frac{\cos k_m z \cos k_m z'}{k^2 - k_m^2}. \tag{2.45}$$

Hence the solution to the wave equation Eq. 2.44 can be obtained by integrating the Green's function over both sides which gives,

$$\tilde{p} = -\frac{i\omega\beta I}{C_p c L}\sum_m \frac{\cos(k_m z)}{k^2 - k_m^2}\int_0^L e^{-i\omega z'/c}\cos(k_m z')dz'. \tag{2.46}$$

Denote the integral in Eq. 2.46 as K_0, evaluation of the integral, we get,

$$K_0 = \int_0^L e^{-i\omega z'/c} \cos(k_m z') dz' \tag{2.47}$$

$$= -\frac{1}{c} \frac{i\omega}{\frac{\omega^2}{c^2} - k_m^2} \left[1 - e^{-i\omega L/c} \cos(k_m L) + e^{-iL\omega/c} \frac{ck_m}{i\omega} \sin(k_m L) \right] \tag{2.48}$$

$$= -\frac{i\omega}{c(\frac{\omega^2}{c^2} - k_m^2)} \Big(1 - e^{-i\omega L/c} r \Big), \tag{2.49}$$

where $r = \cos(k_m L) = (-1)^m$ and $\sin(k_m L) = 0$.

Inverse Fourier transform of Eq. 2.46, the time domain photoacoustic pressure can be derived as,

$$p(t) = \frac{-\beta I}{LC_p c^2} \sum_{m=1}^{M} \cos\Big(\frac{m\pi z}{L}\Big) \left(\frac{c^3 e^{ictk_m} \sqrt{\frac{\pi}{2}} \Big(i - ctk_m + e^{iLk_m}(-1)^m(-i + (L+ct)k_m) \Big)}{2k_m} \right) \tag{2.50}$$

$$= \frac{-\beta I c}{2LC_p} \sum_{m=1}^{M} \frac{\cos(k_m z)}{k_m} \sqrt{\frac{\pi}{2}} e^{ictk_m} \Big[i - ctk_m + e^{iLk_m}(-1)^m(-i + k_m L + ctk_m) \Big]. \tag{2.51}$$

If we take parameters as $z = \frac{L}{2}$, $c = 100$ m/s, $L = 0.1$ m, $\beta = 1$, $C_p = 1$, $I = 1$ and $M = 200$, evaluation of Eq. 2.51 gives Fig. 2.11 and Fig. 2.12. The real part and imaginary parts of a single delta pulse in the time interval of $(0, 0.001s)$ are shown in Fig. 2.11 while longer time intervals $(0, 0.01s)$ show the propagation of acoustic wave in the resonator as shown in Fig. 2.12. These plots verify the correctness of the derived expression Eq. 2.51 for the time domain photoacoustic wave generated by single delta pulse in a one-dimensional resonator. For example, when $z = \frac{L}{2}$, the pressure peaks are observed at 0.5 ms, 1.5 ms, 2.5 ms, 3.5 ms, etc which is predicted in Fig. 2.12 (b). When $z = L$, the pressure peaks are observed at 1 ms, 3 ms, 5 ms, 7ms, etc. Similar mathematics can be applied for the other delta sources, for example, the second delta source $z_1 = L - c(t - L/c) = 2L - ct$. The result for the

$z - z_0 = z - ct$	$\delta(t - \frac{z}{c})$
$z - z_1 = z - 2L + ct$	$\delta(t - [\frac{2L}{c} - \frac{z}{c}])$
$z - z_2 = z + 2L - ct$	$\delta(t - [\frac{2L}{c} + \frac{z}{c}])$
$z - z_3 = z - 4L + ct$	$\delta(t - [\frac{4L}{c} - \frac{z}{c}])$
$z - z_4 = z + 4L - ct$	$\delta(t - [\frac{4L}{c} + \frac{z}{c}])$

Table 2.1: Arguments of the delta functions in Eq. 2.52

summation of all delta sources is presented in Section 2.4.2.

2.4.2 Moving optical sources in a 1D resonator

Consider a one-dimensional resonator that extends from 0 to L irradiated with a laser beam that repeatedly moves the length of the resonator and then reverses direction. For the present problem the heating function is taken to be of the form

$$H(z) = I \sum_n \delta(z - z_n), \tag{2.52}$$

where I is the energy per unit area and time delivered to the gas, z is the coordinate along the symmetry axis of the resonator, and z_n is the coordinate of each of the moving delta function sources. The motion of the laser beam along the z axis is described by the arguments of the delta functions containing the various z_n. Table 2.1 gives values of $z - z_n$ and the corresponding delta function (absent the factor c in the denominator) to be used in Eq. 2.52 for the first few values of n, where the identity $\delta(a - ct) = \delta(t - a/c)/c$ has been used.

The first delta function originates at the left end of the resonator and moves to the right along the z axis. At the time $t = L/c$, the z_1 delta function begins moving from the right end of the resonator traveling to the origin. Thus all of the even numbered entries move from left to right while the odd numbered ones move from the right end

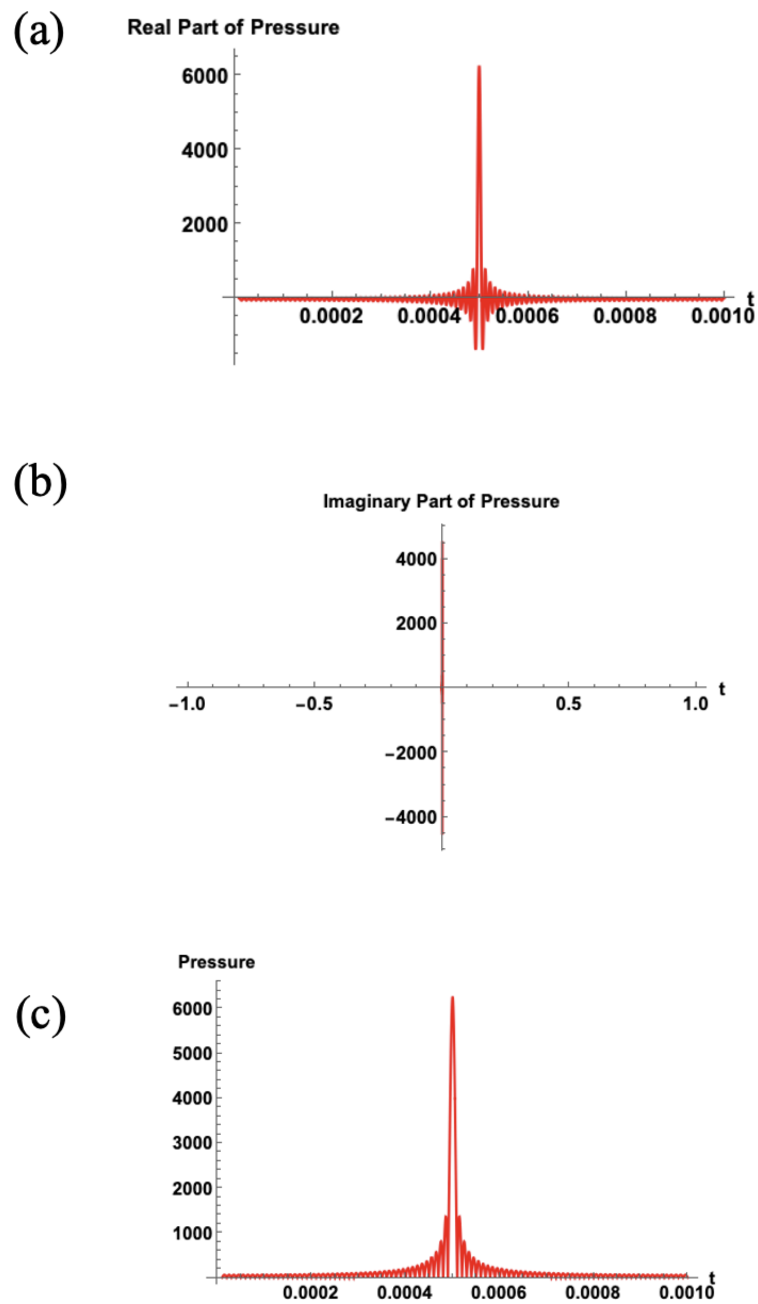

Figure 2.11: Evaluation of the time domain pressure for single delta pulse in a one-dimensional resonator in short time interval (0, 0.001 s) (a) real part of pressure, (b) imaginary part of pressure, (c) the absolute value of pressure. The parameters used are $z = \frac{L}{2}$, $c = 100$ m/s, $L = 0.1$ m, $\beta = 1$, $C_p = 1$, $I = 1$ and $M = 200$.

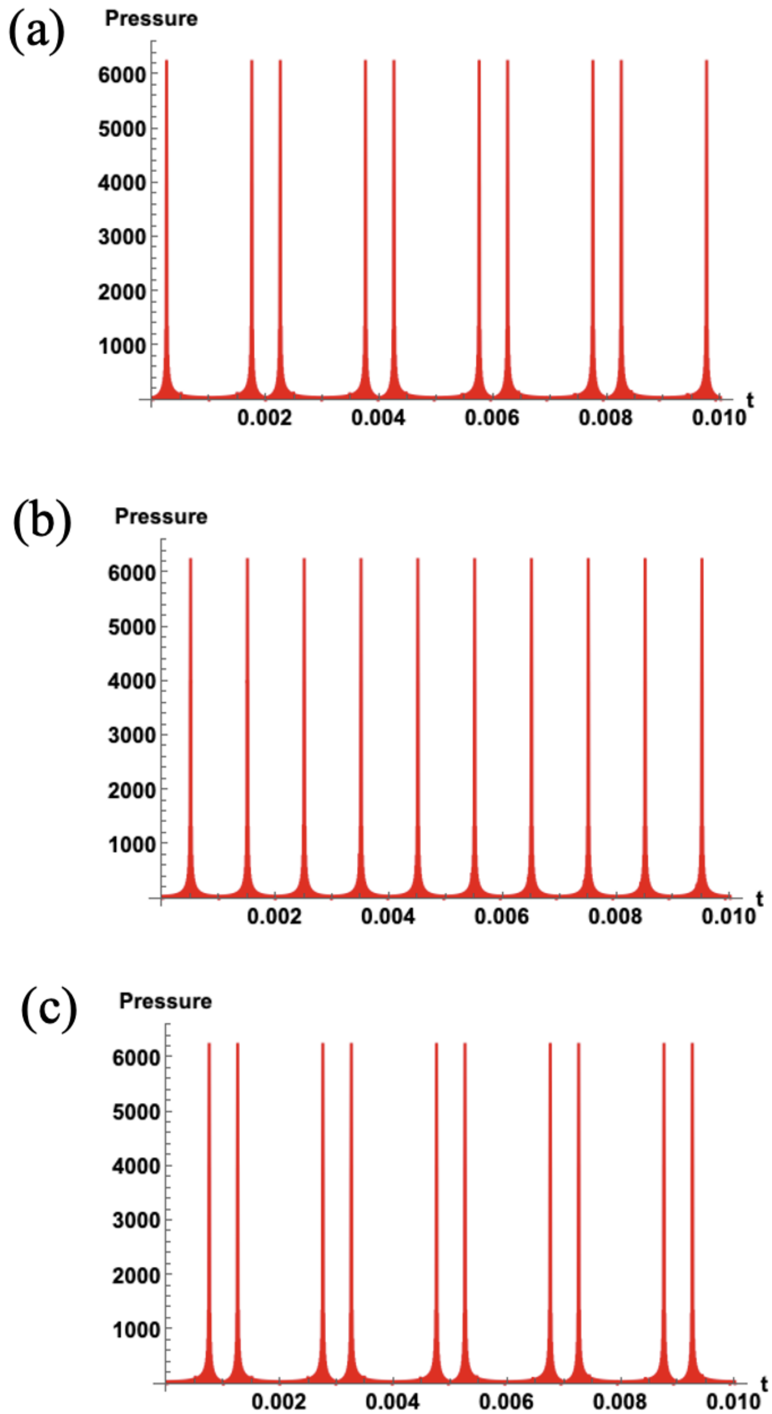

Figure 2.12: Evaluation of the time domain pressure for single delta pulse in a one-dimensional resonator in longer time interval (0, 0.01 s). The parameters taken are (a) $z = \frac{L}{4}$, (b) $z = \frac{L}{2}$, (c) $z = \frac{3L}{4}$, $c = 100$ m/s, $L = 0.1$ m, $\beta = 1$, $C_p = 1$, $I = 1$ and $M = 200$.

of the resonator to the left.

Fourier transformation of Eq. 2.41 followed by integration of the source term by parts gives a Helmholtz equation for the frequency domain pressure $\tilde{p}$ as

$$\left(\frac{d^2}{dz^2} + \frac{\omega^2}{c^2}\right)\tilde{p} = -\frac{i\omega\beta I}{C_p c}\int_{-\infty}^{\infty}\sum_{n=0}\delta(t - t_n)e^{-i\omega t}dt, \tag{2.53}$$

where $t_n = \frac{nL+z}{c}$ for even n and $t_n = \frac{(n+1)L-z}{c}$ for odd n.

The Green's function for the resonator is given as

$$G(z, z') = \frac{2}{L}\sum_m \frac{\cos k_m z \cos k_m z'}{k^2 - k_m^2}, \tag{2.54}$$

where $k = \frac{\omega}{c}$ and $k_m = \frac{m\pi}{L}$. Following an integration of Eq. 2.53 over the Green's function, the frequency domain pressure can be found as solution to Eq. 2.55 and Eq. 2.56.

For even n, we have,

$$\left(\frac{d^2}{dz^2} + \frac{\omega^2}{c^2}\right)\tilde{p} = -\frac{i\omega\beta I}{C_p c}e^{-i\frac{n\omega L}{c}}K_E. \tag{2.55}$$

For odd n, we have,

$$\left(\frac{d^2}{dz^2} + \frac{\omega^2}{c^2}\right)\tilde{p} = -\frac{i\omega\beta I}{C_p c}e^{-i\frac{(n+1)\omega L}{c}}K_O. \tag{2.56}$$

where $K_E = \int_0^L \cos k_m z' e^{-i\omega z'/c}dz'$ and $K_O = K_E^*$. Evaluation of the integral K_E gives,

$$K_E = -\frac{i\omega}{c\left(\frac{\omega^2}{c^2} - k_m^2\right)}\left(1 - re^{-i\omega L/c}\right), \tag{2.57}$$

where $r = (-1)^m$. The frequency domain photoacoustic pressure is thus,

For even n, we have,

$$\tilde{p} = -\frac{\omega^2 \beta I}{C_p c^2 L} \sum_{n,m} \frac{\cos k_m z}{\left(\frac{\omega^2}{c^2} - k_m^2\right)^2} e^{-in\omega L/c} \left(1 - r e^{-i\omega L/c}\right), \tag{2.58}$$

For odd n, we have,

$$\tilde{p} = \frac{\omega^2 \beta I}{C_p c^2 L} \sum_{n,m} \frac{\cos k_m z}{\left(\frac{\omega^2}{c^2} - k_m^2\right)^2} e^{-i(n+1)\omega L/c} \left(1 - r e^{i\omega L/c}\right). \tag{2.59}$$

Inverse Fourier transformation of Eq. 2.58 and Eq. 2.59 can be obtained using Mathematica, which gives,

$$p = -\frac{\sqrt{\pi}\beta I c}{2\sqrt{2} L C_p} \sum_{n,m} \frac{\cos k_m z}{k_m} \Theta(t - nL/c)(-1)^{n+1} \bar{p}, \tag{2.60}$$

where Θ is the Heaviside function and $\bar{p}$ in Eq. 2.60 is defined as,

$$\bar{p} = ck_m r(a-b+t)\cos\left(ck_m(a-b+t)\right) - ck_m(a+t)\cos\left(ck_m(a+t)\right) - \sin\left(ck_m(a+t)\right) + r\sin\left(ck_m(a-b+t)\right), \tag{2.61}$$

where a and b are defined as: for even n: $a = nL/c$ and $b = -L/c$ and for odd n: $a = (n+1)L/c$ and $b = L/c$. The summation in Eq. 2.60 over n refers the number of sweeps of the optical beam, begins at 0, and the summation over m starts at 1, and in principle extends to infinity, but which can be evaluated at a finite number.

Figure 2.13 shows the result of evaluation of Eq. 2.60 for a resonator with a transit time of 1 ms with the pressure recorded at the midpoint of the resonator. Evaluation of Eq. 2.60 for small values of m shows the effects of partial reinforcement and cancellation of the individual contributions to the overall wave amplitude.

It's clear from inspection of Eq. 2.60 that the solution is a summation over

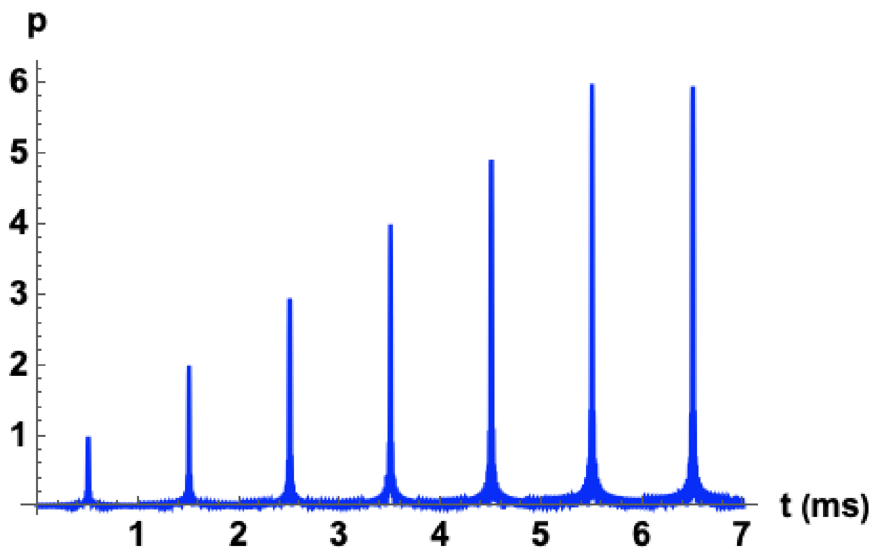

Figure 2.13: Magnitude of the photoacoustic pressure p versus time in milliseconds from Eq. 2.60 evaluated at midpoint of the resonator for $n = 5$, $m = 100$, $L = 0.1m$ and $c = 100m/s$.

numerous wavelets and the peaks in pressure are a result of interference of waves as governed by the Green's function. Given that the form of heating function is a summation of delta functions and that the resulting pressure spikes are sharp, evaluation of Eq. 2.60 at the end points of the resonator results in an ambiguity in the pressure amplitude.

It can be seen that the amplitude of the pressure increases linearly with the number of sweeps across the resonator. This addition is reminiscent of pulsed excitation of a conventional resonator when the time between pulses corresponds to a resonance of the photoacoustic cell. Such pulse addition has been used to advantage in Ref. [93] where a cylindrical resonator containing infrared absorbing gas was excited by a pulsed laser.

Chapter 3

Detection of photoacoustic waves by optical deflection

> “ Give me a lever long enough and a fulcrum on which to place it, and I shall move the world. ”
>
> – Archimedes

Recording of the time profile of photoacoustic waves in fluids [3, 94] has been the subject of keen interest over the past few decades as a result of the unique acoustic waves that can be generated by directing light into absorbing media [80,95–99]. While photoacoustic waves in liquids have been recorded using transducers based on solid transducers such as PZT (lead zirconate titanate), $LiNbO_3$ (lithium niobate) and polyvinylidene (PVDF), both PZT and $LiNbO_3$, the most commonly used ultrasonic transducers, owing to their large acoustic impedances relative to those of virtually every fluid, yield signals that suffer from uneven frequency response and distortion as a result of ringing. Transducers based on PVDF, which has an acoustic impedance much closer to that of water, offer large bandwidths and low signal distortion but suffer from a significantly lower sensitivity than found with conventional solid piezoelectric transducers. Optical recording of photoacoustic waves based on beam deflection has been reported where beam deflection of a low power continuous wave laser is recorded using a photodetector with a small active area placed off-center from the probe beam, or, alternately, where the deflection is recorded with a split photodiode [100,101]. In so far as the use of optical methods for photoacoustic imaging, the use of interferometric methods has been applied with impressive results [43, 50, 102, 103].

3.1 Conventional ways

Photoacoustic imaging has shown great promise in bioimaging owing to its unique combination of strong optical contrast with acoustic propagation depth around a few centimeters. The conventional way for recording the emitted acoustic waves initiated by pulsed laser to date is to use an array of pressure transducers [50,104,105]. Different setups of the ultrasound transducers have been presented in Ref. [59]. Some research groups use a frequency encoded, continuous laser beam to generate photoacoustic waves to be detected by conventional piezoelectric transducers [106]. Fabry-Perot interferometer has been used to sense the pressure field generated by a scanning probe laser beam across the interferometer surface [102]. A U-shaped array of fiber Fabry-Perot interferometers has been used to record the integrated pressure over the length of the fibers [43]. The detailed review for photoacoustic imaging can be found in Ref. [50] and Ref. [72].

As mentioned above, pressure transducers, which are critical components in photoacoustic imaging systems, are far from ideal. Thin film transducers such as PVDF have quite flat frequency response which is great for high resolution imaging but suffer from low sensitivity issues. The crystals such as $LiNbO_3$ and solid transducers such as

PZT have higher sensitivity than PVDF but suffer from significantly distortion of the signal. The distortion comes from the mechanical resonances of the solid transductors that can significantly distort the measured photoacoustic pressure waveform.

The sensitivity of piezoelectric transducers is typically fixed [107] depending on the piezoelectric voltage coefficient (pC/Pa) and the noise in the preamplifier. On the other hand, optical recording of acoustic waves using beam deflection has a huge bandwidth advantage which is mainly limited by the response time of the optical detector and the electronics to read the voltage from a diode detector. Most commercially available optical sensors would have response times on the order of 10 ns. Moreover, it would be possible to use a design that reflects the optical beam back and forth in the sound field region so that the signal amplitude can be significantly enhanced.

3.2 Spherical sources

Photoacoustic waves can be detected by recording optical beam deflection as a result of density gradients inherent in the waves. Beam deflection can be recorded from a single laser beam placed at a distance from the source where data are generated as a function of time, or by recording beam deflections at a single time as the position of the probe beam is varied. For either case, the deflection signal is shown to be described by an Abel transform of the pressure gradient. Here, the inversion of beam deflection data from photoacoustic sources with symmetry in one, two, and three dimensions are investigated. An iterative method based on total variation regularization and a regression procedure based on Lasso regularization are shown to result in accurate reproductions of the theoretical expressions that describe photoacoustic waves from simple sources.

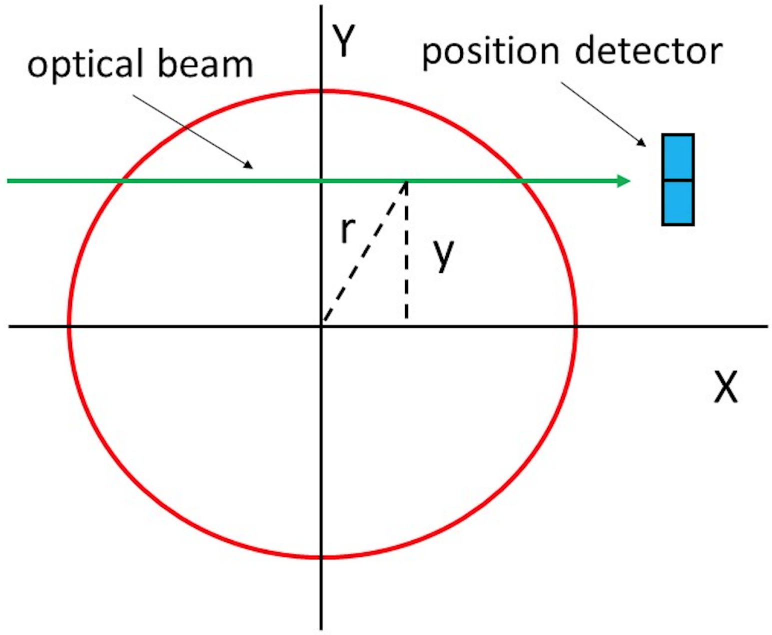

Figure 3.1: Schematic of the experimental arrangement for recording optical beam deflection from the pressure gradient in a photoacoustic wave emanating from the origin of coordinates. Deflection signals can be recorded either by recording the deflection at a fixed time as y is moved over a range of distances from the x axis, or by fixing the position at a position y_0 and recording beam deflections in time. For a spherical source it is assumed that the probe beam is located in the $z = 0$ plane.

Consider a photoacoustic wave emanating from a spherical source located at the origin where the gradient of the pressure is recorded by an optical beam located at a distance y_0 propagating in the positive x direction as shown in Fig. 3.1. At any point along the x axis the deflection angle of the beam [100, 108, 109] is proportional to $\partial p(r,t)/\partial y$ so that the deflection angle in traversing a distance through the entire acoustic wave d can be written as an integral of either the density gradient, or, as formulated here, the pressure gradient over the x coordinate

$$d(t, y) = \frac{n_0 - 1}{2n_0\rho_0 c^2} \int \frac{\partial p(r,t)}{\partial y} dx, \tag{3.1}$$

where n_0 is the ambient density of the medium, ρ_0 is the density, and c is the sound speed. Given that $r^2 = x^2 + y^2$ it follows that the integral in Eq. 3.1 can be written for a beam traversing the entirety of the acoustic field parallel to the x axis as

$$d(t, y) = \frac{n_0 - 1}{n_0 \rho_0 c^2} \int_y^R \left[\frac{y}{r} \frac{\partial p(r, t)}{\partial r} \right] \frac{r}{\sqrt{r^2 - y^2}} dr, \tag{3.2}$$

where R can be taken to describe the farthest spatial extent of the acoustic wave for a given time t, or can be taken as infinity. It can be seen that Eq. 3.2 is the form of an Abel transform [110], the inversion of which has been the subject of substantial interest as it appears in data reduction problems in a number of fields [111–116]. Of note for the photoacoustic imaging inversion problem with integrating line detectors is the use of back-projection algorithms and 2-D inverse Radon transform to determine the original 3D pressure distribution [45].

Here, the problem of determining the acoustic pressure field from a photoacoustic source with spherical symmetry from a recording of optical beam deflection data is investigated using the inverse Abel transform. In Section 3.2.1, the problem of determining the photoacoustic profile recorded by optical beam deflection data recorded in time with the optical beam located at a fixed position is discussed. In Section 3.2.2, a similar problem is presented, but with the probe optical beam positioned at a various distances from the photoacoustic source but with the time from initiating the photoacoustic effect fixed.

3.2.1 Time dependent deflection data from a fixed optical beam

For an optical beam located at a fixed distance y_0 from the x axis that probes the acoustic wave emanating from the origin, is possible to write Eq. 3.2 as

$$\hat{d}_{\hat{y}_0}(\hat{t}) = 2\int_{\hat{y}_0}^{\hat{R}} \left[\frac{\hat{y}_0}{\hat{r}}\frac{\partial \hat{p}(\hat{r},\hat{t})}{\partial \hat{r}}\right] d\sqrt{\hat{r}^2 - \hat{y}_0^2}, \tag{3.3}$$

where the following dimensionless variables have been defined: $\hat{p} = p/\rho_0 c^2$, $\hat{d} = d/a$, $\hat{y}_0 = y_0/a$, $\hat{r} = r/a$, and $\hat{t} = ct/a$, where a is a length parameter, and, for brevity, the factor $(n_0 - 1)/2n_0$ has been set to unity. The quantity in brackets in Eq. 3.3 hereinafter will be referred to as the "source function" and denoted $\hat{S}(\hat{t}, \hat{r}, \hat{y}_0)$. For purposes of numerical evaluation, Eq. 3.3 can be written in matrix form as

$$\hat{d}_k = 2\sum_i \hat{B}_{k,i}\hat{q}_i, \tag{3.4}$$

where $\hat{B}_{k,i}$ and $\hat{q}_i$ are defined as

$$\begin{aligned} \hat{q}_i &= \sqrt{\hat{r}_i^2 - \hat{y}_0^2} - \sqrt{\hat{r}_{i-1}^2 - \hat{y}_0^2}, \\ \hat{B}_{k,i} &= \frac{\hat{y}_0}{\hat{r}}\frac{\partial[\hat{f}(\hat{t} - \hat{r})/\hat{r}]}{\partial \hat{r}}\bigg|_{\hat{r}=\hat{r}_i;\ \hat{t}=\hat{t}_k}. \end{aligned}$$

The index k is associated with the time variable, that is, $\hat{d}_k$, represents k values of beam deflections and the summation over i gives the integration over the source function in Eq. 3.3, whose matrix representation is $\hat{B}_{k,i}$.

An outgoing photoacoustic wave with spherical symmetry [87, 117] excited by a short optical pulse (one where the laser pulse width is significantly smaller than the transit time of sound across the irradiated object) can, in general, can be taken to be of the form $p(r,t) = f(t-(r-a)/c)/r$, represented by $\hat{f}$ in Eq. 3.4, where a is a length parameter for the irradiated object. For example, a would be the radius of the sphere for a spherical droplet [80, 81] discussed above, and the retarded time τ from the perimeter of the sphere would be $t-(r-a)/c$ or $\hat{t}-(\hat{r}-1)$ in dimensionless units. Since probing of the photoacoustic wave is assumed to be at a distance a or greater from the origin, it is convenient from the point of view of notation to label the various values of $\hat{f}$ as $\hat{f}_{k-i}$ so that f_0 corresponds to the first value of the retarded time outside the object. Stated alternately, the shift that corresponds to the removal of the length parameter in the elements of $\hat{\mathbf{B}}$ is the equivalent to starting the summation so that each value of $\hat{q}_i$ multiplies the element $B_{m,i}$ (for any m) corresponding to the point $\hat{r}_i$ rather than $\hat{r}_{i-1}$, which removes the factor of unity in the argument of $\hat{f}$ in Eq. 3.4.

For short pulse excitation the retarded time must be greater than zero; thus values of $\hat{f}_{k-i}$ in Eq. 3.4 must be zero for any negative value $k-i$. This constraint demands the off diagonal elements to the right of the diagonal in $\hat{\mathbf{B}}$ be zero. A second requirement, which eliminates imaginary quantities in Eq. 3.4, is that $\hat{r}_i^2$ be greater than $\hat{y}_0^2$, a condition that results in zeroes in $\hat{q}$. The desired solution to the matrix equation for the photoacoustic problem is a list of values of $\hat{B}_{k,i}$ which represents the numerical approximation to the source function in Eq. 3.3 as a function of retarded time. Given the two conditions on the elements of $\hat{\mathbf{B}}$, Eq. 3.4 can be written

$$\begin{bmatrix} \hat{d}_1 \\ \hat{d}_2 \\ \hat{d}_3 \\ \hat{d}_4 \\ \vdots \end{bmatrix} = \begin{bmatrix} \tilde{f}_0 & 0 & 0 & 0 & 0 \\ \tilde{f}_1 & \tilde{f}_0 & 0 & 0 & 0 \\ \tilde{f}_2 & \tilde{f}_1 & \tilde{f}_0 & 0 & 0 \\ \tilde{f}_3 & \tilde{f}_2 & \tilde{f}_1 & \tilde{f}_0 & 0 \\ \vdots & \vdots & \vdots & \vdots & \vdots \end{bmatrix} \begin{bmatrix} \tilde{q}_1 \\ \tilde{q}_2 \\ \tilde{q}_3 \\ \tilde{q}_4 \\ \vdots \end{bmatrix}, \tag{3.5}$$

where $\tilde{q}_i = 2\hat{q}_i$. Equation 3.5 can be solved by numerical methods; however, the same matrix equation can be rewritten as

$$\begin{bmatrix} \hat{d}_1 \\ \hat{d}_2 \\ \hat{d}_3 \\ \hat{d}_4 \\ \vdots \end{bmatrix} = \begin{bmatrix} \tilde{q}_1 & 0 & 0 & 0 & 0 \\ \tilde{q}_2 & \tilde{q}_1 & 0 & 0 & 0 \\ \tilde{q}_3 & \tilde{q}_2 & \tilde{q}_1 & 0 & 0 \\ \tilde{q}_4 & \tilde{q}_3 & \tilde{q}_2 & \tilde{q}_1 & 0 \\ \vdots & \vdots & \vdots & \vdots & \vdots \end{bmatrix} \begin{bmatrix} \tilde{f}_0 \\ \tilde{f}_1 \\ \tilde{f}_2 \\ \tilde{f}_3 \\ \vdots \end{bmatrix}, \tag{3.6}$$

which can be written in the form of a conventional minimization problem for the vector $\tilde{f}$,

$$\tilde{f} = \arg\min_{\tilde{f}} ||\hat{d} - \tilde{\mathbf{Q}}\tilde{f}||^2. \tag{3.7}$$

The least square solution to the minimization problem is

$$\hat{\mathbf{B}} = (\tilde{\mathbf{Q}}^T\tilde{\mathbf{Q}})^{-1}\tilde{\mathbf{Q}}^T\hat{d}. \tag{3.8}$$

however, as is well-known, the use of Eq. 3.8 suffers from instabilities when noise is present in d and from the effects of ill-conditioning. The use of Lasso (least absolute shrinkage and selection operator) regularization resulted in accurate solution of the minimization in Eq. 3.7 as is shown below in Fig. 3.2.

The iterative, total variational regularization given by Ref. [111,112] was found to be accurate and straightforward, as well, and is outlined in the remaining part. The vector $\tilde{f}_\nu$ for each iteration ν is determined through

$$\tilde{f}_{\nu+1} = \tilde{f}_\nu - [\tilde{\mathbf{Q}}^T\tilde{\mathbf{Q}} + \alpha\hat{\mathbf{L}}(\tilde{f}_\nu)]^{-1}[\tilde{\mathbf{Q}}^T(\tilde{\mathbf{Q}}\tilde{f}_\nu - \hat{d}) + \alpha\hat{\mathbf{L}}(\tilde{f}_\nu)\tilde{f}_\nu], \tag{3.9}$$

where the matrix $\hat{\mathbf{L}}$ and the diffusivity function $\hat{\phi}$ are given by

$$\begin{aligned}\hat{\mathbf{L}}(\tilde{f}) &= \hat{\phi}\hat{\mathbf{D}} + \hat{r}\hat{\mathbf{D}} \cdot \phi\hat{\mathbf{D}}, \\ \hat{\phi} &= \frac{1}{\sqrt{|\hat{\mathbf{D}}\tilde{f}_\nu|^2 + \beta^2}},\end{aligned}$$

with $\hat{r}$ a vector consisting of the dimensionless values of the coordinate. The discrete gradient operator matrix $\hat{\mathbf{D}}$ is constructed as a simple forward difference matrix, which for the case $\hat{R} = 2$ and the number of points $N = 50$, for example, is given [112] by

$$\hat{\mathbf{D}} = \begin{bmatrix} 25 & 0 & 0 & 0 & 0 \\ -25 & 25 & 0 & 0 & 0 \\ 0 & -25 & 25 & 0 & 0 \\ 0 & 0 & -25 & 25 & 0 \\ \vdots & \vdots & \vdots & \vdots & \vdots \end{bmatrix}, \tag{3.10}$$

where each of the nonzero entries are given by $N/\hat{R}$.

Consider the photoacoustic effect from an optically thin, spherical droplet immersed in a fluid with the identical sound speed and density. If the pulse width of the exciting laser is shorter than the transit time of sound across the sphere, the emitted photoacoustic pressure wave is given by Refs. [81] and [80],

$$p(\hat{\tau}) = \frac{\alpha\beta E_0 c^2}{2C_P\hat{r}}(1 - \hat{\tau})\tilde{\Theta}_{0,2}(\hat{\tau}), \tag{3.11}$$

where α is the optical absorption coefficient of the fluid in the sphere, $\hat{\tau}$ is the retarded time from the sphere given by $\hat{\tau} = (c/a)[t - (r - a)/c]$, E_0 is the fluence of the laser pulse, β is the thermal expansion coefficient, a is the radius of the droplet (the length parameter noted above), and $\tilde{\Theta}_{0,2}(\hat{\tau})$ is a square wave function that begins and ends

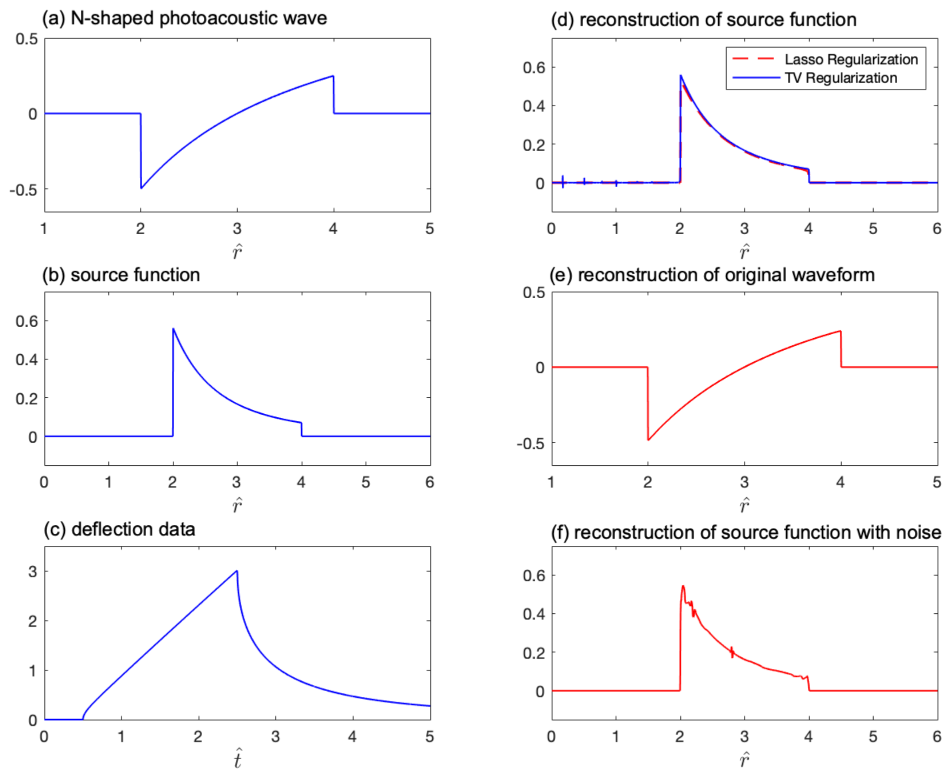

Figure 3.2: Plots of (a) an N-shaped photoacoustic wave from Eq. 3.11 versus $\hat{r}$ at $\hat{t} = 3$, (b) the corresponding source function, (c) the deflection signal vs. $\hat{t}$ for $y_0 = 1.5$, (d) the reconstructed source function vs. $\hat{r}$ from total variational reconstruction (solid line) and Lasso regularization (dashed line), (e) integration of the source function to give the original photoacoustic waveform, and (f) reconstructed source function where noise with an amplitude of 5% of the N-wave peak amplitude was added. All ordinates and abscissas are in dimensionless units.

at values of $\hat{\tau}$ equals 0 and 2, respectively. The photoacoustic pressure described by Eq. 3.11, when plotted as a function of the retarded time, is an N-shaped wave.

To test the numerical reconstruction, simulated data were made up by forming the source function from the functional form of photoacoustic waves. A table of values of $\hat{d}_i$ representing deflection data taken at different times at a single position $\hat{y}_0$ was found by numerical integration of Eq. 3.3. It was found that inversion of the matrix in Eq. 3.8 was difficult as $\tilde{\mathbf{Q}}$ was invariably ill-conditioned. This difficulty was ameliorated by using Lasso regularization [118, 119], available in Matlab software, or total variation regularization [111, 112]. Figure 3.2 shows plots of the original N-shaped acoustic wave as a function of coordinate, the source function, the calculated deflection data, the reconstruction of the source function and its integration to recover the N-wave. The values of the parameters used in the calculation were $\hat{y}_0 = 1.5$, $\alpha = 0.5$, and $\beta = 10^{-5}$. Convergence to the final values of the source function required on the order of 20 iterations of Eq. 3.9. The method based on the minimization indicated in Eq. 3.7 using Lasso regularization [118, 119] was explored as well. The results using both methods, which required only a few seconds of computer time, can be seen in Fig. 3.2 (d) and (e). Although a detailed study of the sparsity level and the reconstruction error is out of the scope of this study, the properties of the Lasso estimator have been treated in the mathematical literature [120–122]. Based on our empirical evaluations with both high and low sparsity levels it is apparent that the reconstruction method based on Lasso regularization performs adequately for the present photoacoustic problem.

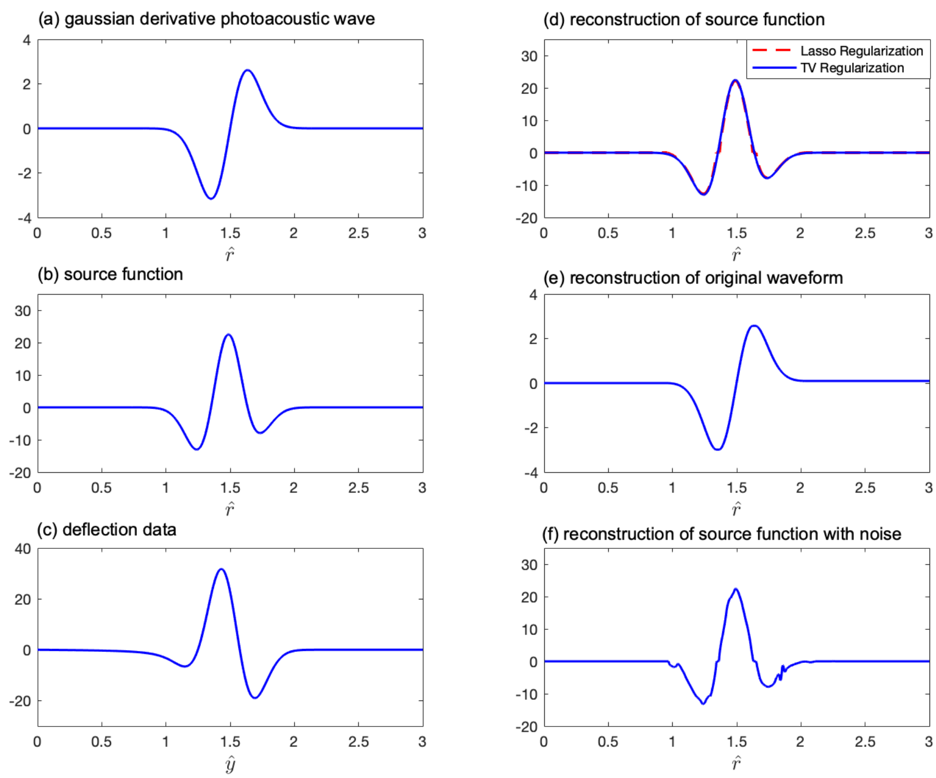

Figure 3.3: Waveforms for (a) a Gaussian photoacoustic pressure wave from Eq. 3.16 vs. coordinate, (b) its source function vs. coordinate, (c) calculated beam deflection vs. displacement from the x-axis, (d) reconstructed source function, (e) original waveform from integration of the reconstructed source, and (f) reconstructed source function where noise with an amplitude of 5% of the initial peak amplitude was added. All waveforms were calculated with $\hat{t} = 1.5$ and $\hat{\Theta} = 0.2$. The ordinates and abscissas are in dimensionless units.

3.2.2 Deflection data from a movable optical beam at a fixed time

One experimental realization of beam deflection for determining photoacoustic wave properties uses a laser beam that is translated parallel to the x-axis to record the deflection at a series of positions y at a fixed time t_0 after a pulsed laser has generated the photoacoustic wave. The mathematics for the inversion is similar to that given above; but in this case solution to

$$\hat{d}_{\hat{t}_0}(\hat{y}) = 2\int_{\hat{y}_0}^{\hat{R}} \Big[\frac{\hat{y}}{\hat{r}}\frac{\partial \hat{p}(\hat{r},\hat{t}_0)}{\partial \hat{r}}\Big] d\sqrt{\hat{r}^2-\hat{y}^2} \tag{3.12}$$

is desired. If the distances from the origin are taken to be the same as those for the radial coordinates to be summed over, i.e. $\hat{r}_i = \hat{y}_i$ $(i = 1, ..., N)$ to yield square matrices, then the matrix equation corresponding to Eq. (3.12) becomes

$$\hat{d}_j = \sum_i \hat{\rho}_i \hat{P}_{i,j}, \tag{3.13}$$

where

$$\begin{aligned}
\hat{P}_{i,j} &= 2\Big[\sqrt{\hat{r}_i^2-\hat{y}_j^2} - \sqrt{\hat{r}_{i-1}^2-\hat{y}_j^2}\Big], \\
\hat{\rho}_i &= \frac{\hat{y}}{\hat{r}}\frac{\partial[f(\hat{r},\hat{t}_0)/\hat{r}]}{\partial \hat{r}}\Big|_{\hat{r}=\hat{r}_i}.
\end{aligned}$$

For computational purposes the values of $\hat{r}_j$ in $\hat{P}_{i,j}$ can be taken as $\hat{y}_j$. The entries for the vector $\hat{\rho}$ are the N values of the source function ranging from 0 to $\hat{R}$. Since only real values of $\hat{\mathbf{P}}$ are acceptable, all matrix elements to the right of the diagonal in $\hat{\mathbf{P}}$ must be zero. Rearrangement of Eq. 3.13 results in the matrix equation for the transpose of $\hat{\mathbf{P}}$

$$\hat{d}_j = \sum_i \hat{P}^T_{j,i}\hat{\rho}_i, \tag{3.14}$$

whose solution requires determination of optimized values of $\hat{\rho}$ according to

$$\hat{\rho} = \arg\min_{\hat{\rho}} ||\hat{d} - \hat{\mathbf{P}}^T\hat{\rho}||^2, \tag{3.15}$$

which can be carried out using Lasso or total variation regularization. The matrix $\hat{\mathbf{P}}$, owing to the choice of taking $\hat{r}_i = \hat{y}_i$, contains numerous zeroes. However both Lasso or total variation regularization yields reconstructed source functions that have excellent matches to the original photoacoustic waves as shown in Fig. 3.3.

An example, the use of the two methods for inversion of deflection signals generated by the photoacoustic effect from a source with symmetry in three dimensions where the laser pulse width is large compared with the transit time across the sphere was investigated. The photoacoustic wave [7] resulting from an optical pulse with a functional form $S(t/\Theta)$ where Θ is a pulse width parameter is

$$p(\hat{\tau}_l) = \frac{\alpha\beta E_0 c^2}{2C_P\hat{r}\ \hat{\Theta}_l}\frac{d}{d\tau_l}S(\hat{\tau}_l), \tag{3.16}$$

where $\hat{\Theta} = c\Theta/a$, $\hat{\tau}_l = (c/a)(t - r/a)$, and $\hat{r} = r/a$, where a is a length parameter associated with the absorber. For a Gaussian laser pulse in time the source function for Eq. 3.12 becomes

$$\hat{S}(\hat{t}, \hat{r}, \hat{y}) = \left(\frac{2\hat{y}}{\hat{r}}\right)\left[\frac{\hat{t}\hat{\Theta}^2 - 2\hat{r}(\hat{t} - \hat{r})^2}{\hat{r}^2\hat{\Theta}^4}\right]e^{-(\hat{t}-\hat{r})^2/\hat{\Theta}^2}, \tag{3.17}$$

which is plotted in Fig. 3.3. The reconstruction of the source function is identical to that given in Section 3.2.1 and was carried out using both Lasso and total variational regularization, the results of which are plotted in Fig. 3.3.

Investigation of the accuracy of the fit of the reconstructed relative to the simulated source function for the solution given in Section 3.2.1 was carried out for a Gaussian source, i.e. where the quantity in brackets in Eq. 3.3 was a Gaussian. The result for the best fits showed a mean squared error for the Lasso regularization to be 1.9×10^{-4}, while that for the total variation regularization (with 250 iterations to obtain the best fit) was 1.4×10^{-4}. The addition of white noise with a root mean square noise amplitude taken to be 5% of the Gaussian function at its peak resulted in values for the error of 2.8×10^{-4} and 4.2×10^{-4} for the Lasso and total variation regularization methods respectively.

3.2.3 Discussion for photoacoustic waves with symmetry in one, two and three dimensions

The present calculation starting with Eq. 3.1 considers only an optical ray. For the case of a finite optical beam, for instance, one with a Gaussian spatial profile, Eq. 3.1 would have to be convoluted with the Gaussian beam profile. The inversion of the convolution appears to be a problem worthy of investigation, but is beyond the scope of the present investigation. In so far as experiments are concerned, application of the results given here for either fixed or movable beams requires that the pressure gradient of the acoustic wave over the spatial extent of the probe optical beam be small, thus eliminating sources that produce, for instance, shock waves.

In addition to solutions to the wave equation for the photoacoustic effect, other functions such as square waves, short pulse waves, triangle waves, Gaussian waves, and Gaussian derivative waves with varying pulse widths were investigated to determine the capability of the Lasso and total variation regularization methods for accurate

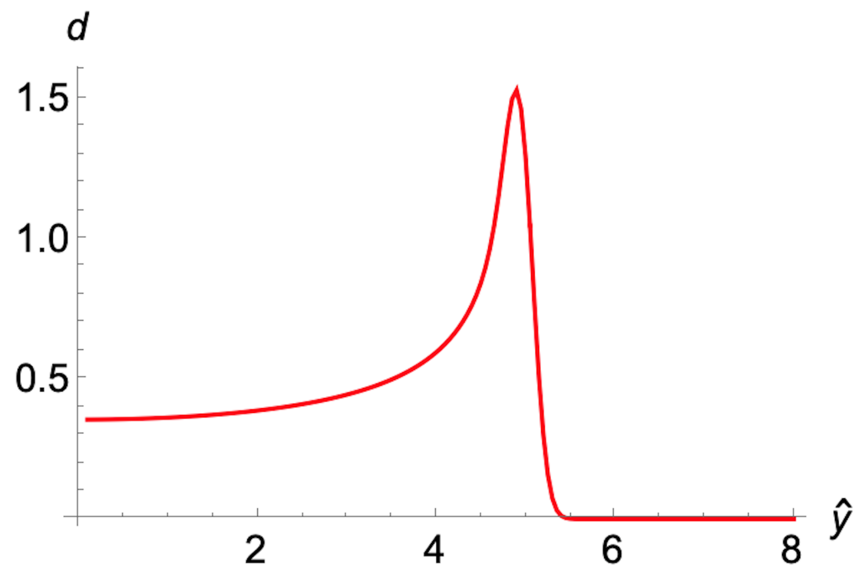

Figure 3.4: Abel transform d of a Gaussian wave in dimensionless units vs. coordinate $\hat{y}$, computed with $\hat{\Theta} = 0.2$

reconstructions. The inversions of the Abel transform were equally successful for all of these waveforms as in the two cases of photoacoustic beam deflection signals from the Gaussian derivative and N-shaped waves discussed above. A plot of the results of a numerical integration of Eq. 3.12 with a simple Gaussian for the source function is shown in Fig. 3.4. It is noteworthy that the transform does not vanish as the time or coordinate approaches zero as is the case with light beam deflection signals. The relative ease of performing the inversions of Gaussian sources suggests the Lasso and total variation regularization methods to Abel inversions of photoionization data.

Note that it is possible to do experiments where the source has symmetry in one as well as two dimensions. For the former, where the pressure gradient is along the y-axis, the deflection is simply proportional to $z\partial p(y,t)/\partial y$, where z is the path length of the optical beam in the medium. Determination of the pressure profile would thus require only integration of the reconstructed deflection data. In two dimensions the geometry for beam deflection would be with the laser beam propagating along what would be the z-axis in Fig. 3.1 with the photoacoustic wave emanating radially outwards. The deflection angle can easily be shown to be exactly that given by Eq. 3.2 and the inversion mathematics would be identical that given in Section 3.2.1 and 3.2.2 .

In so far as experiments are concerned, the recording of beam deflections in time with a single laser beam to determine photoacoustic waveforms appears to be a straightforward method of recording data since contemporary oscilloscopes can digitize signals with both high speed and high resolution. Relative to the fixed position optical arrangement, the experiment where data are collected at one time by sequentially moving the light beam along the y axis requires a more complicated movable optical arrangement. Thus, the photoacoustic experiment described in Section 3.2.1 should be of wider applicability that given in Section 3.2.2. On the other hand, the widespread use of inverse Abel transformation in X-ray tomography, absorption in plasmas and jet engine plumes, and photoionization velocity mapping, suggest that the movable probe geometry discussed in Section 3.2.2 may have the widest application to inverse Abel reconstruction, in general.

3.3 Arbitrary sources: all-optical photoacoustic tomography

Section 3.2 focuses on the methods to reconstruct the photoacoustic waves with symmetry in one, two and three dimensions from the measured optical deflection data. The idea can be naturally extended to arbitrary sources to design a new imaging modality which can function as all-optical photoacoustic tomography. Here we propose a new experimental setup that utilizes the beam deflection of an array of laser

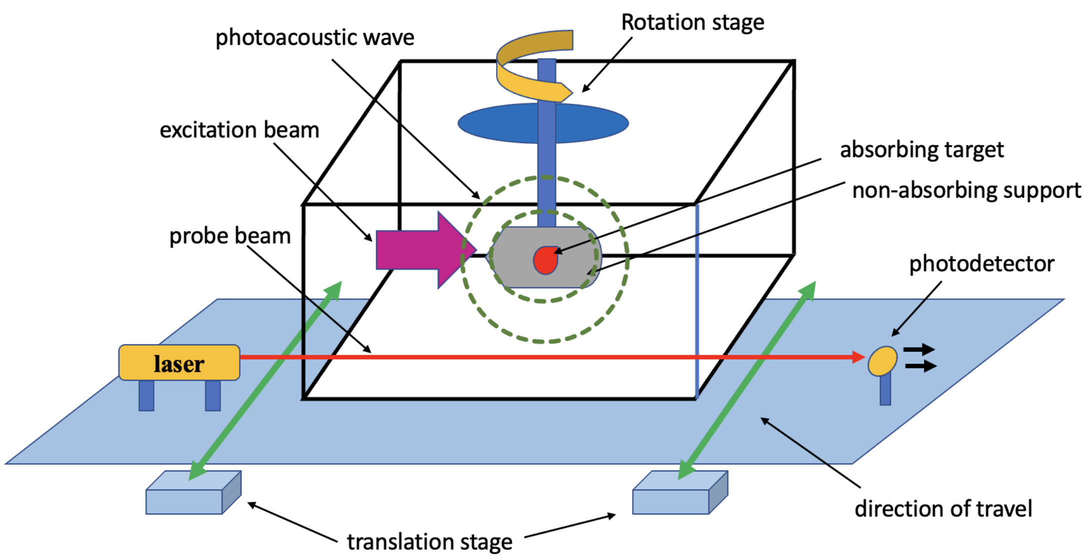

Figure 3.5: Schematic of photoacoustic tank with a single exciting laser beam, probe laser beam, and detector array. The probe laser and detector move simultaneously in recording data.

beams directed along a plane below the photoacoustic source with the recording the deflections of each of the beams with fast photodetectors whose outputs are digitized and fed into computer for signal processing and reconstruction.

Consider a photoacoustic source above the $z = 0$ plane, an array of probe beams on the $z = 0$ plane will traverse the acoustic field emitted by the photoacoustic source. The deflection angle θ_z in the positive z direction along the line d at an angle γ can be written as

$$\theta_z(d, \gamma, t) = \frac{n_0 - 1}{2n_0 c^2 \rho} \iint_{-\infty}^{\infty} \left. \frac{\partial p(r, t)}{\partial z} \right|_{z=0} \delta(x \cos\gamma + y \sin\gamma - d) dx dy, \tag{3.18}$$

where n_0 is the index of refraction, c is the sound speed and ρ is the density of the medium. The deflection angle $\theta_z(d, \gamma, t)$ in Eq. 3.18 describes a Radon transform of the pressure gradient along z direction at plane $z = 0$ from (x, y) to (d, γ). The imaging forward model can be formulated as follows,

$$\Theta_z = \frac{n_0 - 1}{2n_0c^2\rho} RAp_0, \tag{3.19}$$

where R is the Radon transform operator, A is the operator that maps the initial pressure field to the pressure gradient along the z direction at plane $z = 0$. The deflection data Θ_z can be written as a matrix of dimension $(N \times N_t, 1)$, A is a matrix of dimension $(N_x \times N_y \times N_t, N_x \times N_y \times N_z)$ and p_0 is a matrix of dimension $(N_x \times N_y \times N_z, 1)$ where N_t is the number of time grids, N_x, N_y and N_z is the number of space grids in the x, y and z directions and N is related with the Radon transform.

One way to reconstruct the initial pressure would be solving the following optimization problem,

$$\hat{p}_0 = \arg\min_{p_0 \geq 0} \frac{1}{2} \left\| \Theta_z - \frac{n_0 - 1}{2n_0c^2\rho} RAp_0 \right\|^2 + \lambda R(p_0), \tag{3.20}$$

where the first term is the data fidelity term which describes the discrepancy between the measured optical deflection signal with the signal predicted by the model and the second term is the regularization term which is often taken as the total variation regularization $R(p_0) = \|\nabla p_0\|_1$.

The operator A can be further written as $A = MP$ where M is derivative operator and P is the propagation operator that maps the initial pressure to the pressure at different time steps. The action of operator P and its adjoint P^* can be calculated using k-wave. The adjoint of derivative operator is just the negative of the operator itself under some regularity conditions which is due to the following reasoning using integration by parts,

$$\int g \frac{\partial}{\partial z} f = -\int f \frac{\partial g}{\partial z}. \tag{3.21}$$

In one possible setup as Fig. 3.5 shows, one might use some phantom with an absorbing dye suspended from a rotation stage mounted atop of the water-filled glass tank. A 1.06 μm Nd: YAG pulsed laser beam as the excitation beam and a He-Ne probe laser beam enters below and perpendicularly to the direction of the exciting laser. Both the probe laser and the detectors will be mounted on a translation stage that moves along the detector coordinate as the pulsed laser fires while the time dependence of the deflection signal is recorded. The angle γ is scanned from 0 to 180°. Although the proposed experiment here is slow due to the scanning of multiple angles, it can be carried out with single channel instrument to determine the best source, detector and optical train. The initial experiment would be very essential to determine the key parameters such as sensitivity, signal-to-noise ratio, linearity as well as dynamic range for the development of further imaging modalities.

It's possible to record deflections in more than one direction, for example, two directions with a two-dimensional array of light sources, a lens array and a CCD detector operating as an analog of s Shack-Hartman interferometer [123, 124], which might improve the signal-to-noise ratio and make data acquisition faster.

In summary, Section 3.3 discusses the proposal of all-optical photoacoustic tomography and potential experimental realizations that might result in a high resolution, strong contrast and superior signal-to-noise ratio in the reconstructed image. The advantages that this new imaging modality would bring compared with the conventional pressure recording remain unknown which would be worth future experimental efforts to explore.

Chapter 4

Solving inverse problems in optoacoustic tomography using machine learning

> “ An approximate answer to the right problem is worth a good deal more than an exact answer to an approximate problem. ”
>
> – John Wilder Tukey

Optoacoustic tomography, which combines strong optical contrast with high acoustic penetration depth, has shown great promise in bioimaging especially neuroimaging where the applications have spanned imaging of rat brain [125] to human brain [126]. Chapter 4 will discuss the challenges and possible approaches for solving inverse problems in optoacoustic tomography using machine learning.

4.1 Challenges that faces optoacoustic tomography

As in most medical and biophysical imaging modalities, challenges accompany the development of optoacoustic tomography. One critical issue, axiomatic to researchers in photoacoustic imaging, might be the incomplete measurements of the acoustic signals due to the finite bandwidth of the acoustic transducers as well as the limited-view detection setup. As mentioned in Chapter 3, the bandwidths of existing pressure transducers are often limited which constitutes an inherent limitation in measurement accuracy. In practice, the transducer response might be modeled as a Gaussian distributed around some central frequency.

Here a simple simulation has been conducted to demonstrate the bandwidth effect in photoacoustic imaging using k-wave. The computational grid is set to be 0.1 mm, the sound speed as 1500 m/s, the center frequency of the transducer as 2.5 MHz and the bandwidth of the transducer as 85%. The photoacoustic effect generated by a disk with initial pressure 50 Pa, centered at the origin with disk radius 1 mm has been simulated. The acoustic attenuation coefficient alpha of the medium is set to be 0.8 and the attenuation power of the medium is set to be 1.5. The sensors are placed at a radius of 5 mm around the origin with the number of sensors 100. As shown in Fig. 4.1, the original signal obtained from a perfect acoustic detector shows a clear N-shaped waveform while the signal obtained from a bandlimited detector shows a severe distortion of the pressure time series waveform. However, the two peaks (positive and negative peaks) for the bandlimited case coincide very well with the two peaks of the original N-shape waveforms for the perfect detector setup. The N-shape characteristic wave feature of photoacoustic excited spherical droplets is well verified by a list of theory and experiments as discussed in Chapter 2. Figure 4.2 shows

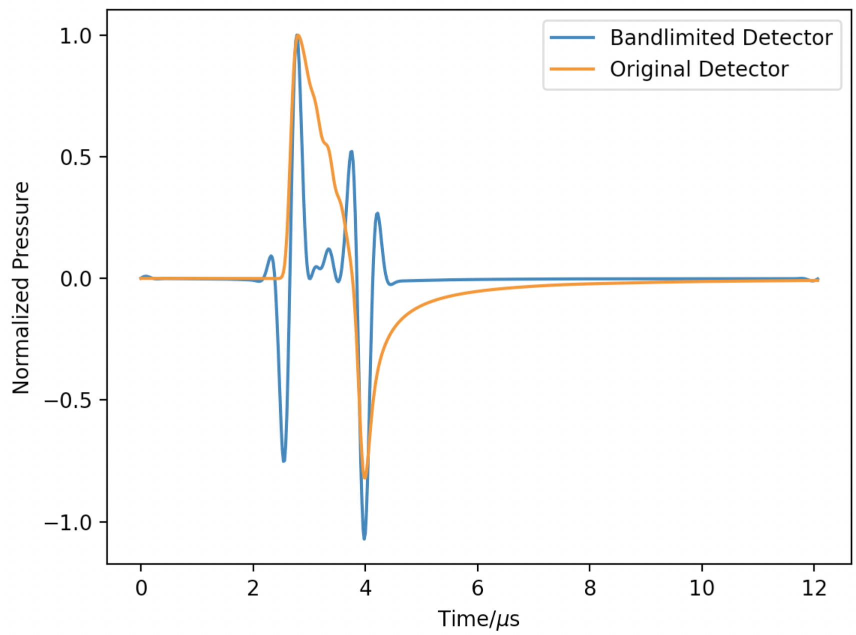

Figure 4.1: Plot of the simulated photoacoustic pressure at some detector position recorded by a perfect detector (orange) and by a bandwidth-limited detector (blue). The pressures are normalized by the corresponding maximum values.

the amplitude spectrum obtained by perfect detectors as well as that obtained by bandlimited detectors. The amplitude for the bandlimited detector decays compared with the original detector although they share some similarities including the major peaks. The size of the droplet roughly determines the time and frequency domain response, millimeter-sized droplets typically have a characteristic time scale on order of μs while the micron-sized droplets would have characteristic time scale of order nanoseconds.

Another challenge in optoacoustic tomography is undersampling which is often due to the limited view of sound field by the array of acoustic transducers. The widely used detection geometries may not satisfy the Shannon sampling criterion. In reality, the pressure transducers can only be placed in some detection planes or parts of the detection spheres. For example, the first functional photoacoustic imaging

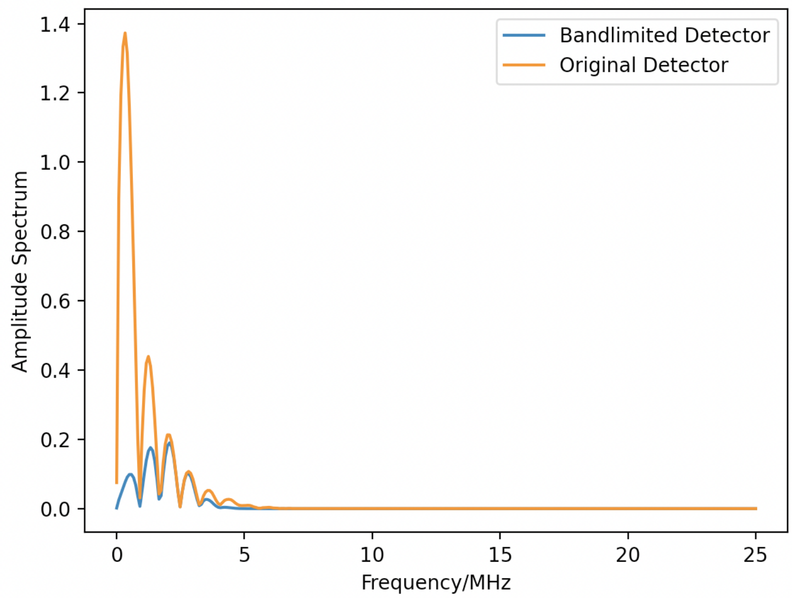

Figure 4.2: Plot of the amplitude of the simulated photoacoustic signals at some detector position for a perfect detector (orange) and a bandwidth-limited detector (blue).

systems that visualized the rat brain [125] used a motor to rotate the transducer in a circle, however, this acquisition setup can not cover a full sphere surrounding the rat brain. Both of these challenges would lead to incomplete measurements which might be partially mitigated using compressed sensing that focuses on how to recover the full information from only partial measurements.

4.2 Compressed sensing

The idea of compressed sensing has been developed among different communities with the goal of recovering information for objects of interest from limited measurements [127–129]. The imaging mechanisms in most medical and biophysical imaging modalities such as OAT, CT, MRI and super-resolution microscopy can be considered as linear forward process which can often be modeled as $y = Ax$ where $A \in R^{n \times p}$,

$y \in R^n$ is the measurement data and $x \in R^p$ as shown in Fig. 4.3. Note that there are also nonlinear imaging modalities such as electrical impedance tomography (EIT) from which one hopes to infer the conductivity distribution from partial measurements of the current flux on the boundary [130]. In genomics, the y vector can be gene expression and the x vector can be epigenetic regulations such as histone modifications. In health care studies, the y vector can be the outcome of the patients while x can be different factors such as ages, treatment as well as hospital locations. The forward model can be interpreted in regression point of view where there are a list of statistical and computational ideas that arise in solving this challenge. One central problem in high dimensional inference lies in studying the asymptotic and non-asymptotic behavior of the estimators for x when $p \gg n$, i.e. when the number of covariates is much larger than the number of measurements or when both p and n are very large under which the curse of dimensionality arises [131] and many interesting phenomena such as universality [132, 133], phase transitions [134–138] come up that would have deep connections with probability theory and statistical physics [122, 139–143]. If the number of covariates p is much larger than the number of measurements n , for example, the number of genes in humans is larger than 20000 and one may only have a few hundreds of drug experiments, the problem of identifying the associated genes with drug resistance becomes quite difficult.

One natural effort in compressed sensing tries to answer how one can reconstruct the vector x with knowledge of y for different structures of A under various model assumptions and how one can design efficient algorithms to recover these vectors [122, 144, 145]. Compressed sensing typically makes 'parsimonious' assumption that the vectors of interest are sparse, i.e. $\|x\|_0 = \sum_{j=1}^{p} 1\{|x|_j \neq 0\} \leq s$ where s is some constant, together with p, could characterize the sparsity level. The ratio s/p would be an important parameter that determines the phase transition phenomenon which

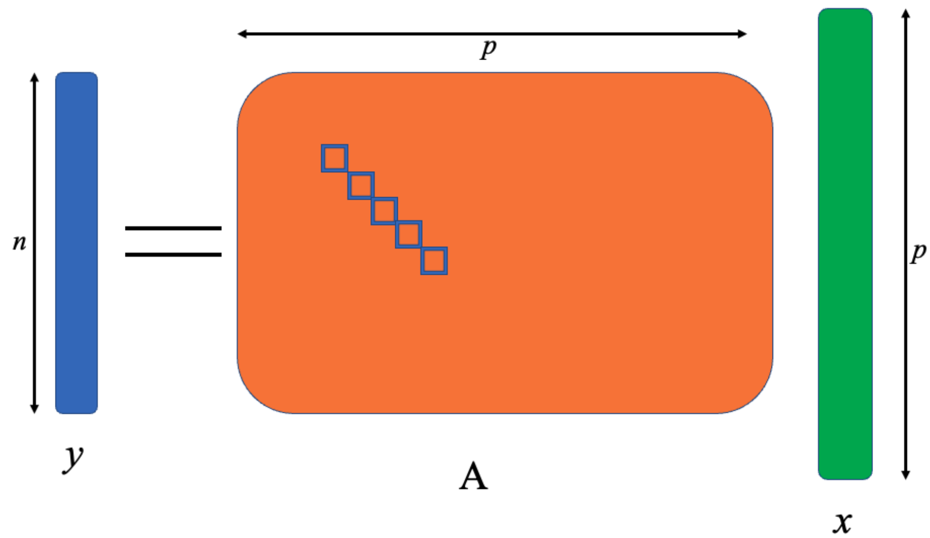

Figure 4.3: Scheme of typical compressed sensing systems. Denote the number of measurements as n and the number of covariates is denoted as p. The structure and properties of A will lead to different algorithms in solving the system.

assemble the phase transitions in statistical physics [146–148]. In the challenge of rare/weak signal detection and recovery in Stein's normal mean model, the phase diagram is characterized by both the fraction of data from a normal with non-null mean and signal strength [149–153].

Under the sparsity assumption, a natural formulation is to minimize $\|x\|_0$ with constraints that $y = Ax$. However the problem is NP-complete and there are no efficient algorithms to solve. The basis pursuit [154] relaxes the problem by changing the minimization of the l_0 norm to the l_1 norm as the l_1 norm is the convex relaxation of the l_0 norm,

$$\min_x \|x\|_1, \quad \text{s.t.} \quad y = Ax. \tag{4.1}$$

The basis pursuit can be solved by linear programming which is available in many computational packages. It has been shown that the basic pursuit can recover the original solution of the compressed sensing problem if certain conditions such as the cone condition and the restricted eigenvalue condition are satisfied [122]. The basis pursuit assumes that the linear model is noiseless, i.e., $y = Ax$ which is a simplified case for the linear model with noise, i.e. $y = Ax + \varepsilon$. Under the noise assumptions, the famous estimator for sparse linear models (Lasso) can be formulated as $\hat{x} = \arg\min_x \frac{1}{2n}\|y - Ax\|_2^2 + \lambda\|x\|_1$. Under some restricted eigenvalue condition and some constraints on λ, the statistical rate of Lasso in l_2 norm is $O(\sqrt{s}\lambda)$ [122].

Beyond the assumptions of x presented above, there might be other structural assumptions which may be generalized to different applications. For example, in the language of sparse regression, the group lasso [155] makes assumptions on the sparsity features in groups, the fused lasso [156] assumes the piecewise-constant of the vector x, the graphical lasso assumes that the associated graph is sparse in high dimensional graphic models [157], and there are some other variants such as adaptive lasso [158], square root lasso [159] and scenarios that make assumptions of the low-rank structure of the matrix [160–162]. In imaging analysis, one would often use total variation [163–165] and wavelet sparsity [166–168] as these priors capture many important features in the images and have tremendous applications [169, 170] such as image restoration [171], super-resolution [172] as well as bioimaging [173] .

There are many kinds of formulation for the total variation regularization, one is the isotropic TV form [163, 174] which is given by $\mathrm{TV}(f) : R^{m\times n} \to R$:

$$\begin{aligned} TV(f) &= \sum_{i=1}^{m-1}\sum_{j=1}^{n-1}\sqrt{(D_x f)_i^2 + (D_y f)_j^2} + \sum_{i=1}^{m-1}|f_{i,n} - f_{i+1,n}| + \sum_{j=1}^{n-1}|f_{m,j} - f_{m,j+1}| \\ &= \sum_{i=1}^{m-1}\sum_{j=1}^{n-1}\sqrt{(f_{i,j} - f_{i+1,j})^2 + (f_{i,j} - f_{i.j+1})^2} + \sum_{i=1}^{m-1}|f_{i,n} - f_{i+1,n}| + \sum_{j=1}^{n-1}|f_{m,j} - f_{m,j+1}| \end{aligned} \tag{4.2}$$

where D_x and D_y are the difference operators and the last two terms deals with the boundary terms.

The other formulation is called the anisotropic TV [174–176] which can be written as,

$$
\begin{aligned}
TV(f) &= \sum_{i=1}^{m-1}\sum_{j=1}^{n-1} |(D_x f)_i| + |(D_y f)_j| + \sum_{i=1}^{m-1} |f_{i,n} - f_{i+1,n}| + \sum_{j=1}^{n-1} |f_{m,j} - f_{m,j+1}| \\
&= \sum_{i=1}^{m-1}\sum_{j=1}^{n-1} |f_{i,j} - f_{i+1,j}| + |f_{i,j} - f_{i.j+1}| + \sum_{i=1}^{m-1} |f_{i,n} - f_{i+1,n}| + \sum_{j=1}^{n-1} |f_{m,j} - f_{m,j+1}|.
\end{aligned}
\tag{4.3}
$$

A salient feature of the difference operator is that the action of the difference operator on an image can be interpreted as a convolution of the image with some certain kernels. This property would be useful in implementing the difference operator. The explicit circulant matrix might also be constructed, however, that would take more efforts than coding the matrix operation into a convolution operator as many signal processing tools are readily available.

In some cases, the problems of interest can be formulated as statistical inverse problems where wavelet decomposition [177–179], deconvolution [180–182] and shrinkage approaches [183–185] can be employed.

4.3 Datasets and representation

Most machine learning models would require a large training dataset so that the model can learn the underlying features sufficiently. As a very new imaging modality, there are no known large databases for photoacoustic imaging data. One approach in creating large training datasets for photoacoustic imaging would be to use the image datasets from other measurements such as CT, MRI, PET, etc. Photoacoustic imaging mostly focuses on visualizing vascular structures hence one possible source

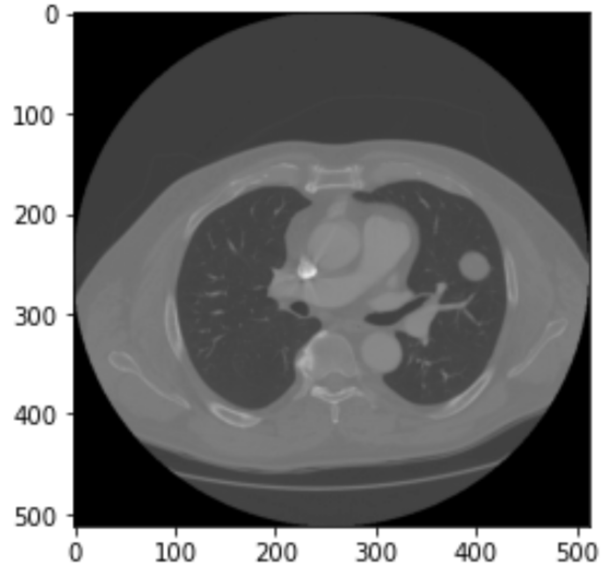

Figure 4.4: Plot of one sample lung CT data from LIDC-IDRI dataset.

of ground truth images may be downloaded from CT imaging databases which are already widely available.

Here the images were downloaded from the database Lung Image Database Consortium image collection (LIDC-IDRI) that consists of lung computed tomography (CT) scans. The data was processed using traditional CT data processing pipelines. The 3D lung CT images were segmented into smaller volumes and projected into the x, y, z axis to obtain the 2D vascular structures as shown in Fig. 4.5. We selected the structures that have significant vascular features as our training data.

Figure 4.6 shows some snapshots of the vessel structures that were produced in one projection and segmentation. These images are completely different, however they share some underlying low dimensional features. One can extract the low-dimensional features in these images to use for prediction in the machine learning models by various approaches. In image analysis, an image can typically be represented by low-dimensional features, one of the most important and straightforward approaches are

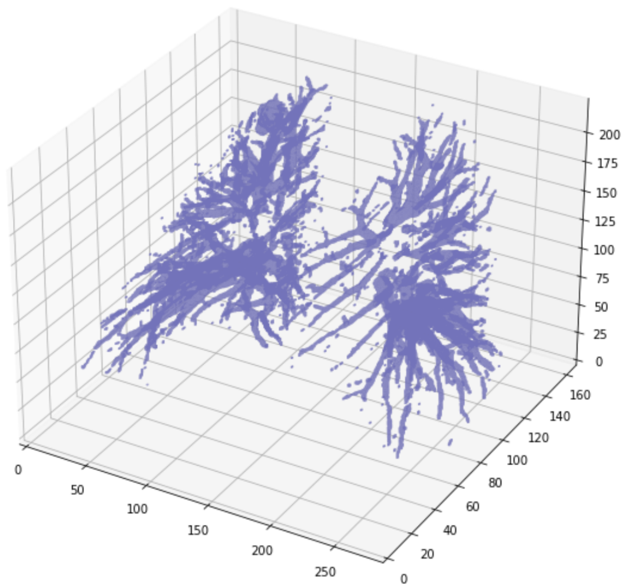

Figure 4.5: 3D Plot of the lung CT scan data after processing. The blood vessels are extracted and highlighted.

the nonnegative matrix factorization [186] and the most well-known method principal component analysis (PCA) [187]. Assume that we have n images $X \in R^{\{k*k,n\}}$ where k is the dimension of each image, the matrix X can be decomposed into the product of two nonnegative matrices U and V,

$$X \approx UV^T, \tag{4.4}$$

where $U \in R^{k^2 \times r}$ and $V \in R^{n \times r}$. The nonnegative decomposition has demonstrated its ability to successfully find the parts-based representations, for example, the eyes, ears and noses in the human faces dataset [186]. Nonnegative matrix factorization can discover these parts-based representations, while other matrix factorizations such as LU, Cholesky and QR decomposition can not. Section 4.5 will discuss recent approaches, deep generative models such as variational autoencoder and deep convolutional generative adversarial networks that use neural networks to encode the

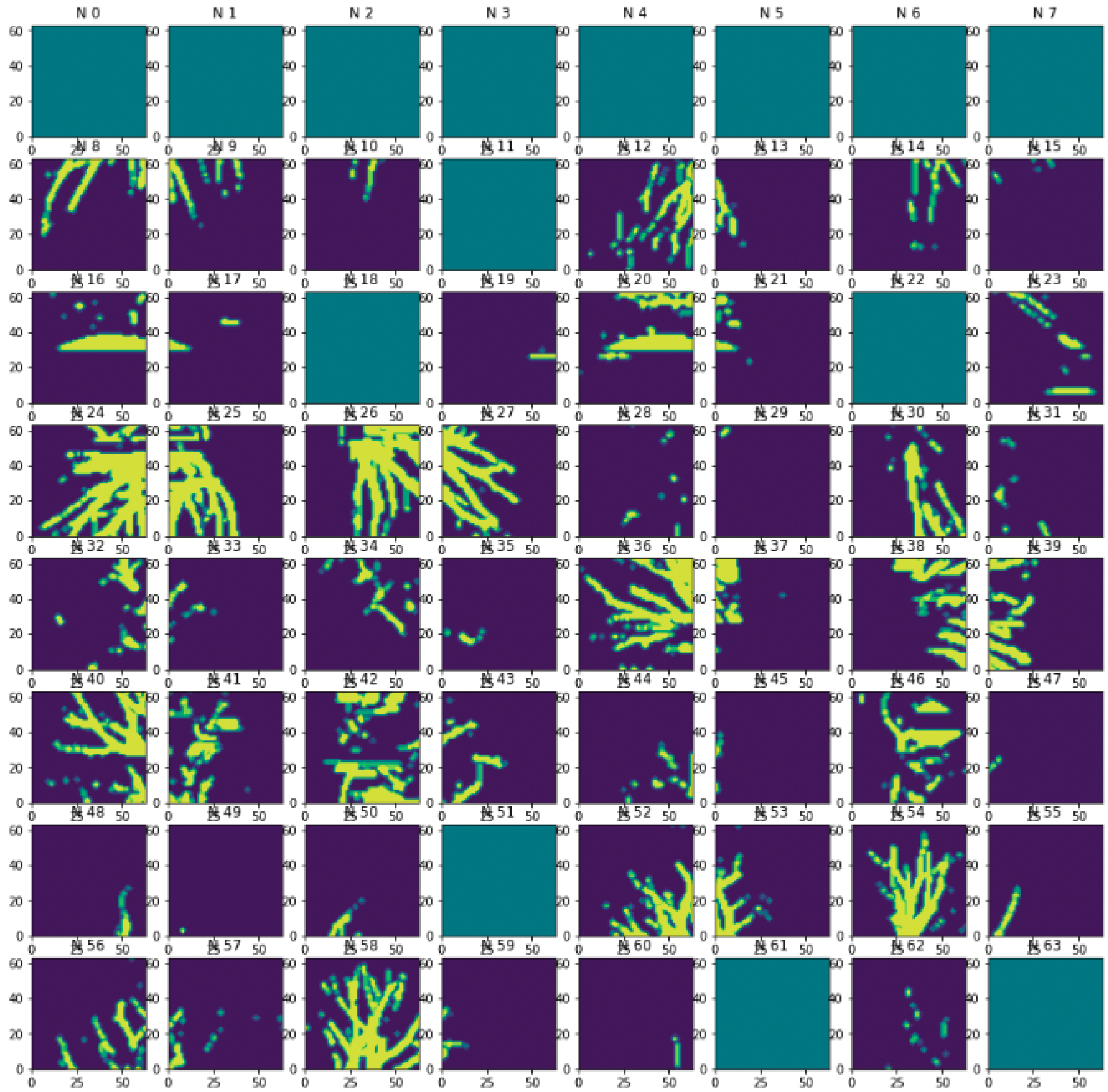

Figure 4.6: Projection and segmentation of the 3D lung CT data into 2D. The structures that have the vessel features are selected into the training dataset.

information of images into some low-dimensional manifolds. These representations are highly nonlinear due to the complexity of the neural networks and hence would often be able to capture higher order nonlinear features in the image datasets [188,189].

4.4 Optimization

In practice one often has to solve the optimization problem $\min_{x \in X} f(x) + g(x)$ where $f(x)$ is convex and smooth, $g(x)$ is usually not smooth. In the case that the problem does not have constraint, i.e. $X = R^d$, if $g(x) = 0$ one may use the gradient descent method for smooth $f(x)$ and Nestrov's smoothing method for non-smooth $f(x)$ [190–192]. If $g(x) \neq 0$, one might use proximal methods that approximate the object function by quadratic terms. In the case there is a constraint, i.e. X belongs to a subset of R^d, then the widely used method would be the constrained gradient descent methods such as Frank-Wolfe algorithm which is essentially a projected gradient descent [190–192]. However the gradient descent methods such as Frank-Wolfe algorithm have $O(1/t)$ convergence rate and would take a long time to exploit the parameter space [190–192]. There have been accelerated gradient descent methods such as Nestrov's accelerated gradient descent which would achieve $O(1/t^2)$ convergence rate while the traditional gradient descent methods would be $O(1/t)$ [193]. Other popular methods might include mirror descent that utilize distance metric different from l_2 norm, such as relative entropy and Hellinger distance [194].

Iterative shrinkage thresholding Algorithm (ISTA), fast iterative shrinkage thresholding algorithm (FISTA) [195] and alternating direction method of multipliers (ADMM) are very popular algorithms for solving the optimization challenges for nonzero $g(x)$ and have demonstrated wide applications in the imaging sciences [196, 197]. Here we discuss different priors and derive the corresponding descriptions for optoacoustic tomography.

4.4.1 Fixed priors: l_1, l_2 and total variation

Consider the linear forward model $y = Ax + \varepsilon$ where $y \in R^n$, $A \in R^{n\times p}$, $x \in X = [0,1]^p$. One would often scale the images to the range $[0,1]$ and flatten the images to be a vector. Here the simplest proximal gradient algorithms with constraints $x \in X = [0,1]^p$ are presented.

(I) We first consider l_2 penalty which is related with Tikhonov regularization [198–200] with constraints $x \in X = [0,1]^p$, in regression language, the l_2 penalty is related with ridge regression [201]. The optimization can be formulated as,

$$\begin{aligned}\hat{x} &= \arg\min_{x\in X=[0,1]^p}\left\{\frac{1}{2}\|y-Ax\|_2^2+\lambda\|x\|_2^2\right\}\\ &= \arg\min_{x\in R^p}\left\{\frac{1}{2}\|y-Ax\|_2^2+\lambda\|x\|_2^2+h(x)\right\}.\end{aligned} \tag{4.5}$$

where $h(x)$ is defined to be,

$$h(x) = \begin{cases} 0, & \text{for } 0 \le x \le 1 \\ \infty, & \text{otherwise} \end{cases}$$

Denote the step size as $\eta = 1/L$, L is the Lipschitz constant related with the matrix A, typically L should be greater than or equal to $\frac{2}{tr(A^TA)}$ to ensure convergence. The following iterative algorithm can be derived,

$$x_{t+1} = \text{prox}_{\eta g}\Bigg(x_t - \eta A^T(Ax_t - y)\Bigg), \tag{4.6}$$

where the formula for $\mathrm{prox}_{\eta g}$ in this case can be derived as:

$$[\mathrm{prox}_{\eta g}(x)]_i = \begin{cases} 0, & \text{for } x_i \leq \eta\lambda \\ \frac{x_i}{1+2\eta\lambda}, & \text{for } \eta\lambda \leq x_i \leq 1+2\eta\lambda \\ 1, & \text{for } x_i \geq 1+2\eta\lambda \end{cases}$$

The above procedures are ISTA based algorithms with convergence rate $O(1/t)$. FISTA based algorithms would have the following modified procedures which would lead to $O(1/t^2)$ convergence,

$$x_{t+1} \leftarrow \mathrm{prox}_{\eta g}\Bigg(v_t - \eta A^T(Av_t - y)\Bigg), \tag{4.7}$$

$$q_t \leftarrow (1 + \sqrt{1 + 4q_{t-1}^2})/2, \tag{4.8}$$

$$v^t \leftarrow x^t + \frac{q_{t-1} - 1}{q_t}(x_t - x_{t-1}), \tag{4.9}$$

where the initial conditions are taken to be $v^0 = x^0$ and $q_0 = 1$. FISTA has been widely applied in the total variation imaging denoising as well as other linear inverse problems [195, 196].

(II) l_1 penalty has been widely used in compressed sensing in imaging owing to the nice properties of convex optimization [128, 166, 202, 203]. In linear and generalized linear models, l_1 penalty is related with the famous Lasso for sparse regression [118, 204, 205]. We first consider the proximal gradient with l_1 penalty with constraints

$x \in X = [0,1]^n$,

$$\hat{x} = \arg \min_{x \in X=[0,1]^p} \left\{ \frac{1}{2}\|y - Ax\|_2^2 + \lambda \|x\|_1 \right\} \tag{4.10}$$

$$= \arg \min_{x \in R^p} \left\{ \frac{1}{2}\|y - Ax\|_2^2 + \lambda \|x\|_1 + h(x) \right\}, \tag{4.11}$$

Let $\eta = \frac{1}{L}$ where η is the stepsize, Equation 4.11 would lead to the following iterative algorithms,

$$x_{t+1} = \text{prox}_{\eta g}\left(x_t - \eta A^T(Ax_t - y) \right), \tag{4.12}$$

where

$$\text{prox}_{\eta g} = \arg \min_{z \in R^p} \frac{1}{2}\|z - x\|^2 + \eta g(z) = \arg \min_{z \in [0,1]^p} \frac{1}{2}\|z - x\|^2 + \eta\lambda\|z\|_1. \tag{4.13}$$

The formula for $\text{prox}_{\eta g}$ can be derived as,

$$[\text{prox}_{\eta g}(x)]_i = \begin{cases} 0, & \text{for } x_i \leq \eta\lambda \\ x_i - \eta\lambda, & \text{for } \eta\lambda \leq x_i \leq 1 + \eta\lambda \\ 1, & \text{for } x_i \geq 1 + \eta\lambda \end{cases}$$

(III) Total variation is a prior that could promote sparsity and allow the images to preserve sharp edges and discontinuities. In addition to the iterative shrinkage algorithms [195, 196], the optimization with total variation regularization could be solved with primal-dual algorithms [197] and alternating direction method of multipliers (ADMM). ADMM is an iterative method that splits the object function into different components and solve it using the proximal operators [206, 207]. It is often used when the proxy is not easy to write as a closed form expression. Using the augumented lagrangian [174, 206, 207], one can obtain the following algorithm for ADMM with TV regularization. The optimization can be written as,

$$\hat{x} = \arg\min_x \frac{1}{2}\|Ax - y\|_2^2 + \lambda TV(x), \tag{4.14}$$

where $TV(x)$ is defined in Section 4.2. Eq. 4.14 is equivalent with the problem $\hat{x} = \arg\min_x \frac{1}{2}\|Ax - y\|_2^2 + \lambda TV(z)$ that satisfys $Dx = z$, where $D = [D_x^T, D_y^T]^T \in R^{2n,n}$ is the difference operator.

Denote $f(x) = \frac{1}{2}\|Ax - y\|_2^2$ and $g(z) = \lambda TV(z)$, the Lagrangian can be written as,

$$L(x, z, \phi) = f(x) + g(z) + \phi^T(Dx - z) + \frac{\rho}{2}\|Dx - z\|_2^2. \tag{4.15}$$

The iterative algorithm can thus be derived as [174, 207],

$$x \leftarrow \arg\min_x \frac{1}{2}\|Ax - y\|_2^2 + \frac{\rho}{2}\|Dx - z + \frac{1}{\rho}\phi\|_2^2, \tag{4.16}$$

$$z \leftarrow \arg\min_z \lambda TV(z) + \frac{\rho}{2}\|Dx - z + \frac{1}{\rho}\phi\|_2^2, \tag{4.17}$$

$$\frac{1}{\rho}\phi \leftarrow \frac{1}{\rho}\phi + Dx - z. \tag{4.18}$$

In summary, one would have the following x-update and z-update [174, 207]:

$$x \leftarrow (A^TA + \rho D^TD)^{-1}\left(A^Ty + \rho D^T(z - \frac{1}{\rho}\phi)\right), \tag{4.19}$$

and $[z]_i = [Dx]_i - \frac{\phi_i}{\rho}$, if $[Dx]_i + \frac{\phi_i}{\rho} \geq \frac{\lambda}{\rho}$ and $[z]_i = [Dx]_i + \frac{\phi_i}{\rho}$, if $[Dx]_i + \frac{\phi_i}{\rho} \leq \frac{\lambda}{\rho}$.

Note that in addition to the continuous approaches, there have been discrete approaches for the optimization challenge such as dynamic programming [208], stimulated annealing [209] as well as message passing [210]. Markov random fields models [142, 211] have been very successful in the application of the statistical physics ideas to the imaging processing such as image denoising.

4.4.2 Other general priors

In Section 4.4.1, iterative algorithms with different priors such as l_1, l_2 and TV priors are presented. These algorithms are deterministic, once the prior is given, the minimization problem becomes fixed and a list of fast algorithms have been proposed to solve these problems including FISTA, ADMM and so on [54, 195, 207].

An adjustment comes that if the prior is not given but learned from data. The core ideas of the above models lie in the different designs for removal Gaussian noise under the model assumption of white noise. As neural networks are great functional approximators [212, 213], there are many approaches to construct neural networks that function as a Gaussian denoiser. Other approaches might include the Plug-and-Play Prior (P^3) [214, 215] and Regularization by Denoising (RED) [216] that exploit the implicit priors for any general inverse problems.

Another alternative choice comes after the invention of the convolutional neural networks (CNNs) which have been applied in the denoising tasks using stochastic algorithms such as ADAM which is a first order gradient based stochastic optimization method by Kingma and Ba [217]. Further, deep CNNs (DnCNN) has been proposed as an effective Gaussian image denoiser in Ref. [218]. It consists of three types layers including Conv+ReLu, Conv+BN+ReLU and Conv layers. Recent denoising models such as DnCNN can act as a general prior in solving the inverse problem, distinct from the traditional l_1, l_2 and TV priors in Section 4.4.1.

Stochastic solutions for the inverse problems have been proposed including SNIPS which samples from the posterior distribution by Langevin dynamics [219] and score-matching which differ from the classical maximum a posteriori (MAP) estimation [220]. There are some connections between the convex optimization and Hamilton-Jacobi PDEs which would have applications in the imaging sciences [221–223].

4.5 Compressed sensing using generative models

Deep Learning, based on different architectures of neural networks, has transformed many research areas including computer vision and natural language processing in the last decade [213]. It has been applied extensively in various disciplines of physical [224, 225] and life sciences recently including genomics [226], medical imaging [227], computational chemistry [228], etc. There are a list of amazing works on deep learning for inverse problems [229–232]. In contrast to the classical model-based approaches for linear inverse problems, deep learning methods for solving tomographic imaging reconstruction are often a combination of model-based approaches and data-driven techniques [233–235]. For example, in photoacoustic tomography, some researchers used iterated backprojection to reconstruct the initial photoacoustic images and then trained a U-Net to improve the reconstruction quality which outperformed the conventional filtered back-projection methods [42, 236]. Deep learning approaches for photoacoustic imaging are still growing fast and there have already been several reviews on this topic [36, 237]. However there are several problems in these approaches, for example the results depend on the network parameters and the model often ignores the underlying physics such as the governing partial differential equations (PDEs). The data-driven approach brings advantages but would also face challenges. There are approaches that encode more physics into the model such as partial differential equations [238, 239], however, the curse of dimensionality would still persist. Besides, another big issue comes from the lack of *in vivo* imaging data while most deep learning models relies significantly on both the quality and quantity of training data [36]. Despite the improvements by many researchers, there is still a long way to go for deep learning models to be applicable for real clinical applications.

Compressed sensing using deep generative models has been proposed in Ref. [240]. Following this work, posterior sampling estimator has been proposed using Langevin dynamics to learn the generative priors and has shown great promise in clinical MRI imaging data [241, 242]. The median-of-means modification of the CSGM estimator has also been proposed for heavy tailed measurements [243]. The main idea for the series of work is to relax assumptions on the sparsity of the estimation object but to assume that the samples lie on some low dimensional manifold that can be estimated from data. If the model is able to learn the underlying low dimensional manifolds from a large set of training data, then it might be used to generate samples that resemble the key features of the real images. Of note that different from PCA, which is linear, deep generative models are able to learn highly nonlinear features underlying the training images due to the complexity of the neural networks.

There are a series of generative models architectures [244], among which the variational autoencoders (VAEs) that minimize the evidence lower bound (ELBO) defined by Kullback–Leibler divergence [188], has gained much success in different applications and has been well-studied.

We first trained convolutional variational autoencoder (CVAE) on training dataset where each image $x \in X$ is assumed to be characterized by some low dimensional representation z. The mapping which is described by a function $G : R^d \to R^{n^2}$ where the latent dimension d is typically much smaller than the image dimension n^2 can be learned from the training dataset. Combining ideas from compressed sensing [240],

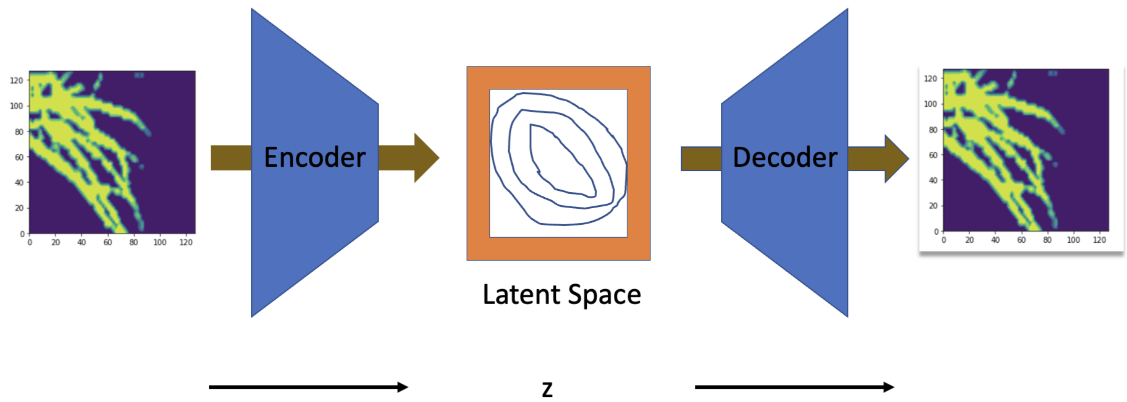

Figure 4.7: Scheme of Conditional Variational Autoencoder.

the following optimization problem can be formulated to minimize the measurement error which is defined as,

$$\min_{z} \|y - AG(z)\|_2^2. \tag{4.20}$$

One can obtain good representation $G(z)$ by training deep generative models using a large amount of training data and the sensing step essentially finds the best reconstructed image that minimized the l_2 loss of measurements with the measurements predicted by the generative model. Theoretical bounds that analyze the sample complexity using restricted eigenvalue condition have been given in Ref. [240]. After obtaining the ground truth dataset as discussed in Section 4.3, we can generate the simulated measurement data using the k-wave package which is available in MATLAB to simulate the photoacoustic wave propagation and generation of time series measurement data [34]. The simulation of measurement data depends on the imaging geometry as well as the physical conditions of the experimental setup which together would define the forward operator A. For simple two dimensional cases, it is possible to construct the matrix A explicitly if small number of grid points is used. We can set each position in the 2D grids to be 1 and other positions as 0 to simulate a single source, run one simulation and then record the signal which is the Green's function response at each position. By linear superposition principle of the acoustic waves generated, it is possible to obtain the matrix A by recording the responses from each position at all computational grids.

Figure 4.10 shows one sample training data set which can be represented as matrix of size 128×128. Figure 4.11 shows the simulated acoustic measurement from this particular training image. We set the grid point spacing in the x and y directions both as $dx = dy = 100\ \mu m$. The sound speed is set to be 1500 m/s. The time step is set to be $dt = dx/c$. The number of total time steps is set to be 256. Hence the size of the forward matrix A would be $(256 \times 128, 128^2)$ for this two dimensional simulation.

We trained CVAE as our generative model on 50000 images for 300 epochs. The network parameters for the CVAE architecture are shown in Fig. 4.8 (encoder) and Fig. 4.9 (decoder). After training CVAE, for each test measurement data y, stochastic gradient descent was used to find the vector $\hat{z}$ corresponding to each measurement y and the reconstructed image is $G(\hat{z})$. Experiments were conducted in two scenarios: 1) limited-view setup with 32 perfect acoustic detectors in a line; 2) limited-view setup with 32 bandlimited acoustic detectors in a line where the center frequency is set to be 2.5 MHz and the bandwidth of the transducer as 95%.

For the baseline total variation regularization with ADMM solver, grid search was conducted in different combinations of ρ and λ. The best parameter is found to be $\rho = 0.05$ and $\lambda = 10^{-3}$ and the number of iterations as 50 (after 50 iterations there are no significant changes of the reconstruction results).

Table 4.1: PSNR, SSIM for limited-view experimental desgin

	TV	CVAE
PSNR	22.35	28.19
SSIM	0.8347	0.9290

```
_________________________________________________________________
 Layout (type)                Output Shape              Param #
=================================================================
 conv2d (Conv2D)              (None, 63, 63, 32)        320

 conv2d_1 (Conv2D)            (None, 31, 31, 64)        18496

 flatten (Flatten)            (None, 61504)             0

 dense (Dense)                (None, 2048)              125962240

=================================================================
Total params: 125,981,056
Trainable params: 125,981,056
Non-trainable params: 0
```

Figure 4.8: Encoder parameters in the CVAE architecture.

```
_________________________________________________________________
 Layer (type)                 Output Shape              Param #
=================================================================
 dense_1 (Dense)              (None, 65536)             67174400

 reshape (Reshape)            (None, 32, 32, 64)        0

 conv2d_transpose (Conv2DTra  (None, 64, 64, 64)        36928
 nspose)

 conv2d_transpose_1 (Conv2DT  (None, 128, 128, 32)      18464
 ranspose)

 conv2d_transpose_2 (Conv2DT  (None, 128, 128, 1)       289
 ranspose)

=================================================================
Total params: 67,230,081
Trainable params: 67,230,081
Non-trainable params: 0
```

Figure 4.9: Decoder parameters in the CVAE architecture.

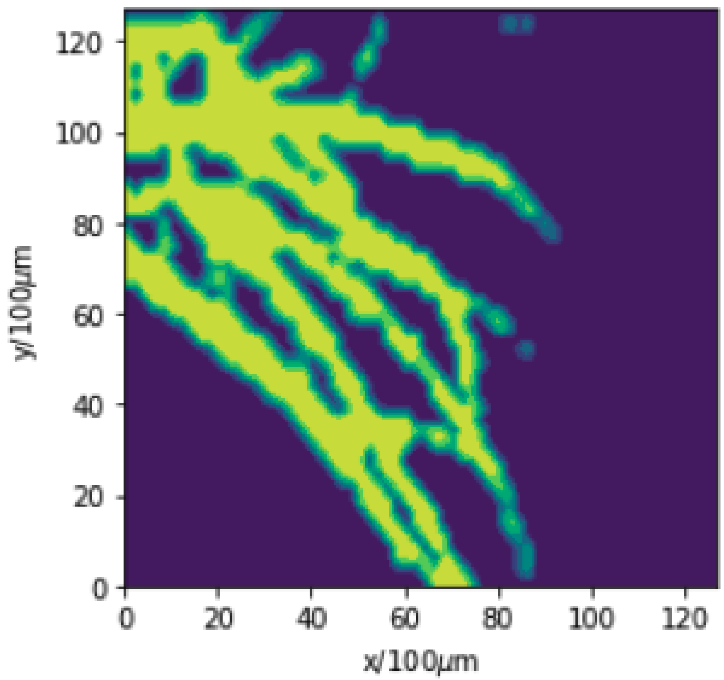

Figure 4.10: One sample training data of blood vessel. The image is normalized to range (0,1). The yellow color represents the vessel and the purple represents the background with the value zero.

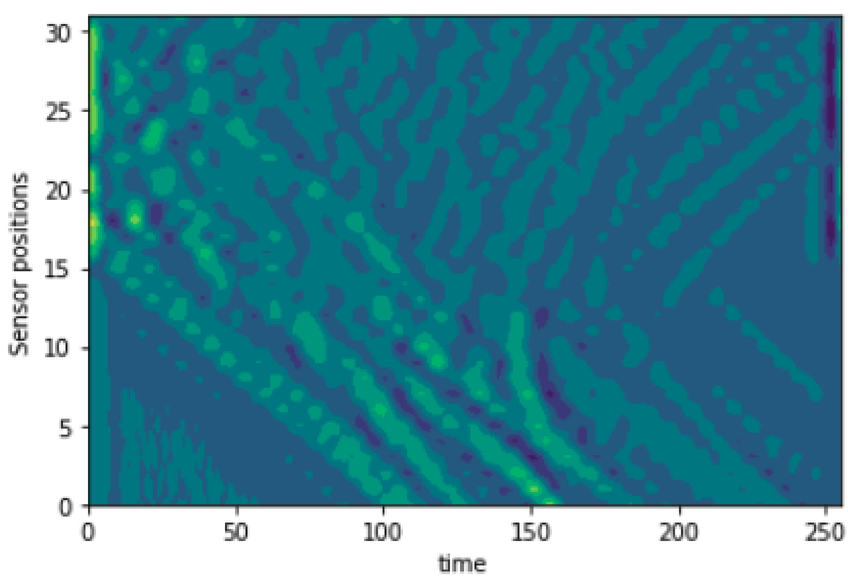

Figure 4.11: One sample simulated acoustic time series measurement. There are 32 sensors distributed uniformly along the $x = 0$ axis and the time step is taken to be dx/c.

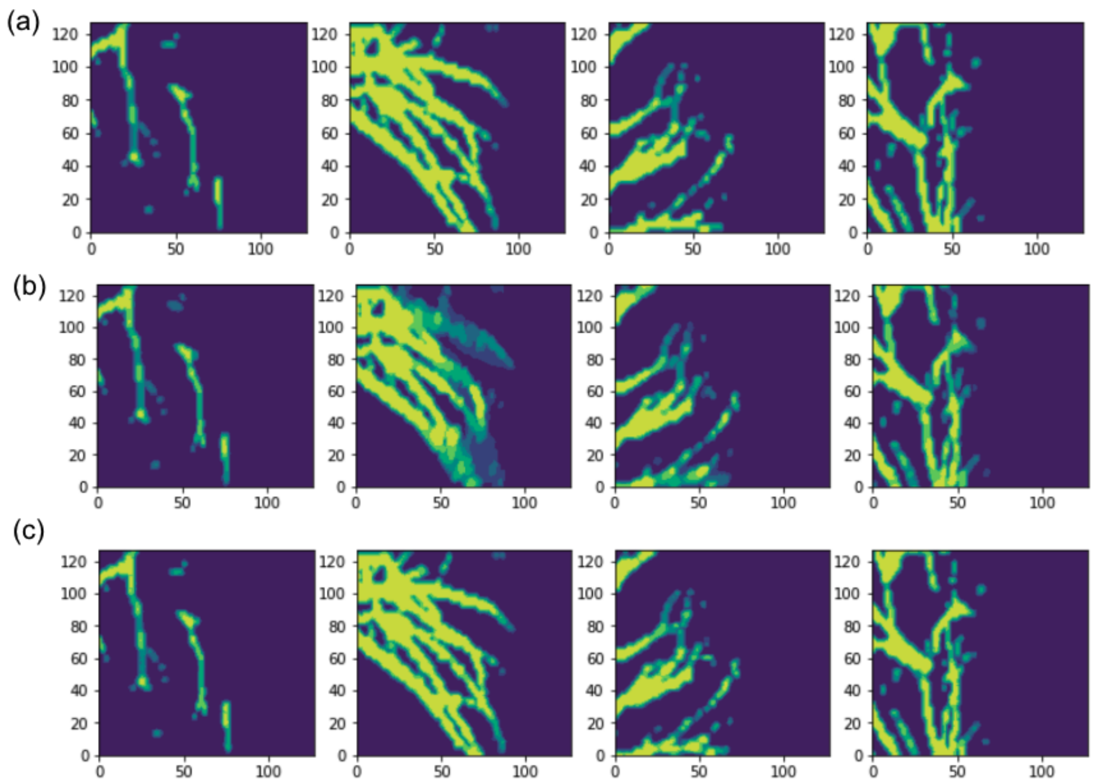

Figure 4.12: Reconstruction results for three sample images in the limited-view experimental design (a) True Images, (b) total variation reconstruction, (c) CVAE reconstruction.

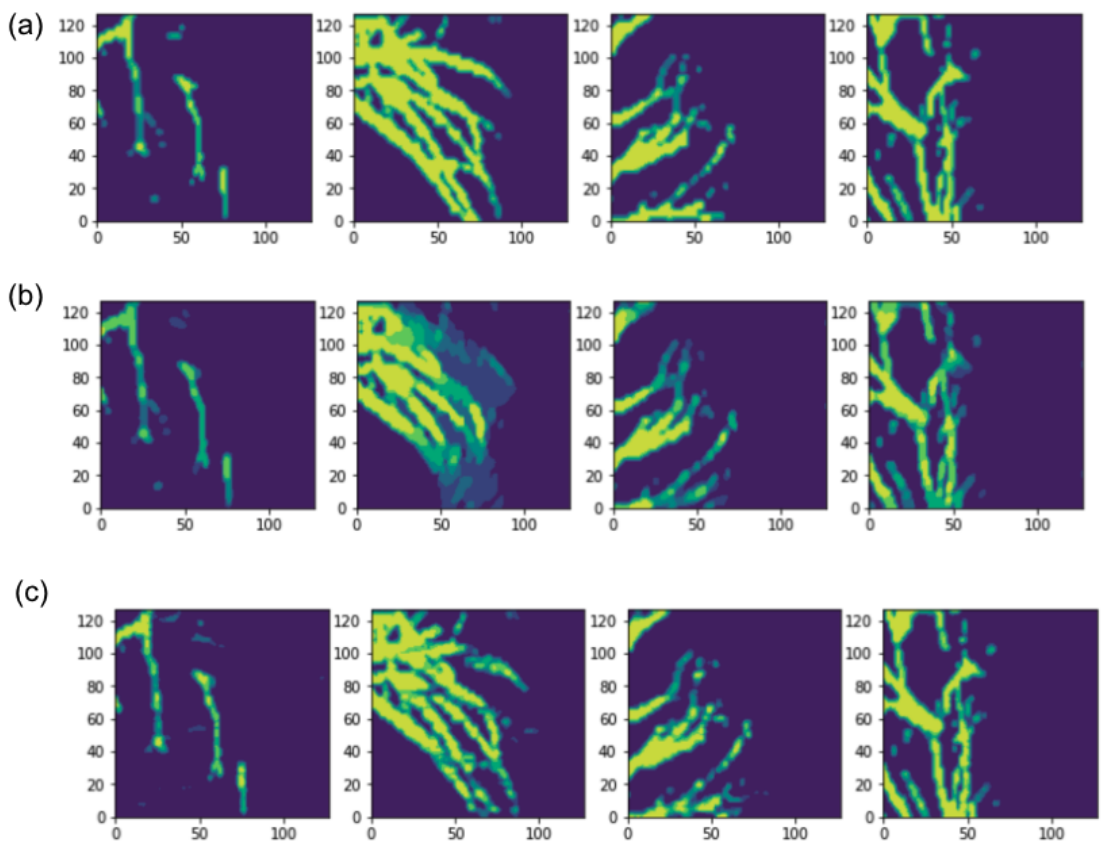

Figure 4.13: Reconstruction for three images in the limited-view and bandwidth limited design (a) True Images, (b) total variation reconstruction, (c) CVAE reconstruction.

Table 4.2: PSNR, SSIM for limited-view and bandwidth-limited experimental desgin

	TV	CVAE
PSNR	19.06	20.36
SSIM	0.6211	0.8429

Three sample images as well as the corresponding measurements are selected and the reconstruction results are shown for both the limited-view simulation (Fig. 4.12) as well as the limited-view and bandwidth-limited simulation (Fig. 4.13). Figure 4.12 and Figure 4.13 show that the model compressed sensing using CVAE has better reconstruction results for both limited-view and bandwidth-limited simulations than the best performance of the conventional total variation regularization. The quantitive results are shown in Table 4.1 and Table 4.2 where PSNR and SSIM for 500 test images are presented. PSNR represents the peak signal-to-noise ratio, the bigger, the better the reconstruction. SSIM represents the structural similarity index measure which represents the similarity between two images. We can see that the reconstructed images from compressed sensing with CVAE has significantly better results in terms of structural similarity. When the experimental design only involves the limited-view issue, the CVAE has much better PSNR than total variation, but as we include the bandwidth-limited issue, PSNR for both methods decrease and the difference between the two becomes smaller. Overall, compressed sensing with CVAE can outperform the best performance of total variation regularization. In terms of computational times, compressed sensing using CVAE is around 10 times faster than total variation using ADMM, while achieving much better reconstruction results.

With the advance of all kinds of generative models including flow-based generative models [245, 246] and scored-based generative models [247–249], the inverse problems in imaging would embrace new tools and opportunities that may push the current limit in resolution, accuracy and imaging speed [250, 251].

4.6 Discussion

Although machine learning approaches have been able to mitigate part of the difficulties that traditional methods suffer from, there is still a long way to go to improve the computational models so that they might be used in real clinical applications. There have been comprehensive reviews on modern regularizations methods [54], Bayesian approaches [252] and data-driven approaches [235] for inverse problems.

Without an attempt to summarize the field, here a few challenges that face machine learning approaches for photoacoustic imaging are presented.

(I) Computational Time

Photoacoustic imaging often involves 3D reconstruction of the initial pressure and further optical absorption coefficients. The iterative approaches, which have been quite successful in overcoming some of the subsampling and bandwidth-limited issues, would require long computational time to converge as these algorithms often involve simulating the forward and adjoint operator in each iteration. Besides, the sparsity level, for example, λ in the TV regularization, would change for different datasets and experimental setups and one often have to do grid searches and cross-validation to find the optimal parameter each time. This would further increase the computational burden.

(II) Uncertainty Quantification

The reconstruction process would give an estimate to the image of interest, which is often far from perfect. Quantification of the uncertainties of the estimators could be much harder than the estimation problem itself. There would be 'deterministic' errors such as errors arising from numerical scientific computing. Another uncertainty might come from the randomness in the physical process. There will be different combination of all kinds of noise including shot noise, Poisson noise and $1/f$ noise where most well-established algorithms focus on the Gaussian denoising. How to develop robust models that can account for the physical nature of the randomness in the measurements would be an interesting area to explore as well.

(III) Domain Adaptability

Domain adaptability deals with whether the model would generate well outside the training data. For example, if one wants to analyze data from one MRI machine trained on the data from Rhode Island hospitals using deep neural networks and later they want to analyze the data from the same MRI machine collected from Boston hospitals using the same model, do they have any guarantee that they can use the same parameters for the trained neural networks in Rhode Island? For deep learning models trained in some particular sets of photoacoustic images, for example, healthy group lung images, will the models be able to reconstruct the precise tumor features in patient groups? Are there any theoretical guarantee for the performance of the deep learning models? Different communities including theoretical computer science [253, 254] and some recent works in statistics [255] have been devoted on different aspects of learning algorithms that can account for domain adaptability issues.

In summary, the area of machine learning in the photoacoustic imaging, more broadly, inverse problems in imaging, is still growing which would benefit from the advancement of many related fields. For example, the intersection of deep learning and scientific computing [256, 257] would allow researchers to simulate the wave propagation more accurately in a much shorter time which would be essential for developing the next generation photoacoustic imaging algorithms.

Chapter 5

X-ray phase contrast imaging

> “The worthwhile problems are the ones you can really solve or help solve, the ones you can really contribute something to. No problem is too small or too trivial if we can really do something about it. ”
>
> – Richard P. Feynman

Optoacoustic tomography has gained much success in bioimaging and its spatial resolution is typically around a few hundreds microns. The X-ray diffraction imaging, owing to its unique wavelength range and penetration depth, could achieve a few hundreds even tens of nanometers spatial resolution [258, 259]. Chapter 5 will present a fast evaluation method of Fresnel integrals for X-ray phase contrast imaging and discuss the phase retrieval challenge.

X-ray phase contrast images can be calculated numerically using the Fresnel integral. Unfortunately, the highly oscillatory nature of the integrand means that its evaluation can require large amounts of computer time. The problem becomes more severe as the wavelength of the X-radiation becomes shorter. Here the use of the fast Fourier transform is discussed. Examples are given for plane wave and point sources and for the more difficult problem of finite sources. The phase retrieval which is the corresponding inverse problem for the forward imaging process based on X-ray diffraction will be discussed at the end of Chapter 5.

5.1 Overview

The advent of spatially coherent X-ray sources such as microfocus X-ray tubes and X-ray synchrotrons has made possible X-ray imaging that has both phase and absorption contrast, the former capable of outlining fine features in the object. Phase contrast arises from deflection of X-radiation as it passes through samples possessing gradients in index of refraction [260–262]. With conventional X-ray sources the large electron beam spot on the anode yields an X-ray beam that averages over the phase contrast features which tend to be composed of primarily high spatial frequencies. With highly coherent X-ray sources, the phase contrast in the image highlights boundaries in the object wherever sharp variations in index of refraction are found.

One of the simplest experimental arrangement for recording a phase contrast image uses an in line optical train where the object is interposed between the source and object plane. An in line X-ray image that includes phase and absorption can be calculated using the Fresnel-Kirchhoff integral [263–266], however, as the integral is highly oscillatory computation resulting in excessive computation time. Examples of evaluation of the Fresnel-Kirchhoff can be found for micron sized objects in Ref. [265, 267, 268]. Here we show the fast Fourier transform can be used to advantage to evaluate the Fresnel-Kirchhoff integral for plane wave and point sources in one dimension and for heterodyne images where a grating is placed in the optical train [269–271].

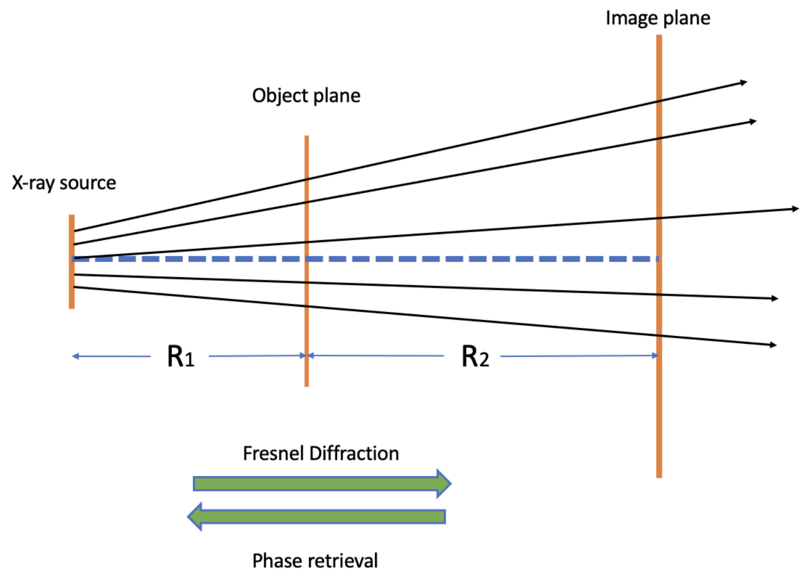

Figure 5.1: Scheme of a typical X-ray phase contrast imaging setup. The distance between the X-ray source and the object plane is R_1 and the distance between the object plane and the image plane is R_2. The forward process is described by Fresnel diffraction and the inverse process is called phase retrieval.

5.2 Plane wave images

Consider the image generated by a one-dimensional object as shown in Fig. 5.1. The expression for the field amplitude in arbitrary units is given by [263, 266, 267] as

$$f(x) = \left(\frac{i}{\lambda z}\right) e^{-ikz} \int q(X) e^{-\frac{ik(x-X)^2}{2z}} dX \tag{5.1}$$

where $q(X)$ is a transmission function that describes the phase and absorption introduced by the object, taken to be of the form

$$q(x) = e^{i\phi(x)-\mu(x)} \tag{5.2}$$

where z is the distance between the object and the image plane, λ is the wavelength of the X-radiation, considered to be monochromatic, k is the wavenumber and x is the distance from the origin in the image plane x. The phase for a flat layer ϕ is given by $k\delta t$ where t is the thickness and δ is the index of refraction decrement; the absorption is given by $\mu = \mu_0 t$. The electric field amplitude given by Eq. 5.1 is of the form of a convolution of two functions q_1 and q_2

$$f(x) = \left(\frac{i}{\lambda z}\right) e^{-ikz} \int q_1(X) q_2(x - X) dX \tag{5.3}$$

It follows [272] that the Fourier transform of Eq. 5.1, we obtain,

$$F(q) = Q_1(u) Q_2(u) \tag{5.4}$$

where $Q_1(u) = \mathcal{F}(q_1(x))$ and $Q_2(u) = \left(\frac{i}{\lambda z}\right) \mathcal{F}(e^{-\frac{ikx^2}{2z}}) = e^{i\pi\lambda z u^2}$. The exponential prefactor in Eq. 5.1 has been deleted as it does not influence the image intensity. The computational procedure is thus to calculate a table of values of $q_1(x)$ together with a table of values of the various x_i for the i values chosen, to carry out numerical Fourier transformation of the $q_1(x)$ table to obtain $Q_1(u)$, and then to multiply each value of $Q_1(u)$ by $Q_2(u)$ to obtain $F(q)$. This procedure requires a single numerical Fourier transformation to obtain F. The Fourier transform of the phase and absorption function is carried out so that the range of coordinates is from $-Xend$ to $Xend$, which is made large enough to entend over the full length of the object, which is placed symmetrically with respect to the origin. The number of points pts, determines the range of u values as $pts/Xend$. The image intensity is then determined using the inverse Fourier transform to determine the field amplitude, which, in turn, is used to determine the absolute value squared of the transform to give the image intensity $I(x)$ which can be written as $f(x) = \mathcal{F}^{-1}\{F(q)\}$ and $I(x) = |f(x)|^2$.

Figure 5.2 shows examples of the use of this procedure to determine images from a flat of width $2a$ and thickness t, a cylinder with radius a, and a Gaussian function described by the following transmission functions in Table 5.1.

Table 5.1: Absorption $\mu(x)$ and phase $\phi(x)$ for flat, cylindrical and exponential objects

Object	Absorption $\mu(x)$	Phase $\phi(x)$
Flat	$\mu_0 t$	$k\delta t$
Cylinder	$2\mu_0 a\sqrt{1-(x/a)^2}$	$2k\delta a\sqrt{1-(x/a)^2}$
Exponential	$\mu_0 t(1-e^{-(x/a)^2})$	$k\delta t[1-e^{-(x/a)^2}]$

It is of note that the execution time for the calculations required only a few seconds using MATLAB on a personal computer.

5.3 Point source images

The expression for the electric field amplitude corresponding to Eq. 5.1 for a point source of radiation is given by [266, 267]

$$f(x) = \left(\frac{i}{\lambda z}\right) e^{-ikR_2} \int q(X) e^{-\frac{ikX^2}{2R_1}} e^{-\frac{ik(x-X)^2}{2R_2}} dX \tag{5.5}$$

where R_1 and R_2 are the distances between the point source and object and the object and the image, respectively. The magnification in the image is given by $\frac{R_1+R_2}{R_1}$. As in the plane wave case, the Fourier transform of Eq. 5.5 can be written as a convolution in the form of Eq. 5.3 by grouping the first two factors in the integrand which can be numerically transformed and finding an analytical solution for the transform of the third factor so that $Q_1(u) = \mathcal{F}\left(q_1(x)e^{-\frac{ikx^2}{2R_1}}\right)$ and $Q_2(u) = e^{i\pi\lambda z u^2}$.

In carrying out the calculation, a table of $q_1(x)$ is calculated and Fourier transformed. Each element of this table is then multiplied by the corresponding elements of $Q_2(u)$ to give a final table that is inverse transformed and squared. An example of

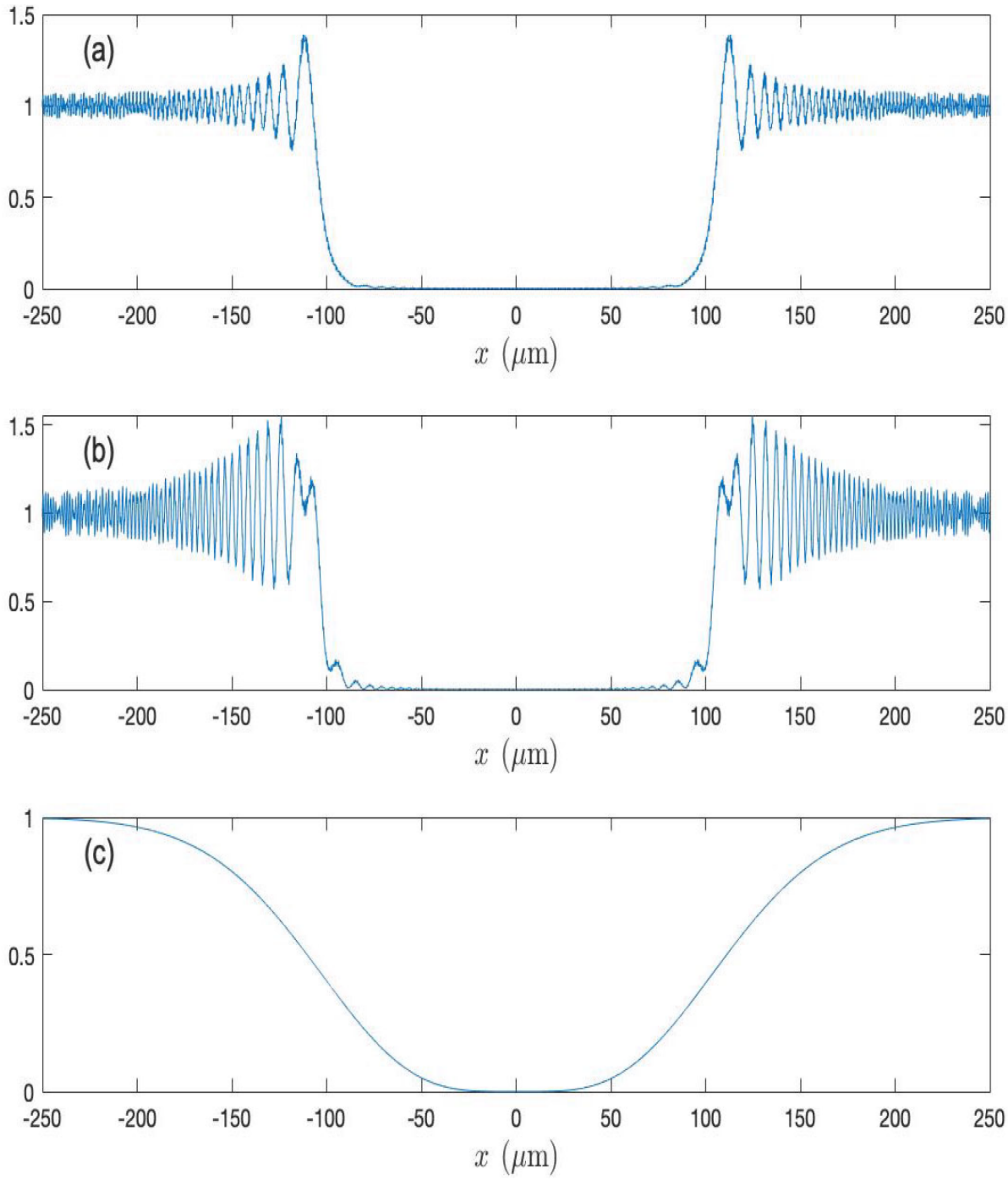

Figure 5.2: Phase contrast images of (a) a 200 μm wide flat with thickness $t = 100$ μm, (b) a 200 μm diameter rod, and (c) a Gaussian function with the functional form listed in Table 5.1 with the parameters a =100 μm and t =100 μm. The calculations were carried out with the radiation wavelength $\lambda = 0.1$Å, an absorption coefficient $\mu_0 = 2.8 \times 10^4/m$ and the phase function decrement $\delta = 3.84 \times 10^{-6}$. The Fourier transform parameters were $Xend$=250 μm and $pts = 40,000$.

the use of this procedure is given by the image in Fig. 5.3 calculated for a flat with a magnification of 1.5.

5.4 Source with finite dimensions

When the source has a finite dimension the Fresnel-Kirchhoff integral becomes a function of an additional parameter ξ which is a coordinate on the source plane so that the field amplitude is found by first finding

$$f(x,\xi) = \left(\frac{i}{\lambda z}\right) e^{-ikR_2} \int q_1(X) e^{-\frac{ik(\xi-X)^2}{2R_1}} e^{-\frac{-ik(x-X)^2}{2R_2}} dX \tag{5.6}$$

which is then integrated over the source distribution taken here to be a Gaussian function with a distance parameter σ to give

$$f(x) = \int f(x,\xi) e^{-(\xi/\sigma)^2} d\xi \tag{5.7}$$

Two factors can be identified to give $F(q,\xi) = Q_1(u,\xi)Q_2(u)$ where $Q_1(u,\xi) = \mathcal{F}\Big(q_1(x)e^{\frac{-ik(\xi-x)^2}{2R_1}}\Big)$ and $Q_2(u) = e^{i\pi\lambda z u^2}$. Once the two factors are multiplied to give $F(q,\xi)$ determined at a single value of ξ, a value of $f(x,\xi)$ is found by inverse Fourier transformation of $F(q,\xi)$. A table of values of $f(x,\xi_j)f(x,\xi_j)^*$ for image intensity at x from a source point ξ_j is calculated for a number of j values which is used for numerical integration according to Eq. 5.7. It can be seen from Fig. 5.4 that the averaging of the intensity over a source dimension of tens of microns, characteristic of commercially available microfocus X-ray tubes still leaves strong, easily visualized phase constrast features in the image irrespective of whether the object is a defined inert sample or biological tissue [273].

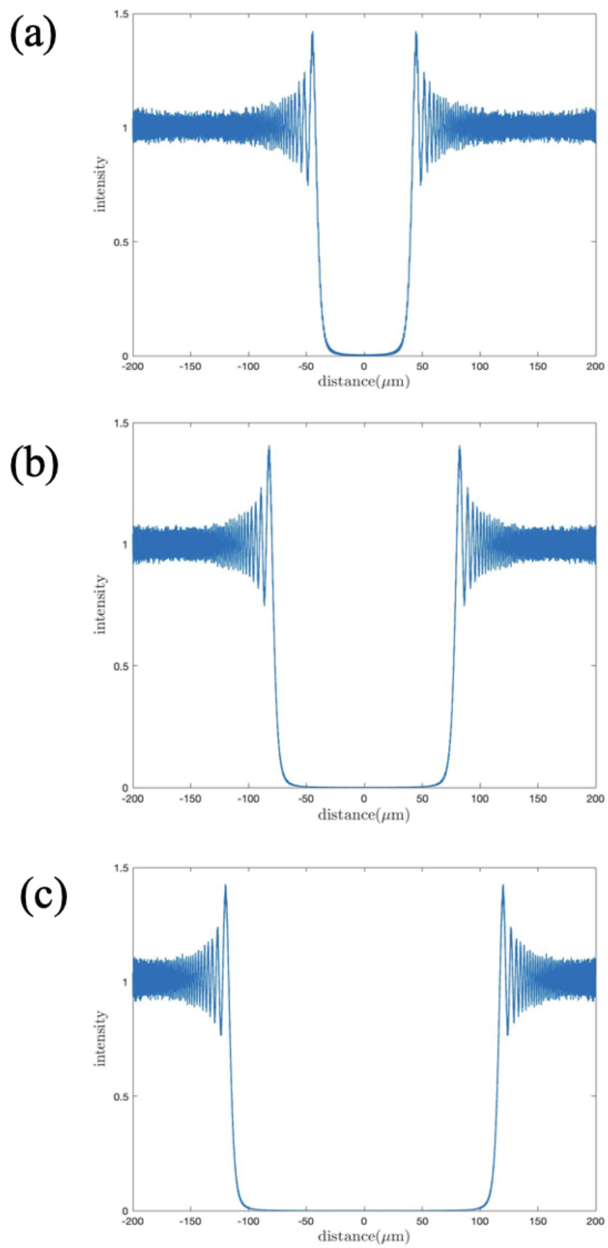

Figure 5.3: X-ray phase contrast images for (a) a 50 μm wide flat, (b) 100 μm wide flat and (c) 150 μm wide flat with $R_1 = 1$, $R_2 = 0.5$. The X-ray energy is set to be 12 keV. The Fourier transform parameters $Xend$ is set to be 1000 μm and $pts = 30000$.

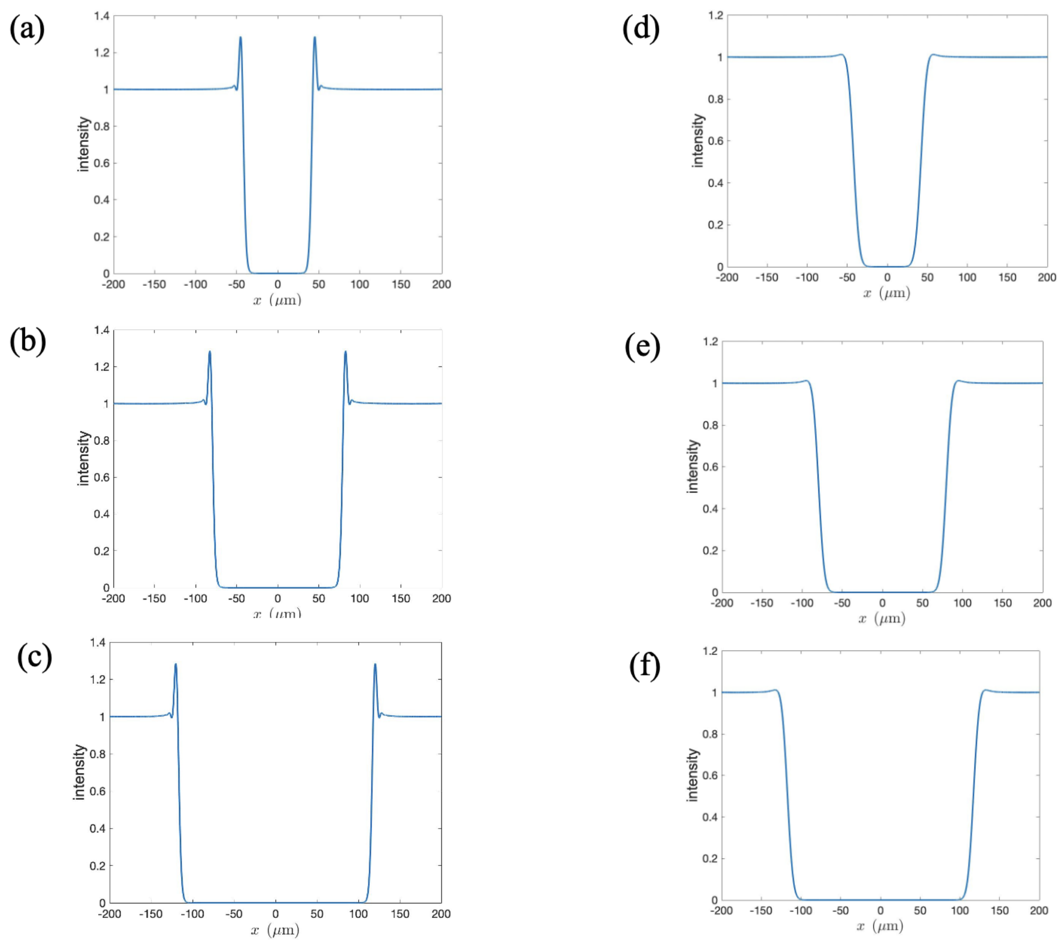

Figure 5.4: X ray phase contrast images for gold (a)-(c) with source size 6.75 μm and (d)-(f) with source size 20 μm for (a) and (d) 50 μm cube, (b) and (e) 100 μm cube, (c) and (f) 150 μm cube. The Fourier transform parameters pts is taken to be 30000, $Xend$ is taken to be 1000 μm with magnification 1.5.

5.5 Heterodyne images

It has been shown [269–271, 273, 274] that placement of an absorption grating in contact with the object in the optical train of an in-line phase contrast imaging apparatus results in an increase in image contrast when harmonics of the grating in the image are selected. Here a grating whose transmission is taken to be a square wave is placed in the object plane causing a modification in the overall object transmission function. The field amplitude for a source with a finite dimension is

$$f(x,\xi) = \left(\frac{i}{\lambda z}\right) e^{-ikR_2} \int q_1(X) g(X) e^{-\frac{ik(\xi-X)^2}{2R_1}} e^{-\frac{-ik(x-X)^2}{2R_2}} dX \tag{5.8}$$

where the square wave function $g(x)$ [275] can be written as an expansion in cosine functions as

$$g(x) = \frac{1}{2} + \frac{2}{\pi} \sum_{j=1}^{\infty} \frac{(-1)^{j-1}}{(2j-1)} \cos(2j-1)k_g x \tag{5.9}$$

where k_g is the grating wavenumber. The Fourier transform of f is thus of the form $F(u) = Q_1(u)Q_2(u)$ where where $Q_1(u,\xi) = \mathcal{F}\Big(q_1(x)g(x)e^{\frac{-ik(\xi-x)^2}{2R_1}}\Big)$ and $Q_2(u) = e^{i\pi\lambda z u^2}$.

5.6 Phase retrieval challenge

The X-ray diffraction imaging has great potential for visualizing the nanoscale structures with fascinating breakthroughs in bioimaging. For example, single mimivirus has been imaged with a resolution of a few tens of nanometers by a single X-ray diffraction pattern without the need for sample crystallization [259]. The imaging of the subtle neuronal structures in biological tissues at resolution smaller than a hundred nanometer in a mm-sized sample volumes has been demonstrated using X-ray holographic nano-tomography (XNH) [258]. The inverse problem of the forward Fresnel-Kirchhoff integral is called phase retrieval. A series of works in X-ray phase contrast imaging start from the transport-of-intensity equation to derive the algorihm for phase retrieval [276, 277]. In X-ray phase contrast imaging, one early important contribution would be Paganin's method for phase and amplitude retrieval that assumes the homogeneity of the object [277]. This method along with different variants, due to their simplicity and applicability, are still widely used in modern applications [258].

The area of coherent diffractive imaging (CDI) has been very active in recent years. The goal of CDI is to develop mathematical tools and computational algorithms to recover the phase information of the object of interest without the need to use many lens in diffraction experiments due to the limitation of availability for the specific lens functioning at the X-ray wavelength [278, 279]. It would be of great interest whether the spatial resolution of the samples could be pushed towards the atomic resolution and the temporal resolution of the chemical reactions towards femtoseconds [280–282] even attosecond [283] by these advanced algorithms.

The general phase retrieval challenge for X-ray diffraction can be formulated as recovering $f(t)$ given the measurements $|\hat{f}(\omega)|^2 = |\int_{t\in T} f(t)e^{-i\omega t}|^2$ [284]. Much efforts have focused on the alternating projection algorithms [285,286] to solve the nonconvex optimization problem where the very early effort was the reconstruction of an object from the modulus of the Fourier transform by Fienup [287]. Recent progress has been made by adding random modulation (coded diffraction pattern) which can give theoretical guarantee for the phase retrieval for which the reconstruction performance is related with the number of coded diffraction patterns [288,289]. A series of advanced algorithms have been proposed for phase retrieval including PhaseLift [288–290] which is based convex programming, PhaseMax [291, 292] which is based on linear programming and Wirtinger flow [288, 293] which is based on gradient descent methods where universality phenomena was discovered for different design matrix [294, 295]. There are a list of recent efforts in using randomness and probabilistic analysis to push the limit for the fundamental bounds of optimal sensing [296–300]. The proof of these kinds of bounds would usually involve the tail and concentration equalities, high dimensional probability well as random matrix theory [122, 301–303].

The phase retrieval challenges would, in general, have connections with inverse problems in photoacoustic imaging. They both belong to the subject of inverse problems which are very active areas in applied mathematics with wide applications in science and engineering. The solution to one problem might shed light to the other.

Chapter 6

Conclusion

> "It is not knowledge, but the act of learning, not possession but the act of getting there, which grants the greatest enjoyment."
>
> – Carl Friedrich Gauss

This thesis centers different aspects of the photoacoustic effect. Chapter 1 focuses on the physical process that generates photoacoustic effect including spherical droplets, fluid layers as well as oscillating delta sources in a one-dimensional oscillator. The development of quantitative optoacoustic tomography requires a thorough understanding of the photoacoustic pressure generation process. Different micro- and nanosized absorbers can be used as contrast agents in photoacoustic imaging owing to the large amplitude pressure waves generated. We studied the photoacoustic effect generated within a spherical droplet for two cases: a sphere with a surrounding region of fluid that absorbs radiation and a sphere that absorbs radiation itself. Analytical solutions to the photoacoustic wave equation in the frequency and time domain were derived. High amplitude transients, compressions in the former and rarefactions in the latter, were shown to be generated within the droplets as the waves approach the center of the droplet. We investigated the properties of the photoacoustic effect when a continuous wave laser beam is moving back-and-forth in a one-dimensional resonator. The pressure is found to increase linearly with the number of sweeps across the resonator according to linear acoustic theory.

Chapter 3 focuses on the detection of photoacoustic waves by optical deflection. A salient feature of the photoacoustic effect is that the temporal and spatial characteristics of the ultrasound waves generated encode information such as geometry and sound speed as well as density of the irradiated body. We can infer these properties by detection of the emitted acoustic waves. The conventional way for detection of photoacoustic waves using ultrasonic transducers would suffer from either low bandwidth or low sensitivity issues. We proposed new methods of determining photoacoustic waveforms using recordings of optical beam deflections. Optical recording of photoacoustic waves is expected to provide unique advantages due to the high speed response of the optical detectors and freedom from the distortion that accompanies conventional piezoelectric transducers.

Chapter 4 focuses on one prominent application of the photoacoustic effect: the optoacoustic tomography. The computational way to alleviate the current limitations such as limited-view, sub-sampling as well as finite-bandwidth in optoacoustic tomography is to introduce regularizations such as total variation and wavelet sparsity in solving the inverse problems. We discussed the conventional ways of solving linear inverse problems including ISTA, FISTA and ADMM with l_1, l_2 and total variation regularization which do not fully exploit the available dataset. Besides these approaches suffer from high computational burden especially for the 3D *in vivo* optoacoustic tomography. Chapter 4 combines compressed sensing with deep generative models such as CVAE to solve inverse problems in optoacoustic tomography.

Chapter 5 focuses on X-ray phase contrast imaging. We present a fast evaluation method of the Fresnel-Kirchhoff integral for plane wave and point sources in one dimension, for heterodyne images where a grating is placed in the optical train and are able to determine the effects of source dimensions on resolution.

Modern biophysics and biological imaging would require a thorough understanding of the physical mechanism in the experiments as well as quantitative descriptions and inference of observations. The thesis reveals parts of the efforts in combining mathematics and computation to bridge the gap between theory and experiments for better designing and understanding of these complex yet intriguing biological measurements.

Bibliography

[1] Xingchi Yan and Gerald J Diebold. Generation of high amplitude compressions and rarefactions in a photoacoustically excited droplet. *Photoacoustics*, 23:100289, 2021.

[2] Xingchi Yan and Gerald J Diebold. Abel inversion of optical beam deflection signals from photoacoustic waves with symmetry in one, two, and three dimensions. *Journal of Applied Physics*, 130(21):214902, 2021.

[3] V. E. Gusev and A. A. Karabutov. *Laser Optoacoustics*. American Institute of Physics, New York, 1993.

[4] Allan Rosencwaig. *Photoacoustics and Photoacoustic Spectroscopy*. Wiley, New York, 1980.

[5] P. M. Morse and K. U. Ingard. Theoretical acoustics. *Harwood Academic*, 1991.

[6] P. J. Westervelt and R. S. Larson. Laser-excited broadside array. *J. Acoust. Soc. Am.*, 54:121–122, 1973.

[7] G. J. Diebold, T. Sun, and M. I. Khan. Photoacoustic monopole radiation in one, two, and three dimensions. *Phys. Rev. Lett.*, 67:3384–3387, 1991.

[8] G. J. Diebold and T. Sun. Properties of photoacoustic waves in one, two, and three dimensions. *Acta Acust. united Ac.*, 80:339–351, 1994.

[9] Alexander Graham Bell. Upon the production and reproduction of sound by light. *Journal of the Society of Telegraph Engineers*, 9(34):404–426, 1880.

[10] Alexander Graham Bell. Lxviii. upon the production of sound by radiant energy. *The London, Edinburgh, and Dublin Philosophical Magazine and Journal of Science*, 11(71):510–528, 1881.

[11] Jane Hodgkinson and Ralph P Tatam. Optical gas sensing: a review. *Measurement science and technology*, 24(1):012004, 2012.

[12] Peter Hess. Resonant photoacoustic spectroscopy. In *Physical and Inorganic Chemistry*, pages 1–32. Springer, 1983.

[13] MW Sigrist. Air monitoring by laser photoacoustic spectroscopy. *Air monitoring by spectroscopic techniques*, 127:163–238, 1994.

[14] Allan Rosencwaig and Allen Gersho. Theory of the photoacoustic effect with solids. *Journal of Applied Physics*, 47(1):64–69, 1976.

[15] Thomas L Szabo. Time domain wave equations for lossy media obeying a frequency power law. *The Journal of the Acoustical Society of America*, 96(1):491–500, 1994.

[16] W Chen and S Holm. Modified szabo's wave equation models for lossy media obeying frequency power law. *The Journal of the Acoustical Society of America*, 114(5):2570–2574, 2003.

[17] Siegfried Ginter, Marko Liebler, Eckard Steiger, Thomas Dreyer, and Rainer E Riedlinger. Full-wave modeling of therapeutic ultrasound: Nonlinear ultrasound

propagation in ideal fluids. *The Journal of the Acoustical Society of America*, 111(5):2049–2059, 2002.

[18] James F Kelly, Robert J McGough, and Mark M Meerschaert. Analytical time-domain green's functions for power-law media. *The Journal of the Acoustical Society of America*, 124(5):2861–2872, 2008.

[19] Wen Chen and Sverre Holm. Fractional laplacian time-space models for linear and nonlinear lossy media exhibiting arbitrary frequency power-law dependency. *The Journal of the Acoustical Society of America*, 115(4):1424–1430, 2004.

[20] Bradley E Treeby and Ben T Cox. Modeling power law absorption and dispersion for acoustic propagation using the fractional laplacian. *The Journal of the Acoustical Society of America*, 127(5):2741–2748, 2010.

[21] Benjamin T Cox, S Kara, Simon R Arridge, and Paul C Beard. k-space propagation models for acoustically heterogeneous media: Application to biomedical photoacoustics. *The Journal of the Acoustical Society of America*, 121(6):3453–3464, 2007.

[22] T Douglas Mast, Laura M Hinkelman, Michael J Orr, Victor W Sparrow, and Robert C Waag. Simulation of ultrasonic pulse propagation through the abdominal wall. *The Journal of the Acoustical Society of America*, 102(2):1177–1190, 1997.

[23] David Gottlieb and Eli Turkel. Dissipative two-four methods for time-dependent problems. *Mathematics of computation*, 30(136):703–723, 1976.

[24] Sigal Gottlieb, Chi-Wang Shu, and Eitan Tadmor. Strong stability-preserving high-order time discretization methods. *SIAM review*, 43(1):89–112, 2001.

[25] Dietrich Braess. *Finite elements: Theory, fast solvers, and applications in solid mechanics*. Cambridge University Press, 2007.

[26] Randall J LeVeque et al. *Finite volume methods for hyperbolic problems*, volume 31. Cambridge university press, 2002.

[27] Claes Johnson. *Numerical solution of partial differential equations by the finite element method*. Courier Corporation, 2012.

[28] Alexandre Ern and Jean-Luc Guermond. *Theory and practice of finite elements*, volume 159. Springer, 2004.

[29] Huabei Jiang, Zhen Yuan, and Xuejun Gu. Spatially varying optical and acoustic property reconstruction using finite-element-based photoacoustic tomography. *JOSA A*, 23(4):878–888, 2006.

[30] Bengt Fornberg. *A practical guide to pseudospectral methods*. Number 1. Cambridge university press, 1998.

[31] Makoto Tabei, T Douglas Mast, and Robert C Waag. A k-space method for coupled first-order acoustic propagation equations. *The Journal of the Acoustical Society of America*, 111(1):53–63, 2002.

[32] Xiaojuen Yuan, D Borup, J Wiskin, Michael Berggren, and Steven A Johnson. Simulation of acoustic wave propagation in dispersive media with relaxation losses by using fdtd method with pml absorbing boundary condition. *IEEE transactions on ultrasonics, ferroelectrics, and frequency control*, 46(1):14–23, 1999.

[33] Jean-Pierre Berenger. A perfectly matched layer for the absorption of electromagnetic waves. *Journal of computational physics*, 114(2):185–200, 1994.

[34] Bradley E Treeby and Benjamin T Cox. k-wave: Matlab toolbox for the simulation and reconstruction of photoacoustic wave fields. *Journal of biomedical optics*, 15(2):021314, 2010.

[35] Minghua Xu and Lihong V Wang. Universal back-projection algorithm for photoacoustic computed tomography. *Physical Review E*, 71(1):016706, 2005.

[36] Andreas Hauptmann and Ben T Cox. Deep learning in photoacoustic tomography: current approaches and future directions. *Journal of Biomedical Optics*, 25(11):112903, 2020.

[37] Yuan Xu, Lihong V Wang, Gaik Ambartsoumian, and Peter Kuchment. Reconstructions in limited-view thermoacoustic tomography. *Medical physics*, 31(4):724–733, 2004.

[38] Stephen J Norton. Reconstruction of a two-dimensional reflecting medium over a circular domain: Exact solution. *The Journal of the Acoustical Society of America*, 67(4):1266–1273, 1980.

[39] David Finch and Sarah K Patch. Determining a function from its mean values over a family of spheres. *SIAM journal on mathematical analysis*, 35(5):1213–1240, 2004.

[40] David Finch, Markus Haltmeier, and Rakesh. Inversion of spherical means and the wave equation in even dimensions. *SIAM Journal on Applied Mathematics*, 68(2):392–412, 2007.

[41] Leonid A Kunyansky. Explicit inversion formulae for the spherical mean radon transform. *Inverse problems*, 23(1):373, 2007.

[42] Stephan Antholzer, Markus Haltmeier, and Johannes Schwab. Deep learning for photoacoustic tomography from sparse data. *Inverse problems in science and engineering*, 27(7):987–1005, 2019.

[43] Peter Burgholzer, Christian Hofer, Günther Paltauf, Markus Haltmeier, and Otmar Scherzer. Thermoacoustic tomography with integrating area and line detectors. *IEEE transactions on ultrasonics, ferroelectrics, and frequency control*, 52(9):1577–1583, 2005.

[44] Guenther Paltauf, Robert Nuster, Markus Haltmeier, and Peter Burgholzer. Photoacoustic tomography using a mach-zehnder interferometer as an acoustic line detector. *Applied optics*, 46(16):3352–3358, 2007.

[45] Peter Burgholzer, Johannes Bauer-Marschallinger, Hubert Grün, Markus Haltmeier, and Günther Paltauf. Temporal back-projection algorithms for photoacoustic tomography with integrating line detectors. *Inverse Probl.*, 23(6):S65, 2007.

[46] David J Gross. The role of symmetry in fundamental physics. *Proceedings of the National Academy of Sciences*, 93(25):14256–14259, 1996.

[47] Bradley E Treeby, Edward Z Zhang, and Benjamin T Cox. Photoacoustic tomography in absorbing acoustic media using time reversal. *Inverse Problems*, 26(11):115003, 2010.

[48] Jianliang Qian, Plamen Stefanov, Gunther Uhlmann, and Hongkai Zhao. An efficient neumann series–based algorithm for thermoacoustic and photoacoustic tomography with variable sound speed. *SIAM Journal on Imaging Sciences*, 4(3):850–883, 2011.

[49] Plamen Stefanov and Gunther Uhlmann. Thermoacoustic tomography with variable sound speed. *Inverse Problems*, 25(7):075011, 2009.

[50] L. Wang, editor. *Photoacoustic Imaging and Spectroscopy.* CRC Press, Boca Raton, 2009.

[51] Amir Rosenthal, Daniel Razansky, and Vasilis Ntziachristos. Fast semi-analytical model-based acoustic inversion for quantitative optoacoustic tomography. *IEEE transactions on medical imaging*, 29(6):1275–1285, 2010.

[52] Chao Huang, Kun Wang, Liming Nie, Lihong V Wang, and Mark A Anastasio. Full-wave iterative image reconstruction in photoacoustic tomography with acoustically inhomogeneous media. *IEEE transactions on medical imaging*, 32(6):1097–1110, 2013.

[53] Simon R Arridge, Marta M Betcke, Ben T Cox, Felix Lucka, and Brad E Treeby. On the adjoint operator in photoacoustic tomography. *Inverse Problems*, 32(11):115012, 2016.

[54] Martin Benning and Martin Burger. Modern regularization methods for inverse problems. *Acta Numerica*, 27:1–111, 2018.

[55] Lian Xiong, Wenyu Bai, Feifei Chen, Xian Zhao, Fapeng Yu, and Gerald J Diebold. Photoacoustic trace detection of gases at the parts-per-quadrillion level with a moving optical grating. *Proceedings of the National Academy of Sciences*, 114(28):7246–7249, 2017.

[56] Ekaterina I Galanzha, Evgeny V Shashkov, Thomas Kelly, Jin-Woo Kim, Lily Yang, and Vladimir P Zharov. In vivo magnetic enrichment and multiplex

photoacoustic detection of circulating tumour cells. *Nature nanotechnology*, 4(12):855–860, 2009.

[57] Hao F Zhang, Konstantin Maslov, George Stoica, and Lihong V Wang. Functional photoacoustic microscopy for high-resolution and noninvasive in vivo imaging. *Nature biotechnology*, 24(7):848–851, 2006.

[58] Lihong V Wang. Tutorial on photoacoustic microscopy and computed tomography. *IEEE Journal of Selected Topics in Quantum Electronics*, 14(1):171–179, 2008.

[59] Lihong V Wang and Junjie Yao. A practical guide to photoacoustic tomography in the life sciences. *Nature methods*, 13(8):627–638, 2016.

[60] Benjamin T Cox, Jan G Laufer, Paul C Beard, and Simon R Arridge. Quantitative spectroscopic photoacoustic imaging: a review. *Journal of biomedical optics*, 17(6):061202, 2012.

[61] Jun Xia, Muhammad R Chatni, Konstantin I Maslov, Zijian Guo, Kun Wang, Mark A Anastasio, and Lihong V Wang. Whole-body ring-shaped confocal photoacoustic computed tomography of small animals in vivo. *Journal of biomedical optics*, 17(5):050506, 2012.

[62] Robert A Kruger, Richard B Lam, Daniel R Reinecke, Stephen P Del Rio, and Ryan P Doyle. Photoacoustic angiography of the breast. *Medical physics*, 37(11):6096–6100, 2010.

[63] Amit P Jathoul, Jan Laufer, Olumide Ogunlade, Bradley Treeby, Ben Cox, Edward Zhang, Peter Johnson, Arnold R Pizzey, Brian Philip, Teresa Marafioti, et al. Deep in vivo photoacoustic imaging of mammalian tissues using a tyrosinase-based genetic reporter. *Nature Photonics*, 9(4):239–246, 2015.

[64] Todd N Erpelding, Chulhong Kim, Manojit Pramanik, Ladislav Jankovic, Konstantin Maslov, Zijian Guo, Julie A Margenthaler, Michael D Pashley, and Lihong V Wang. Sentinel lymph nodes in the rat: noninvasive photoacoustic and us imaging with a clinical us system. *Radiology*, 256(1):102, 2010.

[65] Chi Zhang, Konstantin Maslov, and Lihong V Wang. Subwavelength-resolution label-free photoacoustic microscopy of optical absorption in vivo. *Optics letters*, 35(19):3195–3197, 2010.

[66] Junjie Yao, Konstantin I Maslov, Yu Zhang, Younan Xia, and Lihong V Wang. Label-free oxygen-metabolic photoacoustic microscopy in vivo. *Journal of biomedical optics*, 16(7):076003, 2011.

[67] Joon-Mo Yang, Christopher Favazza, Ruimin Chen, Junjie Yao, Xin Cai, Konstantin Maslov, Qifa Zhou, K Kirk Shung, and Lihong V Wang. Simultaneous functional photoacoustic and ultrasonic endoscopy of internal organs in vivo. *Nature medicine*, 18(8):1297–1302, 2012.

[68] Moritz F Kircher, Adam De La Zerda, Jesse V Jokerst, Cristina L Zavaleta, Paul J Kempen, Erik Mittra, Ken Pitter, Ruimin Huang, Carl Campos, Frezghi Habte, et al. A brain tumor molecular imaging strategy using a new triple-modality mri-photoacoustic-raman nanoparticle. *Nature medicine*, 18(5):829–834, 2012.

[69] Lei Li, Liren Zhu, Li Lin, Konstantin Maslov, Junhui Shi, Liren Zhu, Ma Cheng, Junjie Yao, Lidai Wang, Ruiying Zhang, Wanyi Chen, and Lihong V. Wang. Single-impulse panoramic photoacoustic computed tomography of small-animal whole-body dynamics at high spatiotemporal resolution. *Nat. Biomed. Eng.*, 1:1–11, 2017.

[70] Minghua Xu and Lihong V. Wang. Photoacoustic imaging in biomedicine. *Rev. Sci. Instrum.*, 77:041101–1/22, 2006.

[71] Yuan Xu, Dazi Feng, and Lihong V. Wang. Exact frequency-domain reconstruction for thermoacoustic tomography–i planar geometry. *IEEE Trans. Med. Imag.*, 21:823–828, 2002.

[72] Huabei Jiang. *Photoacoustic Tomography.* CRC Press, Boca Ratan, 2015.

[73] Edward Z. Zhang, Boris Povazay, Jan Laufer, Aneesh Alex, Bernd Hofer, Barbara Pedley, Carl Glittenberg, Bradley Treeby, Ben Cox, Paul Beard, and Wolfgang Drexler. Multimodal photoacoustic and optical coherence tomography scanner using an all optical detection scheme for 3d morphological skin imaging. *Biomed. Opt. Express*, 2:2202–2215, 2011.

[74] Andrew A. Plumb, Nam Trung Huynh, Jamie Guggenheim, Edward Zhang, and Paul Beard. Rapid volumetric photoacoustic tomographic imaging with a fabry-perot ultrasound sensor depicts peripheral arteries and microvascular vasomotor responses to thermal stimuli. *Eur. Radiol.*, 28:1037–1045, 2018.

[75] G. Paultauf, R. Nuster, and P. Burgholzer. Characterization of integrating ultrasound detectors for photoacoustic tomography. *J. Appl. Phys.*, 105:102026/1–9, 2009.

[76] Peter Burgholzer, Christian Hofer, Gunther Paltauf, and Markus Haltmeier. Thermoacoustic tomography with integrating area and line detectors. *IEEE Trans. Ultrason., Ferroelectr., Freq. Control*, 52:1577–1583, 2005.

[77] Dario Livio Longo, Rachele Stefania, Silvio Aime, and Alexander Oraevsky. Melanin-based contrast agents for biomedical optoacoustic imaging and theranostic applications. *Int. J. Mol. Sci.*, 18:1719/1–20, 2017.

[78] M. I. Khan, T. Sun, and G. J. Diebold. Photoacoustic waves generated by absorption of laser radiation in optically thin layers. *J. Acoust. Soc. Am.*, 93:1417–1425, 1993.

[79] Lian Xiong, Jennifer M. Ruddock, and Gerald J. Diebold. Photoacoustic transients generated by laser irradiation of thin films. *Photoacoustics*, 3:60–63, 2015.

[80] G. J. Diebold, M. I. Khan, and S. M. Park. Photoacoustic signatures of particulate matter: optical production of acoustic monopole radiation. *Science*, 250:101–104, 1990.

[81] G. J. Diebold and P. J. Westervelt. The photoacoustic effect generated by a spherical droplet in a fluid. *J. Acoust. Soc. Am.*, 84:2245–2251, 1988. The numerator of Eq. 6 is missing a factor of $\hat{r}$. The transmission coefficient T following Eq. 30 in the text should have a 1 in the denominator, not a 2.

[82] M. I. Khan and G. J. Diebold. The photoacoustic effect generated by an isotropic solid sphere. *Ultrasonics*, 33:265–269, 1995.

[83] G. J. Diebold, A. C. Beveridge, and T. J. Hamilton. The photoacoustic effect generated by an incompressible sphere. *J. Acoust. Soc. Am.*, 112:1780–1786, 2002.

[84] M. I. Khan and G. J. Diebold. The photoacoustic effect generated by laser irradiation of an isotropic solid cylinder. *Ultrasonics*, 34:19–24, 1996.

[85] Yong Li, Hui Fang, Changjun Min, and Xiaocong Yuan. Analytic theory of photoacoustic wave generation from a spheroidal droplet. *Opt. Express*, 22:19953–19969, 2014.

[86] Yong Li, Hui Fang, Changjun Min, and Xiaocong Yuan. Simulating photoacoustic waves produced by individual biological particles with spheroidal wave functions. *Sci. Rep.*, 5:1–11, 2015.

[87] L. D. Landau and E. M. Lifshitz. *Fluid Dynamics*. Pergamon, New York, second edition, 1987. See Section 71.

[88] S. Temkin. *Elements of Acoustics*. John Wiley, New York, 1981.

[89] P. M. Morse. *Vibration and Sound*. Acoustical Society of America, New York, 1981.

[90] Eric M Strohm, Ivan Gorelikov, Naomi Matsuura, and Michael C Kolios. Acoustic and photoacoustic characterization of micron-sized perfluorocarbon emulsions. *J. Biomed. Opt.*, 17:096016/1–9, 2012.

[91] MI Khan, T Sun, and GJ Diebold. Photoacoustic waves generated by absorption of laser radiation in optically thin layers. *The Journal of the Acoustical Society of America*, 93(3):1417–1425, 1993.

[92] Lev Davidovich Landau, Evgenij M Lifšic, Evegnii Mikhailovich Lifshitz, Arnold Markovich Kosevich, and Lev Petrovich Pitaevskii. *Theory of elasticity: volume 7*, volume 7. Elsevier, 1986.

[93] A Karbach and P Hess. Photoacoustic signal in a cylindrical resonator: theory and laser experiments for ch4 and c2h6. *The Journal of chemical physics*, 84(6):2945–2952, 1986.

[94] L. M. Lyamshev. *Radiation Acoustics*. CRC Press, Boca Raton, 2004.

[95] Wenyu Bai and Gerald J Diebold. Photoacoustic effect generated by moving optical sources: Motion in three dimensions. *J. Acoust. Soc. Am.*, 142(6):3796–3803, 2017.

[96] F. V. Bunkin, Al. A. Kolomensky, and V. G. Mikhalevich. *Lasers in Acoustics*. Harwood Academic, Reading MA, 1991.

[97] Wenyu Bai and Gerald J. Diebold. Photoacoustic effect generated by moving optical sources: Motion in one dimension. *J. Appl. Phys.*, 119:124904, 2016.

[98] Wenyu Bai and Gerald J Diebold. Photoacoustic effect generated from an expanding spherical source. *Int. J. Thermophys.*, 39(2):1–6, 2018.

[99] L. M. Lyamshev and L. V. Sedov. Optical generation of sound in a liquid-thermal mechanism (review). *Physics Reviews (Soviet Scientific Reviews, Section A)*, 3:459–553, 1981.

[100] Jami L Johnson, Kasper van Wijk, James N Caron, and Miriam Timmerman. Gas-coupled laser acoustic detection as a non-contact line detector for photoacoustic and ultrasound imaging. *J. Opt.*, 18(2):024005, 2016.

[101] Saher M Maswadi, Bennett L Ibey, Caleb C Roth, Dmitri A Tsyboulski, Hope T Beier, Randolph D Glickman, and Alexander A Oraevsky. All-optical optoacoustic microscopy based on probe beam deflection technique. *Photoacoustics*, 4(3):91–101, 2016.

[102] Edward Z Zhang, Boris Povazay, Jan Laufer, Aneesh Alex, Bernd Hofer, Barbara Pedley, Carl Glittenberg, Bradley Treeby, Ben Cox, Paul Beard, et al. Multimodal photoacoustic and optical coherence tomography scanner using an all optical detection scheme for 3d morphological skin imaging. *Biomed. Opt. Express*, 2(8):2202–2215, 2011.

[103] Guenther Paltauf, Robert Nuster, and Peter Burgholzer. Characterization of integrating ultrasound detectors for photoacoustic tomography. *J. Appl. Phys.*, 105(10):102026, 2009.

[104] Richard Bouchard, Onur Sahin, and Stanislav Emelianov. Ultrasound-guided photoacoustic imaging: current state and future development. *IEEE transactions on ultrasonics, ferroelectrics, and frequency control*, 61(3):450–466, 2014.

[105] Robert A Kruger, Pingyu Liu, Yuncai "Richard" Fang, and C Robert Appledorn. Photoacoustic ultrasound (paus)—reconstruction tomography. *Medical physics*, 22(10):1605–1609, 1995.

[106] A Mandelis. Progress in photothermal and photoacoustic science and technology. *Principles and Perspectives of Photothermal and Photoacoustic Phenomena and Life and Earth Science*, 1997.

[107] Ltd APC International. *Piezoelectric ceramics: principles and applications*. APC International, 2002.

[108] Jr. Ronald A. Barnes, Saher Maswade, Randolph Glickman, and Mehdi Shadaram. Probe beam deflection technique as acoustic emission directionality sensor with photoacoustic emission source. *Appl. Opt.*, 53:511–519, 2014.

[109] Bao-Yu Hsieh, Sung-Liang Chen, Tao Ling, L Jay Guo, and Pai-Chi Li. All-optical scanhead for ultrasound and photoacoustic imaging—-imaging mode switching by dichroic filtering. *Photoacoustics*, 2(1):39–46, 2014.

[110] R. M. Bracewell. *The Fourier Transform and Its Applications.* McGraw-Hill, New York, 1965.

[111] Thomas J Asaki, R Chartrand, KR Vixie, and B Wohlberg. Abel inversion using total-variation regularization. *Inverse Probl.*, 21(6):1895, 2005.

[112] Thomas J. Asaki, Patrick R. Campbell, Rick Chartrand, Collin E. Powell, Kevin R. Bixie, and Brendt E. Wohlberg. Abel inversion using total variation regularization: applications. *Inverse Probl. Sci. Eng.*, 14:873–885, 2006.

[113] Georg Pretzler. A new method for numerical abel-inversion. *Z. Natur.*, 46:639–641, 1991.

[114] L. Montgomery Smith and Dennis R. Keefer. Abel inversion using transform techniques. *J. Quant. Spectrosc. Radiat. Transf.*, 39:367–373, 1988.

[115] Pablo A. Vicharelli and Walter P. Lapaatovich. Iterative method for computing the inverse abel transform. *Appl. Phys. Lett.*, 50:557–559, 1987.

[116] Gustavo A. Garcia and Laurent Nahon. Two-dimensional charged particle image inversion using a polar basis function expansion. *Rev. Sci. Instrum.*, 75:4989–4996, 2004.

[117] S. Temkin. *Elements of Acoustics.* John Wiley, New York, 1981.

[118] Robert Tibshirani. Regression shrinkage and selection via the lasso. *J. R. Stat. Soc. Series B Stat. Methodol.*, 58:267–288, 1996.

[119] Jerome Friedman, Trevor Hastie, and Rob Tibshirani. Regularization paths for generalized linear models via coordinate descent. *J. Stat. Softw.*, 33(1):1, 2010.

[120] Hui Zou, Trevor Hastie, and Robert Tibshirani. On the "degrees of freedom" of the lasso. *Ann. Stat.*, 35(5):2173–2192, 2007.

[121] Ryan J Tibshirani and Jonathan Taylor. Degrees of freedom in lasso problems. *Ann. Stat.*, 40(2):1198–1232, 2012.

[122] Martin J Wainwright. *High-dimensional statistics: A non-asymptotic viewpoint*, volume 48. Cambridge University Press, 2019.

[123] Ben C Platt and Roland Shack. History and principles of shack-hartmann wavefront sensing, 2001.

[124] Daniel R Neal, James Copland, and David A Neal. Shack-hartmann wavefront sensor precision and accuracy. In *Advanced Characterization Techniques for Optical, Semiconductor, and Data Storage Components*, volume 4779, pages 148–160. SPIE, 2002.

[125] Xueding Wang, Yongjiang Pang, Geng Ku, Xueyi Xie, George Stoica, and Lihong V Wang. Noninvasive laser-induced photoacoustic tomography for structural and functional in vivo imaging of the brain. *Nature biotechnology*, 21(7):803–806, 2003.

[126] Shuai Na, Jonathan J Russin, Li Lin, Xiaoyun Yuan, Peng Hu, Kay B Jann, Lirong Yan, Konstantin Maslov, Junhui Shi, Danny J Wang, et al. Massively parallel functional photoacoustic computed tomography of the human brain. *Nature Biomedical Engineering*, 6(5):584–592, 2022.

[127] Emmanuel J Candes and David L Donoho. Recovering edges in ill-posed inverse problems: Optimality of curvelet frames. *The Annals of Statistics*, 30(3):784–842, 2002.

[128] David L Donoho. Compressed sensing. *IEEE Transactions on information theory*, 52(4):1289–1306, 2006.

[129] David L Donoho, Michael Elad, and Vladimir N Temlyakov. Stable recovery of sparse overcomplete representations in the presence of noise. *IEEE Transactions on information theory*, 52(1):6–18, 2005.

[130] Kweku Abraham and Richard Nickl. On statistical calderón problems. *Mathematical Statistics and Learning*, 2(2):165–216, 2020.

[131] Richard Bellman. Dynamic programming. *Princeton University Press*, 1957.

[132] Hatef Monajemi, Sina Jafarpour, Matan Gavish, Stat 330/CME 362 Collaboration, David L Donoho, Sivaram Ambikasaran, Sergio Bacallado, Dinesh Bharadia, Yuxin Chen, Young Choi, et al. Deterministic matrices matching the compressed sensing phase transitions of gaussian random matrices. *Proceedings of the National Academy of Sciences*, 110(4):1181–1186, 2013.

[133] Thibault Lesieur, Florent Krzakala, and Lenka Zdeborová. Mmse of probabilistic low-rank matrix estimation: Universality with respect to the output channel. In *2015 53rd Annual Allerton Conference on Communication, Control, and Computing (Allerton)*, pages 680–687. IEEE, 2015.

[134] Jean Barbier, Florent Krzakala, Nicolas Macris, Léo Miolane, and Lenka Zdeborová. Optimal errors and phase transitions in high-dimensional generalized

linear models. *Proceedings of the National Academy of Sciences*, 116(12):5451–5460, 2019.

[135] Thibault Lesieur, Florent Krzakala, and Lenka Zdeborová. Phase transitions in sparse pca. In *2015 IEEE International Symposium on Information Theory (ISIT)*, pages 1635–1639. IEEE, 2015.

[136] Lenka Zdeborová and Florent Krzakała. Phase transitions in the coloring of random graphs. *Physical Review E*, 76(3):031131, 2007.

[137] Aurelien Decelle, Florent Krzakala, Cristopher Moore, and Lenka Zdeborová. Inference and phase transitions in the detection of modules in sparse networks. *Physical Review Letters*, 107(6):065701, 2011.

[138] Yoshiyuki Kabashima, Florent Krzakala, Marc Mézard, Ayaka Sakata, and Lenka Zdeborová. Phase transitions and sample complexity in bayes-optimal matrix factorization. *IEEE Transactions on information theory*, 62(7):4228–4265, 2016.

[139] Michel Talagrand. *Mean field models for spin glasses: Volume I: Basic examples*, volume 54. Springer Science & Business Media, 2010.

[140] Erwin Bolthausen and Alain-Sol Sznitman. *Ten lectures on random media*, volume 32. Springer Science & Business Media, 2002.

[141] Michel Ledoux. *The concentration of measure phenomenon*. Number 89. American Mathematical Soc., 2001.

[142] Hans-Otto Georgii. Gibbs measures and phase transitions. In *Gibbs Measures and Phase Transitions*. de Gruyter, 2011.

[143] Madhu Advani and Surya Ganguli. Statistical mechanics of optimal convex inference in high dimensions. *Physical Review X*, 6(3):031034, 2016.

[144] Simon Foucart and Holger Rauhut. An invitation to compressive sensing. In *A mathematical introduction to compressive sensing*, pages 1–39. Springer, 2013.

[145] Michael Lustig, David Donoho, and John M Pauly. Sparse mri: The application of compressed sensing for rapid mr imaging. *Magnetic Resonance in Medicine: An Official Journal of the International Society for Magnetic Resonance in Medicine*, 58(6):1182–1195, 2007.

[146] Emmanuel J Candès and Pragya Sur. The phase transition for the existence of the maximum likelihood estimate in high-dimensional logistic regression. *The Annals of Statistics*, 48(1):27–42, 2020.

[147] Pragya Sur and Emmanuel J Candès. A modern maximum-likelihood theory for high-dimensional logistic regression. *Proceedings of the National Academy of Sciences*, 116(29):14516–14525, 2019.

[148] Qian Zhao, Pragya Sur, and Emmanuel J Candes. The asymptotic distribution of the mle in high-dimensional logistic models: Arbitrary covariance. *Bernoulli*, 28(3):1835–1861, 2022.

[149] Bradley Efron. Large-scale simultaneous hypothesis testing: the choice of a null hypothesis. *Journal of the American Statistical Association*, 99(465):96–104, 2004.

[150] David Donoho and Jiashun Jin. Higher criticism for detecting sparse heterogeneous mixtures. *The Annals of Statistics*, 32(3):962–994, 2004.

[151] David Donoho and Jiashun Jin. Higher criticism for large-scale inference, especially for rare and weak effects. *Statistical Science*, 30(1):1–25, 2015.

[152] Jiashun Jin and Zheng Tracy Ke. Rare and weak effects in large-scale inference: methods and phase diagrams. *Statistica Sinica*, pages 1–34, 2016.

[153] Peter Hall and Jiashun Jin. Innovated higher criticism for detecting sparse signals in correlated noise. *The Annals of Statistics*, 38(3):1686–1732, 2010.

[154] Scott Shaobing Chen, David L Donoho, and Michael A Saunders. Atomic decomposition by basis pursuit. *SIAM review*, 43(1):129–159, 2001.

[155] Jerome Friedman, Trevor Hastie, and Robert Tibshirani. A note on the group lasso and a sparse group lasso. *arXiv preprint arXiv:1001.0736*, 2010.

[156] Robert Tibshirani, Michael Saunders, Saharon Rosset, Ji Zhu, and Keith Knight. Sparsity and smoothness via the fused lasso. *Journal of the Royal Statistical Society: Series B (Statistical Methodology)*, 67(1):91–108, 2005.

[157] Jerome Friedman, Trevor Hastie, and Robert Tibshirani. Sparse inverse covariance estimation with the graphical lasso. *Biostatistics*, 9(3):432–441, 2008.

[158] Hui Zou. The adaptive lasso and its oracle properties. *Journal of the American statistical association*, 101(476):1418–1429, 2006.

[159] Alexandre Belloni, Victor Chernozhukov, and Lie Wang. Square-root lasso: pivotal recovery of sparse signals via conic programming. *Biometrika*, 98(4):791–806, 2011.

[160] Emmanuel Candes and Benjamin Recht. Exact matrix completion via convex optimization. *Communications of the ACM*, 55(6):111–119, 2012.

[161] Jian-Feng Cai, Emmanuel J Candès, and Zuowei Shen. A singular value thresholding algorithm for matrix completion. *SIAM Journal on optimization*, 20(4):1956–1982, 2010.

[162] Emmanuel J Candès, Xiaodong Li, Yi Ma, and John Wright. Robust principal component analysis? *Journal of the ACM (JACM)*, 58(3):1–37, 2011.

[163] Leonid I Rudin, Stanley Osher, and Emad Fatemi. Nonlinear total variation based noise removal algorithms. *Physica D: nonlinear phenomena*, 60(1-4):259–268, 1992.

[164] Robert Acar and Curtis R Vogel. Analysis of bounded variation penalty methods for ill-posed problems. *Inverse problems*, 10(6):1217, 1994.

[165] Martin Burger and Stanley Osher. A guide to the tv zoo. In *Level set and PDE based reconstruction methods in imaging*, pages 1–70. Springer, 2013.

[166] Emmanuel J Candès, Justin Romberg, and Terence Tao. Robust uncertainty principles: Exact signal reconstruction from highly incomplete frequency information. *IEEE Transactions on information theory*, 52(2):489–509, 2006.

[167] David L Donoho, Iain M Johnstone, Gérard Kerkyacharian, and Dominique Picard. Wavelet shrinkage: asymptopia? *Journal of the Royal Statistical Society: Series B (Methodological)*, 57(2):301–337, 1995.

[168] David L Donoho and Iain M Johnstone. Adapting to unknown smoothness via wavelet shrinkage. *Journal of the american statistical association*, 90(432):1200–1224, 1995.

[169] Gilles Aubert, Pierre Kornprobst, and Giles Aubert. *Mathematical problems in image processing: partial differential equations and the calculus of variations*, volume 147. Springer, 2006.

[170] Gerhard Winkler. *Image analysis, random fields and Markov chain Monte Carlo methods: a mathematical introduction*, volume 27. Springer Science & Business Media, 2003.

[171] Mingqiang Zhu and Tony Chan. An efficient primal-dual hybrid gradient algorithm for total variation image restoration. *Ucla Cam Report*, 34:8–34, 2008.

[172] Antonio Marquina and Stanley J Osher. Image super-resolution by tv-regularization and bregman iteration. *Journal of Scientific Computing*, 37(3):367–382, 2008.

[173] Martin Benning, Lynn Gladden, Daniel Holland, Carola-Bibiane Schönlieb, and Tuomo Valkonen. Phase reconstruction from velocity-encoded mri measurements–a survey of sparsity-promoting variational approaches. *Journal of Magnetic Resonance*, 238:26–43, 2014.

[174] Gordon Wetzstein. Stanford ee367 computational imaging 2022. *Stanford*, 2022.

[175] Charles Bouman and Ken Sauer. A generalized gaussian image model for edge-preserving map estimation. *IEEE Transactions on image processing*, 2(3):296–310, 1993.

[176] Dorit S Hochbaum. An efficient algorithm for image segmentation, markov random fields and related problems. *Journal of the ACM (JACM)*, 48(4):686–701, 2001.

[177] Felix Abramovich and Bernard W Silverman. Wavelet decomposition approaches to statistical inverse problems. *Biometrika*, 85(1):115–129, 1998.

[178] David L Donoho. Nonlinear solution of linear inverse problems by wavelet–vaguelette decomposition. *Applied and computational harmonic analysis*, 2(2):101–126, 1995.

[179] Yazhen Wang. Minimax estimation via wavelets for indirect long-memory data. *Journal of statistical planning and inference*, 64(1):45–55, 1997.

[180] Jianqing Fan and Ja-Yong Koo. Wavelet deconvolution. *IEEE transactions on information theory*, 48(3):734–747, 2002.

[181] Iain M Johnstone, Gérard Kerkyacharian, Dominique Picard, and Marc Raimondo. Wavelet deconvolution in a periodic setting. *Journal of the Royal Statistical Society: Series B (Statistical Methodology)*, 66(3):547–573, 2004.

[182] Iain M Johnstone and Marc Raimondo. Periodic boxcar deconvolution and diophantine approximation. *The Annals of Statistics*, 32(5):1781–1804, 2004.

[183] Eric D Kolaczyk. A wavelet shrinkage approach to tomographic image reconstruction. *Journal of the American Statistical Association*, 91(435):1079–1090, 1996.

[184] Iain M Johnstone. Wavelet shrinkage for correlated data and inverse problems: adaptivity results. *Statistica Sinica*, pages 51–83, 1999.

[185] Iain M Johnstone and Bernard W Silverman. Discretization effects in statistical inverse problems. *Journal of complexity*, 7(1):1–34, 1991.

[186] Daniel D Lee and H Sebastian Seung. Learning the parts of objects by non-negative matrix factorization. *Nature*, 401(6755):788–791, 1999.

[187] Karl Pearson. Liii. on lines and planes of closest fit to systems of points in space. *The London, Edinburgh, and Dublin philosophical magazine and journal of science*, 2(11):559–572, 1901.

[188] Diederik P Kingma and Max Welling. Auto-encoding variational bayes. *arXiv preprint arXiv:1312.6114*, 2013.

[189] Ian Goodfellow, Jean Pouget-Abadie, Mehdi Mirza, Bing Xu, David Warde-Farley, Sherjil Ozair, Aaron Courville, and Yoshua Bengio. Generative adversarial nets. *Advances in neural information processing systems*, 27, 2014.

[190] Dimitri Bertsekas, Angelia Nedic, and Asuman Ozdaglar. *Convex analysis and optimization*, volume 1. Athena Scientific, 2003.

[191] Stephen Boyd, Stephen P Boyd, and Lieven Vandenberghe. *Convex optimization*. Cambridge university press, 2004.

[192] Sébastien Bubeck et al. Convex optimization: Algorithms and complexity. *Foundations and Trends® in Machine Learning*, 8(3-4):231–357, 2015.

[193] Yurii E Nesterov. A method for solving the convex programming problem with convergence rate o (1/kˆ 2). In *Dokl. akad. nauk Sssr*, volume 269, pages 543–547, 1983.

[194] Inderjit S Dhillon and Joel A Tropp. Matrix nearness problems with bregman divergences. *SIAM Journal on Matrix Analysis and Applications*, 29(4):1120–1146, 2008.

[195] Amir Beck and Marc Teboulle. A fast iterative shrinkage-thresholding algorithm for linear inverse problems. *SIAM journal on imaging sciences*, 2(1):183–202, 2009.

[196] Amir Beck and Marc Teboulle. Fast gradient-based algorithms for constrained total variation image denoising and deblurring problems. *IEEE transactions on image processing*, 18(11):2419–2434, 2009.

[197] Antonin Chambolle and Thomas Pock. A first-order primal-dual algorithm for convex problems with applications to imaging. *Journal of mathematical imaging and vision*, 40(1):120–145, 2011.

[198] Andrey Nikolayevich Tikhonov. On the stability of inverse problems. In *Dokl. Akad. Nauk SSSR*, volume 39, pages 195–198, 1943.

[199] Andrei Nikolajevits Tihonov. Solution of incorrectly formulated problems and the regularization method. *Soviet Math.*, 4:1035–1038, 1963.

[200] Andre Nikolaevich Tikhonov and Vasilii Iakovlevich Arsenin. *Solutions of Ill-posed Problems: Andrey N. Tikhonov and Vasiliy Y. Arsenin. Translation Editor Fritz John*. Winston & Sons, 1977.

[201] Arthur E Hoerl and Robert W Kennard. Ridge regression: Biased estimation for nonorthogonal problems. *Technometrics*, 12(1):55–67, 1970.

[202] Tom Goldstein and Stanley Osher. The split bregman method for l1-regularized problems. *SIAM journal on imaging sciences*, 2(2):323–343, 2009.

[203] Wotao Yin, Stanley Osher, Donald Goldfarb, and Jerome Darbon. Bregman iterative algorithms for \ell_1-minimization with applications to compressed sensing. *SIAM Journal on Imaging sciences*, 1(1):143–168, 2008.

[204] Ryan J Tibshirani. The lasso problem and uniqueness. *Electronic Journal of statistics*, 7:1456–1490, 2013.

[205] Sara A Van de Geer. High-dimensional generalized linear models and the lasso. *The Annals of Statistics*, 36(2):614–645, 2008.

[206] Magnus R Hestenes. Multiplier and gradient methods. *Journal of optimization theory and applications*, 4(5):303–320, 1969.

[207] Stephen Boyd, Neal Parikh, Eric Chu, Borja Peleato, Jonathan Eckstein, et al. Distributed optimization and statistical learning via the alternating direction method of multipliers. *Foundations and Trends® in Machine learning*, 3(1):1–122, 2011.

[208] Amir A Amini, Terry E Weymouth, and Ramesh C Jain. Using dynamic programming for solving variational problems in vision. *IEEE Transactions on pattern analysis and machine intelligence*, 12(9):855–867, 1990.

[209] Stuart Geman and Donald Geman. Stochastic relaxation, gibbs distributions, and the bayesian restoration of images. *IEEE Transactions on pattern analysis and machine intelligence*, (6):721–741, 1984.

[210] Martin J Wainwright, Tommi S Jaakkola, and Alan S Willsky. Map estimation via agreement on trees: message-passing and linear programming. *IEEE transactions on information theory*, 51(11):3697–3717, 2005.

[211] Stuart Geman and Christine Graffigne. Markov random field image models and their applications to computer vision. In *Proceedings of the international congress of mathematicians*, volume 1, page 2. Berkeley, CA, 1986.

[212] Kurt Hornik. Approximation capabilities of multilayer feedforward networks. *Neural networks*, 4(2):251–257, 1991.

[213] Yann LeCun, Yoshua Bengio, and Geoffrey Hinton. Deep learning. *nature*, 521(7553):436–444, 2015.

[214] Singanallur V Venkatakrishnan, Charles A Bouman, and Brendt Wohlberg. Plug-and-play priors for model based reconstruction. In *2013 IEEE Global Conference on Signal and Information Processing*, pages 945–948. IEEE, 2013.

[215] Stanley H Chan, Xiran Wang, and Omar A Elgendy. Plug-and-play admm for image restoration: Fixed-point convergence and applications. *IEEE Transactions on Computational Imaging*, 3(1):84–98, 2016.

[216] Yaniv Romano, Michael Elad, and Peyman Milanfar. The little engine that could: Regularization by denoising (red). *SIAM Journal on Imaging Sciences*, 10(4):1804–1844, 2017.

[217] Diederik P Kingma and Jimmy Ba. Adam: A method for stochastic optimization. *arXiv preprint arXiv:1412.6980*, 2014.

[218] Kai Zhang, Wangmeng Zuo, Yunjin Chen, Deyu Meng, and Lei Zhang. Beyond a gaussian denoiser: Residual learning of deep cnn for image denoising. *IEEE transactions on image processing*, 26(7):3142–3155, 2017.

[219] Bahjat Kawar, Gregory Vaksman, and Michael Elad. Snips: Solving noisy inverse problems stochastically. *Advances in Neural Information Processing Systems*, 34:21757–21769, 2021.

[220] Zahra Kadkhodaie and Eero Simoncelli. Stochastic solutions for linear inverse problems using the prior implicit in a denoiser. *Advances in Neural Information Processing Systems*, 34:13242–13254, 2021.

[221] Jérôme Darbon and Stanley Osher. Algorithms for overcoming the curse of dimensionality for certain hamilton–jacobi equations arising in control theory and elsewhere. *Research in the Mathematical Sciences*, 3(1):1–26, 2016.

[222] Yat Tin Chow, Jérôme Darbon, Stanley Osher, and Wotao Yin. Algorithm for overcoming the curse of dimensionality for state-dependent hamilton-jacobi equations. *Journal of Computational Physics*, 387:376–409, 2019.

[223] Jérôme Darbon. On convex finite-dimensional variational methods in imaging sciences and hamilton–jacobi equations. *SIAM Journal on Imaging Sciences*, 8(4):2268–2293, 2015.

[224] Giuseppe Carleo, Ignacio Cirac, Kyle Cranmer, Laurent Daudet, Maria Schuld, Naftali Tishby, Leslie Vogt-Maranto, and Lenka Zdeborová. Machine learning and the physical sciences. *Reviews of Modern Physics*, 91(4):045002, 2019.

[225] Gordon Wetzstein, Aydogan Ozcan, Sylvain Gigan, Shanhui Fan, Dirk Englund, Marin Soljačić, Cornelia Denz, David AB Miller, and Demetri Psaltis. Inference in artificial intelligence with deep optics and photonics. *Nature*, 588(7836):39–47, 2020.

[226] Gökcen Eraslan, Žiga Avsec, Julien Gagneur, and Fabian J Theis. Deep learning: new computational modelling techniques for genomics. *Nature Reviews Genetics*, 20(7):389–403, 2019.

[227] Kenji Suzuki. Overview of deep learning in medical imaging. *Radiological physics and technology*, 10(3):257–273, 2017.

[228] Linfeng Zhang, Jiequn Han, Han Wang, Roberto Car, and EJPRL Weinan. Deep potential molecular dynamics: a scalable model with the accuracy of quantum mechanics. *Physical review letters*, 120(14):143001, 2018.

[229] Jong Chul Ye, Yoseob Han, and Eunju Cha. Deep convolutional framelets: A general deep learning framework for inverse problems. *SIAM Journal on Imaging Sciences*, 11(2):991–1048, 2018.

[230] Davis Gilton, Greg Ongie, and Rebecca Willett. Neumann networks for linear inverse problems in imaging. *IEEE Transactions on Computational Imaging*, 6:328–343, 2019.

[231] Kyong Hwan Jin, Michael T McCann, Emmanuel Froustey, and Michael Unser. Deep convolutional neural network for inverse problems in imaging. *IEEE Transactions on Image Processing*, 26(9):4509–4522, 2017.

[232] Davis Gilton, Gregory Ongie, and Rebecca Willett. Deep equilibrium architectures for inverse problems in imaging. *IEEE Transactions on Computational Imaging*, 7:1123–1133, 2021.

[233] Bo Zhu, Jeremiah Z Liu, Stephen F Cauley, Bruce R Rosen, and Matthew S Rosen. Image reconstruction by domain-transform manifold learning. *Nature*, 555(7697):487–492, 2018.

[234] Gregory Ongie, Ajil Jalal, Christopher A Metzler, Richard G Baraniuk, Alexandros G Dimakis, and Rebecca Willett. Deep learning techniques for inverse problems in imaging. *IEEE Journal on Selected Areas in Information Theory*, 1(1):39–56, 2020.

[235] Simon Arridge, Peter Maass, Ozan Öktem, and Carola-Bibiane Schönlieb. Solving inverse problems using data-driven models. *Acta Numerica*, 28:1–174, 2019.

[236] Stephan Antholzer, Markus Haltmeier, Robert Nuster, and Johannes Schwab. Photoacoustic image reconstruction via deep learning. In *Photons Plus Ultrasound: Imaging and Sensing 2018*, volume 10494, pages 433–442. SPIE, 2018.

[237] Neda Davoudi, Xosé Luís Deán-Ben, and Daniel Razansky. Deep learning optoacoustic tomography with sparse data. *Nature Machine Intelligence*, 1(10):453–460, 2019.

[238] Yuehaw Khoo, Jianfeng Lu, and Lexing Ying. Solving parametric pde problems with artificial neural networks. *European Journal of Applied Mathematics*, 32(3):421–435, 2021.

[239] Maziar Raissi, Paris Perdikaris, and George E Karniadakis. Physics-informed neural networks: A deep learning framework for solving forward and inverse problems involving nonlinear partial differential equations. *Journal of Computational physics*, 378:686–707, 2019.

[240] Ashish Bora, Ajil Jalal, Eric Price, and Alexandros G Dimakis. Compressed sensing using generative models. In *International Conference on Machine Learning*, pages 537–546. PMLR, 2017.

[241] Ajil Jalal, Sushrut Karmalkar, Alexandros G Dimakis, and Eric Price. Instance-optimal compressed sensing via posterior sampling. *arXiv preprint arXiv:2106.11438*, 2021.

[242] Ajil Jalal, Marius Arvinte, Giannis Daras, Eric Price, Alexandros G Dimakis, and Jon Tamir. Robust compressed sensing mri with deep generative priors. *Advances in Neural Information Processing Systems*, 34:14938–14954, 2021.

[243] Ajil Jalal, Liu Liu, Alexandros G Dimakis, and Constantine Caramanis. Robust compressed sensing using generative models. *Advances in Neural Information Processing Systems*, 33:713–727, 2020.

[244] Jakub M Tomczak. Why deep generative modeling? In *Deep Generative Modeling*, pages 1–12. Springer, 2022.

[245] Laurent Dinh, David Krueger, and Yoshua Bengio. Nice: Non-linear independent components estimation. *arXiv preprint arXiv:1410.8516*, 2014.

[246] Durk P Kingma and Prafulla Dhariwal. Glow: Generative flow with invertible 1x1 convolutions. *Advances in neural information processing systems*, 31, 2018.

[247] Yang Song and Stefano Ermon. Generative modeling by estimating gradients of the data distribution. *Advances in Neural Information Processing Systems*, 32, 2019.

[248] Yang Song and Stefano Ermon. Improved techniques for training score-based generative models. *Advances in neural information processing systems*, 33:12438–12448, 2020.

[249] Yang Song, Jascha Sohl-Dickstein, Diederik P Kingma, Abhishek Kumar, Stefano Ermon, and Ben Poole. Score-based generative modeling through stochastic differential equations. *arXiv preprint arXiv:2011.13456*, 2020.

[250] Yang Song, Liyue Shen, Lei Xing, and Stefano Ermon. Solving inverse problems in medical imaging with score-based generative models. *arXiv preprint arXiv:2111.08005*, 2021.

[251] Muhammad Asim, Max Daniels, Oscar Leong, Ali Ahmed, and Paul Hand. Invertible generative models for inverse problems: mitigating representation error and dataset bias. In *International Conference on Machine Learning*, pages 399–409. PMLR, 2020.

[252] Masoumeh Dashti and Andrew M Stuart. The bayesian approach to inverse problems. In *Handbook of uncertainty quantification*, pages 311–428. Springer, 2017.

[253] Shai Ben-David, John Blitzer, Koby Crammer, Alex Kulesza, Fernando Pereira, and Jennifer Wortman Vaughan. A theory of learning from different domains. *Machine learning*, 79(1):151–175, 2010.

[254] Michael Mitzenmacher and Eli Upfal. *Probability and computing: Randomization and probabilistic techniques in algorithms and data analysis*. Cambridge university press, 2017.

[255] Hidetoshi Shimodaira. Improving predictive inference under covariate shift by weighting the log-likelihood function. *Journal of statistical planning and inference*, 90(2):227–244, 2000.

[256] Samuel H Rudy, Steven L Brunton, Joshua L Proctor, and J Nathan Kutz. Data-driven discovery of partial differential equations. *Science advances*, 3(4):e1602614, 2017.

[257] Bing Yu et al. The deep ritz method: a deep learning-based numerical algorithm for solving variational problems. *Communications in Mathematics and Statistics*, 6(1):1–12, 2018.

[258] Aaron T Kuan, Jasper S Phelps, Logan A Thomas, Tri M Nguyen, Julie Han, Chiao-Lin Chen, Anthony W Azevedo, John C Tuthill, Jan Funke, Peter Cloetens, et al. Dense neuronal reconstruction through x-ray holographic nano-tomography. *Nature neuroscience*, 23(12):1637–1643, 2020.

[259] M Marvin Seibert, Tomas Ekeberg, Filipe RNC Maia, Martin Svenda, Jakob Andreasson, Olof Jönsson, Duško Odić, Bianca Iwan, Andrea Rocker, Daniel Westphal, et al. Single mimivirus particles intercepted and imaged with an x-ray laser. *Nature*, 470(7332):78–81, 2011.

[260] SW Wilkins, T Ei Gureyev, D Gao, A Pogany, and AW Stevenson. Phase-contrast imaging using polychromatic hard x-rays. *Nature*, 384(6607):335–338, 1996.

[261] Peter Cloetens, W Ludwig, J Baruchel, D Van Dyck, J Van Landuyt, JP Guigay, and Ma Schlenker. Holotomography: Quantitative phase tomography with micrometer resolution using hard synchrotron radiation x rays. *Applied physics letters*, 75(19):2912–2914, 1999.

[262] Peter Cloetens, Raymond Barrett, José Baruchel, Jean-Pierre Guigay, and Michel Schlenker. Phase objects in synchrotron radiation hard x-ray imaging. *Journal of physics D: applied physics*, 29(1):133, 1996.

[263] John Maxwell Cowley. Diffraction physics. 1995.

[264] M Born and E Wolf. Principle of optics. 1991.

[265] Fulvia Arfelli, M Assante, V Bonvicini, A Bravin, Giovanni Cantatore, Edoardo Castelli, L Dalla Palma, M Di Michiel, Renata Longo, A Olivo, et al. Low-dose phase contrast x-ray medical imaging. *Physics in Medicine & Biology*, 43(10):2845, 1998.

[266] Andrew Pogany, D Gao, and SW Wilkins. Contrast and resolution in imaging with a microfocus x-ray source. *Review of Scientific Instruments*, 68(7):2774–2782, 1997.

[267] Guohua Cao, Theron J Hamilton, Christoph Rose-Petruck, and Gerald J Diebold. X-ray phase-contrast imaging: transmission functions separable in cartesian coordinates. *JOSA A*, 24(4):1201–1208, 2007.

[268] Guohua Cao, Theron Hamilton, Christopher M Laperle, Christoph Rose-Petruck, and Gerald J Diebold. X-ray phase contrast imaging: Transmission functions separable in cylindrical coordinates. *Journal of applied physics*, 105(10):102002, 2009.

[269] Han Wen, Eric E Bennett, Monica M Hegedus, and Stanislas Rapacchi. Fourier x-ray scattering radiography yields bone structural information. *Radiology*, 251(3):910, 2009.

[270] Han Wen, Eric E Bennett, Monica M Hegedus, and Stefanie C Carroll. Spatial harmonic imaging of x-ray scattering—initial results. *IEEE transactions on medical imaging*, 27(8):997–1002, 2008.

[271] Yanan Liu, Brian Ahr, Alexander Linkin, Gerald J Diebold, and Christoph Rose-Petruck. X-ray spatial harmonic imaging of phase objects. *Optics letters*, 36(12):2209–2211, 2011.

[272] Ronald Newbold Bracewell and Ronald N Bracewell. *The Fourier transform and its applications*, volume 31999. McGraw-Hill New York, 1986.

[273] Theron J Hamilton, Claude Bailat, Stephan Gehring, Christopher M Laperle, Jack Wands, Christoph Rose-Petruck, and Gerald J Diebold. X-ray elastography: Modification of x-ray phase contrast images using ultrasonic radiation pressure. *Journal of Applied Physics*, 105(10):102001, 2009.

[274] Binbin Wu, Yanan Liu, Christoph Rose-Petruck, and Gerald J Diebold. X-ray spatial frequency heterodyne imaging. *Applied Physics Letters*, 100(6):061110, 2012.

[275] Colin Crosland Goodyear. *Signals and Information*. Wiley-Interscience, 1971.

[276] KA Nugent, TE Gureyev, DF Cookson, D Paganin, and ZNMN Barnea. Quantitative phase imaging using hard x rays. *Physical review letters*, 77(14):2961, 1996.

[277] David Paganin, Sheridan C Mayo, Tim E Gureyev, Peter R Miller, and Steve W Wilkins. Simultaneous phase and amplitude extraction from a single defocused image of a homogeneous object. *Journal of microscopy*, 206(1):33–40, 2002.

[278] Jianwei Miao, Pambos Charalambous, Janos Kirz, and David Sayre. Extending the methodology of x-ray crystallography to allow imaging of micrometre-sized non-crystalline specimens. *Nature*, 400(6742):342–344, 1999.

[279] Jianwei Miao, Tetsuya Ishikawa, Ian K Robinson, and Margaret M Murnane. Beyond crystallography: Diffractive imaging using coherent x-ray light sources. *Science*, 348(6234):530–535, 2015.

[280] Jie Yang, Markus Guehr, Xiaozhe Shen, Renkai Li, Theodore Vecchione, Ryan Coffee, Jeff Corbett, Alan Fry, Nick Hartmann, Carsten Hast, et al. Diffractive imaging of coherent nuclear motion in isolated molecules. *Physical review letters*, 117(15):153002, 2016.

[281] MP Minitti, JM Budarz, Adam Kirrander, JS Robinson, Daniel Ratner, TJ Lane, D Zhu, JM Glownia, M Kozina, HT Lemke, et al. Imaging molecular motion: Femtosecond x-ray scattering of an electrocyclic chemical reaction. *Physical review letters*, 114(25):255501, 2015.

[282] Brian Stankus, Haiwang Yong, Nikola Zotev, Jennifer M Ruddock, Darren Bellshaw, Thomas J Lane, Mengning Liang, Sébastien Boutet, Sergio Carbajo, Joseph S Robinson, et al. Ultrafast x-ray scattering reveals vibrational coherence following rydberg excitation. *Nature chemistry*, 11(8):716–721, 2019.

[283] N Hartmann, G Hartmann, R Heider, MS Wagner, M Ilchen, J Buck, AO Lindahl, C Benko, J Grünert, J Krzywinski, et al. Attosecond time–energy structure of x-ray free-electron laser pulses. *Nature Photonics*, 12(4):215–220, 2018.

[284] David A Barmherzig, Ju Sun, Po-Nan Li, Thomas Joseph Lane, and Emmanuel J Candes. Holographic phase retrieval and reference design. *Inverse Problems*, 35(9):094001, 2019.

[285] D Russell Luke. Relaxed averaged alternating reflections for diffraction imaging. *Inverse problems*, 21(1):37, 2004.

[286] Zaiwen Wen, Chao Yang, Xin Liu, and Stefano Marchesini. Alternating direction methods for classical and ptychographic phase retrieval. *Inverse Problems*, 28(11):115010, 2012.

[287] James R Fienup. Reconstruction of an object from the modulus of its fourier transform. *Optics letters*, 3(1):27–29, 1978.

[288] Emmanuel J Candes, Xiaodong Li, and Mahdi Soltanolkotabi. Phase retrieval from coded diffraction patterns. *Applied and Computational Harmonic Analysis*, 39(2):277–299, 2015.

[289] Emmanuel J Candes, Yonina C Eldar, Thomas Strohmer, and Vladislav Voroninski. Phase retrieval via matrix completion. *SIAM review*, 57(2):225–251, 2015.

[290] Emmanuel J Candes, Thomas Strohmer, and Vladislav Voroninski. Phaselift: Exact and stable signal recovery from magnitude measurements via convex programming. *Communications on Pure and Applied Mathematics*, 66(8):1241–1274, 2013.

[291] Tom Goldstein and Christoph Studer. Phasemax: Convex phase retrieval via basis pursuit. *IEEE Transactions on Information Theory*, 64(4):2675–2689, 2018.

[292] Oussama Dhifallah, Christos Thrampoulidis, and Yue M Lu. Phase retrieval via linear programming: Fundamental limits and algorithmic improvements. In *2017 55th Annual Allerton Conference on Communication, Control, and Computing (Allerton)*, pages 1071–1077. IEEE, 2017.

[293] Yuxin Chen and Emmanuel Candes. Solving random quadratic systems of equations is nearly as easy as solving linear systems. *Advances in Neural Information Processing Systems*, 28, 2015.

[294] Hong Hu and Yue M Lu. Universality laws for high-dimensional learning with random features. *arXiv preprint arXiv:2009.07669*, 2020.

[295] Rishabh Dudeja, Subhabrata Sen, and Yue M Lu. Spectral universality of regularized linear regression with nearly deterministic sensing matrices. *arXiv preprint arXiv:2208.02753*, 2022.

[296] Florent Krzakala, Marc Mézard, Francois Sausset, Yifan Sun, and Lenka Zdeborová. Probabilistic reconstruction in compressed sensing: algorithms, phase diagrams, and threshold achieving matrices. *Journal of Statistical Mechanics: Theory and Experiment*, 2012(08):P08009, 2012.

[297] Florent Krzakala, Marc Mézard, François Sausset, YF Sun, and Lenka Zdeborová. Statistical-physics-based reconstruction in compressed sensing. *Physical Review X*, 2(2):021005, 2012.

[298] Marco Mondelli and Andrea Montanari. Fundamental limits of weak recovery with applications to phase retrieval. In *Conference On Learning Theory*, pages 1445–1450. PMLR, 2018.

[299] Wangyu Luo, Wael Alghamdi, and Yue M Lu. Optimal spectral initialization for signal recovery with applications to phase retrieval. *IEEE Transactions on Signal Processing*, 67(9):2347–2356, 2019.

[300] Yue M Lu and Gen Li. Phase transitions of spectral initialization for high-dimensional non-convex estimation. *Information and Inference: A Journal of the IMA*, 9(3):507–541, 2020.

[301] Roman Vershynin. *High-dimensional probability: An introduction with applications in data science*, volume 47. Cambridge university press, 2018.

[302] László Erdős and Horng-Tzer Yau. *A dynamical approach to random matrix theory*, volume 28. American Mathematical Soc., 2017.

[303] Marc Mezard and Andrea Montanari. *Information, physics, and computation.* Oxford University Press, 2009.